3-D imaging based on hard x-ray grating interferometry: theory, development and application

Zur Erlangung des akademischen Grades eines
DOKTORS DER NATURWISSENSCHAFTEN
von der Fakultät Physik des
Karlsruher Instituts für Technologie (KIT)

genehmigte

Dissertation

von

M. Sc. Venera Weinhardt (geb. Altapova)
aus Tomsk

Tag der mündlichen Prüfung: 25.04.2014

Referent: Prof. Dr.rer.nat. T. Baumbach

Korreferent: Prof. Dr.rer.nat. V. Saile

Kurzfassung

Als im letzten Jahrzehnt neu aufgekommene Techniken erlauben es Phasenkontrast-Bildgebungs-Methoden im Röntgenbereich, schwach absorbierenden Stoffe zu untersuchen, die mit konventioneller Radiographie und Computer-Tomographie nicht abgebildet werden können. Eine dieser Techniken, die Talbot-Gitter-Interferometrie, nutzt verschiedene Kontrastmechanismen und kann selbst mit Röntgenquellen mit schwacher Kohärenz wie Laborquellen realisiert werden. Obwohl die Methode inzwischen in einer Reihe von Laboren implementiert wurde, existieren nach wie vor Einschränkungen bezü- glich Phasensensitivität, der Größe der untersuchbaren Proben sowie der Aufnahme- geschwindigkeit.

Ziel dieser Arbeit ist es, die Methode bezüglich dieser Einschränkungen an ihre Grenzen zu bringen. Dabei liegt der spezielle Fokus auf der Entwicklung und Optimierung der Gitterinterferometrie zur Phasenkontrastbildgebung *lateral ausgedehnter* Proben sowie der Erhöhung der Aufnahmegeschwindigkeit. Die Grundlagen für diese Entwicklungen werden mit der theoretischen Beschreibung des Vorwärtsproblems und des inversen Problems der Bildgebung gelegt, durch numerische Berechnungen unterstützt und in Beispielexperimenten demonstriert. Anschließend werden die wichtigsten Formeln für die Rekonstruktion der dreidimensionalen Verteilung von Absorption, Streuung und Phasenverschiebung in der Probe entwickelt. Anschießend wird die Charakterisierung von mikrostrukturierten Gittern und ein neues Gitterdesign, das auf einer Verkippung der Gitterlinien basiert, analytisch diskutiert und in Experimenten demonstriert, in denen eine Effizienzverbesserung gegenüber des konventionellen Designs beobachtet werden kann. Die Talbot Gitterinterferometrie wurde in die existierenden Aufbauten des TopoTomo Strahlrohrs bei ANKA sowie des ID19 Strahlrohrs an der ESRF integriert, wobei die jeweiligen komplementären Eigenschaften dieser beiden Strahlrohre ausgenutzt wurden. Basierend auf dem in dieser Arbeit entwickelten theoretischen Model wurde die Methode im Hinblick auf Phasensesitivität und Geschwindigkeit optimiert. Das Potential dieser neuen Aufbauten wird anhand einer Reihe von Anwendungen aus der Bildgebung veranschaulicht: der Untersuchung der Porosität polymerbasierter Gewebe-Gerüst, des Vergeleiches der Morphologie geund entfalteter Fledermausflügel sowie der Zerfall von Pergament.

Zusammenfassend erweiteren die methodischen Entwicklungen dieser Arbeit das Verständnis der Talbot Gitterinterferometrie, etablieren die Methode für Routineexperimente und erweiteren sie in Richtung einer Implementierung in der zerstörungsfreien Werkstoffprüfung sowie für medizinische Untersuchungen.

Abstract

Emerging in the last decade, x-ray phase contrast imaging techniques allow to visualize low absorbing tissues not accessible with conventional absorption radiography and computed tomography. Among them, the recently developed Talbot grating interferometry offers various contrast mechanisms and can be utilized even with low coherent table-top or laboratory x-ray sources. Even though the method has since been implemented and demonstrated at a number of facilities, it is still limited in terms of phase sensitivity, size of the accessible samples and acquisition speed.

This thesis aims on pushing limits of this method with respect to these shortcomings. Its particular focus was on the development and optimization of Talbot grating interferometry for phase contrast imaging of laterally extended samples and high speed. The foundation for this development is established by a theoretical description of the forward problem of image formation and the inverse problem of data retrieval, supported by numerical calculations and confirmed in exemplary experiments. The main reconstruction equations and an efficient 1-D projection filter are developed, yielding 3-D distribution of attenuation, scattering, and phase shift within the specimen. The characterization of grating microstructures and a novel design based on a tilted phase grating are discussed analytically and demonstrated experimentally, highlighting an increased efficiency with respect to the conventional one. Exploiting complementary characteristics of two different beamlines, Talbot grating interferometry was integrated to the existing tomographic and laminographic instruments of the TopoTomo beamline at ANKA and of the ID19 beamline at ESRF. Based on the theoretical model developed within this thesis, the method was optimized in terms of phase selectivity and speed of the experiments.

The potential of these new instruments is demonstrated by a wide variety of imaging applications: the investigation of porosity in polymer-based scaffolds, a morphological comparison of folded and unfolded bat wings, and the degradation of historical parchment. In conclusion, the methodical development presented in this thesis extends the understanding of Talbot grating interferometry, establishes the method for routine experiments, and advances it towards practical implementation in non-destructive testing and clinical diagnostics.

Acknowledgements

First of all, I am grateful to my professor, supervisor and after so many years a friend, Tilo Baumbach. His enthusiasm, support and faith in my work, kept me working, working and then working even harder. He was (and I guess is) crazy enough to give a chance to a girl from deep Siberian forest. I am thankful for this opportunity!

I would like to thank my reviewer, Prof. Saile for having interest and especially finding time to read and evaluate my work.

My gratefulness to Daniel Hänschke I am not capable of putting in words. Without him I would just never survive! From first moment on asking every stupid (no, truly stupid) question, I hope I could support you at least partially as much you did over this time. I think it is not necessary to write that every word, image and table in this thesis was part of his comments, reviews or just passing by and saying "looks great".

I would like to thank Julian Moosmann for his precious support during my first beamtimes. There is no better team and no more fun than me, Daniel and Julian gathering together to rock science.

Many thanks to Lukas Helfen. His warmth, optimism and smile kept my mood up at the hardest moments. It is always pleasure to work with him.

I thank Franz Kuchling, Barbara Trimborn, Dmitry Karpov, Feng Chen, Alina Spiridonova and Yulia Bykova for the opportunity which they gave me by being my students. I have learned more from them, than I will ever be able to give from my side. Being part of my life, friends and family, they kept me motivated asking questions but even more important for further, greater ideas which they could realize. Our life can bring us apart, but the moments which we spent together will always be in my heart. Thank you guys!

For supervising and helping me to start up as a scientist I would like to thank Danielle Pelliccia, Tim Weitkamp, Franz Pfeiffer and Christian David. High level of their scientific work will most probably remain for me unreachable.

I would like to thank Irene Zanette for her help and support during my first years. Working at two different countries and synchrotron facilities, we could always find a common language.

This work have been never possible without help of Institute for Microstructures and Technologies. I thank Elena Reznikova, Vladimir Nazmov, Jahonnes Kenntner and Markus Simon for never refusing to realize my next stupid idea or design upon x-ray gratings and lenses. I am happy to collaborate with Danays Kunka, Felix Marschall, Harald Vogt and Arndt Last. I hope our future work will bring us beyond available techniques. I thank Jürgen Mohr for helping me in this work.

I thank imaging group for the great scientific atmosphere, especially Patrik Vagovic, Angelica Ceccillia, Tomy dos Santos Rolo, Ralf Hoffman, Alexey Ershov, Thomas van de Kamp, Elias Hamann, Jochen Butzer, Ruth Heine and Yin Cheng. My special thanks to Thorsten Müller who always gave a great support during my experiments.

I would also like to thank Sondes Bauer for giving me an example of what hard work at large scale facility means. Best luck for your beamline and future experiments.

Despite of all work which I did for the past years I kept feeling myself as a drop in the ocean. Sometimes it is hard to realize, but behind this thesis hidden vast work and support from whole ANKA/IPS/LAS/KIT colleagues. With help of our administration, especially Danielle Rostohar, Katya Walter, Anne Stösser and Margit Helma, our technical department, Harald Schade, Marianne Knauer, Volker Weiss and Tobias Hilverling and our IT department, David Haas. I hope we will continue to do great science between addiction fun and pain!

I thank all collaborators and friends with whom I just started to work. I am looking forward to discover more together.

I thank Markus Riotte, Sergei Lazarev and Marthe Kaufholz for keeping fun around me and giving great advice on everyday survival. Many thanks to my friend Olga Bauder who made my work at KIT and my life in Germany brighter and full of pleasure.

I am very grateful to my husband Lothar Weinhardt for bringing meaning in my life (I really thought I already figured it out). Without him I might spent 10 more years to write this thesis.

Last but not the least, I express my gratitude to my parents, who does not understand why or what I do, but truly believes that whatever I am up to, I will perform the best.

: ——————— contents ———————

Contents

Conventions and symbols

This section summarizes common mathematical notations, symbols and abbreviations that will be used in this work:

(x, y, z) - real space coordinates, with z as a x-ray beam direction

$\perp$ - denotes vectors with coordinates in (x, z) plane, perpendicular to the sample plane

$\parallel$ - denotes vectors with coordinates in (x, y) plane, planes parallel to each over along the optical axis z

(f_x, f_y, f_z) - reciprocal space coordinates

$\mathcal{F}, \mathcal{F}^{-1}$ - Fourier transform and inverse Fourier transform

$\mathcal{G}$ - Fourier transform of function g

E - energy

λ - wavelength

c - speed of light

$K = \frac{2\pi}{\lambda}$ - wave vector

r_0 - Thomson scattering length (classical electron radius)

2-D, 3-D - two- and three-dimensional

CT - computed tomography

CTF - contrast transfer function

LIGA - Lithographie, Galvanik und Abformung

SEM - scanning electron microscopy

ROI - region of interest

CNR - contrast to noise ratio

ESRF - European Synchrotron Radiation Facility

ANKA - Angstromquelle Karlsruhe

BM - bending magnet

DMM - double multilayer monochromator

KNMF - Karlsruhe Nano and Micro Facility

UHMWPE - ultra high molecular weight polyethylene

PVDF - polyvinylidene difluoride

LDPE - low-density polyethylene

CONTENTS

CCD - charged-coupled device

MiQA - microscopy and quality assurance

1 Introduction

1.1 Motivation

Modern x-ray imaging methods are among the most important physical measuring tools of clinical diagnostics, non-destructive testing as well as imaging diagnostics in fundamental research. Its high penetration depth makes x-rays a unique and non-invasive tool for 3-D imaging of bulk objects with high spatial resolution. During the last two decades, a huge variety of new x-ray micro- and nano-imaging techniques has been successfully established at synchrotron sources, taking benefit from their outstanding beam properties. Coherent and high flux x-rays provided by synchrotron sources advanced the development of new and substantially enhanced contrast mechanisms. Main approaches include the usage of the x-ray's wave nature for phase contrast imaging (62, 67, 69, 90), the reconstruction of quantitative phase contrast, the electron density contrast via holographic x-ray propagation methods (90) or via (diffraction based) differential phase contrast imaging methods (25), and the use of small angle scattering causing dark-field contrast to collect nanostructure information (69).

One recently emerged phase contrast imaging method is the Talbot grating interferometry (23, 61). This method is based on two x-ray diffraction gratings for which self-imaging and the Moiré effect transform the phase shift introduced by the object into intensity modulations. Even though the usage of diffraction gratings requires coherent x-ray beam properties, the Talbot grating interferometry can be transferred to low coherent laboratory x-ray tubes with the help of an additional grating acting as multiple virtual sources (71). Thanks to the phase shift detected by the Talbot grating interferometer, soft tissues with similar absorption properties, for example organs of the human body, become destinguishable. Thus, the method will potentially replace current clinical diagnostic tools such as mammography, angiography, and computer tomography (13, 20).

Hard x-ray energies typical for clinical diagnostics require diffraction gratings with high aspect ratio (ratio of the width of a structure to it's height) to be used in the

Talbot grating interferometer. Deep x-ray lithography developed at the Karlsruhe Institute of Technology (KIT) allows to fabricate microstructures with aspect ratios of about 100, providing the highest aspect ratio microstructures available in the world (59). The ANKA light source is an application oriented synchrotron facility, operating more than 13 beamlines, among them three deep x-ray lithography beamlines for fabrication of diffraction gratings and other microstructures (7). The access to the unique properties of the synchortron source, diffraction gratings with high aspect ratio, and the interdisciplinary environment of KIT, it was offered the ideal environment to establish Talbot grating interferometry at ANKA and making it available for users from different application fields.

1.2 Existing phase contrast imaging techniques

In the hard x-ray range required to penetrate bulk materials, the phase shift introduced by the specimen dominates up to three orders of magnitude over absorption (8). Thus, the phase shift is the preferential contrast mode for x-ray imaging. However, detecting the phase shift directly is not possible due to the high frequency of oscillation of the electromagnetic field in the x-ray range and therefore the phase shift can only be detected if it is converted into x-ray beam intensity modulations.

There is a number of phase contrast imaging methods, which are characterized by the major mechanism used to transform the phase shift into intensity. They are classified as follows: 1) propagation (90); 2) analyser (12); and 3) interferometry (9, 23, 71). We will briefly describe the principles, advantages and limitations for each class of techniques. For a more complete overview, the reader is referred to the following reviews (39, 54, 58).

Propagation-based imaging methods employ self interference between the incident wave field and the scattered component of the transmitted wave field during free space propagation. More careful considerations shows that such interference patterns are sensitive to the Laplacian of phase modulations $\triangle\varphi(\boldsymbol{r}_{||})$. Thus, a homogeneous phase shift can not be detected by this technique. From the instrumental point of view, propagation techniques are the most simple class of methods as the x-ray detector only needs to be shifted further away from the specimen in comparison to conventional absorption radiography. However, strong requirements on the x-ray beam such as

high transverse and temporal coherence restricts these methods to be used only at third generation synchrotron facilities (19). The inverse problem of reconstructing the phase from intensity modulations has been solved by a number of algorithms (48, 52). However, the quantitative reconstruction of the object properties remains a challenge (14).

Analyser-based techniques integrate a Fourier filter (for example a crystal) into the setup, enhancing parts of the Fourier space (21). Therefore, they are sensitive to the gradient of the phase shift $\nabla\varphi(\boldsymbol{r}_{||})$. In this class of methods, it is possible to choose the phase shift desired for detection or acquire a series of images with different positions of the Fourier filter. As such a rocking scan allows to obtain the full range of deflection angles behind the sample, absorption, phase shift, and small-angle scattering signals are available within one measurement (25). The high angular selectivity of the Fourier filter comes at the cost of photon flux. Therefore, analyser-based imaging can be performed only at a high-flux beamline, where a reasonable exposure time can be achieved (90).

Interferometry is one of the oldest and most widely spread methods in visible light optics. It is based on the interference pattern created by the superposition of two or more waves. However, efficient optical components for interferometry in the x-ray range have been lacking until the end of the last century. Tremendous progress in technology (of optical devices) allowed to extend and implement visible light techniques for soft and hard x-rays. The first x-ray interferometer was proposed by U. Bonse and M. Hart (9). In their work, the authors utilized a set of optical elements: 1) a crystal which splits the beam into two by diffraction in Laue geometry ("beam splitter"); 2) a transmission mirror to introduce a phase shift in one (reference) beam; 3) an analyzer crystal that overlaps the reference beam with the beam passed through the specimen. In this setup, the phase shift introduced by the sample in one of the beams is transferred into fringe modulations. Such an interferometer is a very sensitive instrument for phase contrast imaging, since it allows a direct measure of phase differences. On the other hand, the beam requirements are very stringent. Highly coherent and monochromatic x-rays are required, thus restricting the applicability of such a system. Additionally, the instrument has to remain stable within nanoradian over the exposure time for an image (typically one minute) or a complete tomogram (a few hours).

Principles similar to analyzer-based and interferometry techniques were used to develop an interferometer based on two gratings the so-called Talbot grating interfer-

ometry (23, 61). The 1^{st} grating diffracts the incident wave field into two (or more) diffraction orders, acting as a beam splitter. These beams interfere along the propagation direction and are then transferred by the 2^{d} absorption grating, acting as an analyzer, into a detectable Moiré pattern. In comparison with the other phase contrast methods, Talbot grating interferometry can be implemented with low coherent x-ray radiation, working even with laboratory sources (71). At the same time, the angular sensitivity of the method is in the same range (nanoradians) as that of a crystal interferometer, which in combination with laboratory sources offers the potential for implementation in medical physics, life science, and clinical studies in the near future.

1.3 Aims and outline of the thesis

For the last decade, the originally two-dimensional Talbot grating interferometry was extended to three-dimensional computed phase contrast tomography, gaining quantitative volumetric information of the refractive index distribution (66, 70). A new contrast mode based on scattering ("dark-field") available in grating interferometry has been discovered a few years ago (69). Thus, grating interferometry offers three contrast functions: absorption, phase shift, and dark-field can be retrieved from the analysis of the same intensity pattern. The method has since been implemented and demonstrated at a number of synchrotron radiation facilities and at laboratories using an x-ray tube for visualization of features not accessible by conventional absorption tomography (31, 60, 81).

Meanwhile, conventional tomographic imaging of laterally extended (rather flat) objects requires to choose between local tomography with a limited field of view, due to the large sample area, or limited angle tomography, due to insufficient x-ray penetration. Both result in incomplete or inconsistent sampling in frequency space causing artifacts in the reconstructed volume. Additionally, even though the method has become commonly used, the acquisition speed and performance in terms of phase sensitivity is not efficient making systematic studies impossible.

Within this thesis, these drawbacks of Talbot grating interferometry were tackled with the following aims:

– Compact theoretical description and modeling for computer simulations of grating interferometry with the focus on either increasing acquisition speed or sensitivity

to the phase shift.

- Description and development of reconstruction equations for combination of grating interferometry with laminographic geometry in all three contrast modes to image laterally extended objects.

- Provide means for characterization, selection, and development of gratings in terms of image quality.

- Based on the theoretical considerations, develop and implement high-speed and high-sensitivity grating interferometer setups. Demonstrate the performance of the instrument in terms of spatial resolution, phase sensitivity, available contrasts, and apply on relevant application cases.

The thesis is structured as follows. After this introduction, the principles of grating-based interferometry are discussed in Chapter 2. The chapter describes the interaction of x-rays with matter, background information on absorption and phase contrast. The diffraction on gratings, propagation of the wavefront behind the grating as well as the Talbot and the Moiré effect are profoundly described. The inverse problem of reconstruction absorption, phase, and dark-field contrasts in 3-D tomographic and laminographic geometry is derived.

Chapter 3 is dedicated to x-ray gratings. State of the art fabrication of diffraction gratings is described. A further focus is on the characterization and quality assurance of phase and absorption gratings. The novel design of phase grating that uses tilted structures is experimentally verified.

The development and implementation of high-speed phase contrast imaging is described in Chapter 4. The instrumental setup and the mechanical requirements of grating interferometry are described. It is outlined how by optimisation of the x-ray energy bandwidth and development of a new acquisition scheme high-speed grating interferometry is possible. The spatial resolution, phase contrast sensitivity, and speed achievable with the developed instrument is demonstrated by proof-of-principal experiments. The application of grating interferometry to study porosity in polymer-derived scaffolds is outlined.

Chapter 5 is dedicated to high sensitivity phase contrast imaging. The implementation of the compact grating interferometer into the existing laminography setup at the

ID19 beamline is outlined. The optimization of the x-ray coherence properties is briefly described. Proof-of-principle experiments demonstrate the achievable phase sensitivity, ability to tune phase selectivity and dark-field contrast, and the correlation of multiple contrasts in relation to different morphologies of the same specimen. High-sensitivity phase contrast imaging is applied to study degradation in historical Dead Sea scrolls.

Chapter 6 summarizes the work performed within this thesis and outlines future perspectives and developments in grating interferometry.

2 Principles of grating-based interferometry

Contents

This chapter gives a compact theoretical description of grating based three-dimensional imaging. The theory is based on the projection approximation for scattering by the sample and Fresnel diffraction by the grating. Diffraction by the grating and it's self-imaging or Talbot effect is developed for different types of gratings. The disturbance of the grating diffraction pattern by the sample is transformed by the second grating to a Moiré pattern. The Moiré pattern is further used to reconstruct object contrast functions. The reconstruction of the 3-D object contrast functions is described for the laminographic geometry, a special case of which is conventional computer tomography (CT). The last section shows the theoretical description of the effect of partial coherence on imaging with grating interferometry.

2.1 X-ray imaging

X-rays are electromagnetic waves with a short wavelength λ (high frequency, ω). The interaction of electromagnetic waves with a medium is gathered by classical electromagnetic theory in terms of Maxwell's equations (43). Assuming a nonmagnetic medium, it is convenient to describe the interaction of x-rays with matter by the index of refraction n:

$$n(\omega) = 1 - \delta(\omega) + i\beta(\omega). \tag{2.1}$$

wherein $\delta(\omega)$ is the refractive index decrement, and $\beta(\omega)$ is the imaginary part of the refractive index.

The imaginary part of the refractive index $\beta(\omega)$ is related to the absorption of the incoming photons by electrons in medium (86). If the photoabsorption factor by one electron is described by $f^{''}(\omega)$, the imaginary part of the refractive index is described by:

$$\beta(\omega) = -\left(\frac{2\pi\rho_e r_0}{K^2}\right)\sum_{m=1}^{M} f_m^{''}(\omega). \tag{2.2}$$

Here, ρ_e denotes the electron density of the material, r_0 is the Thomson scattering length, K is the length of the incident wavevector $\boldsymbol{K}_0$ related to the frequency of the incoming x-ray radiation ω by $|\boldsymbol{K}_0| = K = \frac{\omega}{c} = \frac{2\pi}{\lambda}$, and M is the number of electrons in the medium. The photoabsorption effect exhibits strong discontinuities at energies close to bound electron's energy levels (absorption edges or anomalous contributions), see Fig.2.1 (a).

The refractive index decrement is related to the elastic scattering processes within the medium and described by the wave vector transfer or scattering vector $\boldsymbol{Q}$. If the energy of the incident x-ray radiation is far from the absorption edges, the scattering process can be described as scattering on free electrons within the material. In the case of x-ray imaging experiments, as an approximation only forward scattering $\boldsymbol{Q}/\boldsymbol{K} \ll 1$ is considered that $f(\boldsymbol{Q}) \sim f(0)$. With this the refractive index decrement δ can be written as (18):

$$\delta(\omega) = \frac{2\pi\rho_e r_0 \sum_{m=1}^{M} f_m^0(\omega) + f_m^{'}(\omega)}{K^2}. \tag{2.3}$$

The Thomson scattering length $f^0(\boldsymbol{Q})$, the photoabsorption factor $f^{''}(\omega)$ and the anomalous contributions $f^{'}(\omega)$ for gold as a function of photon energy is shown in

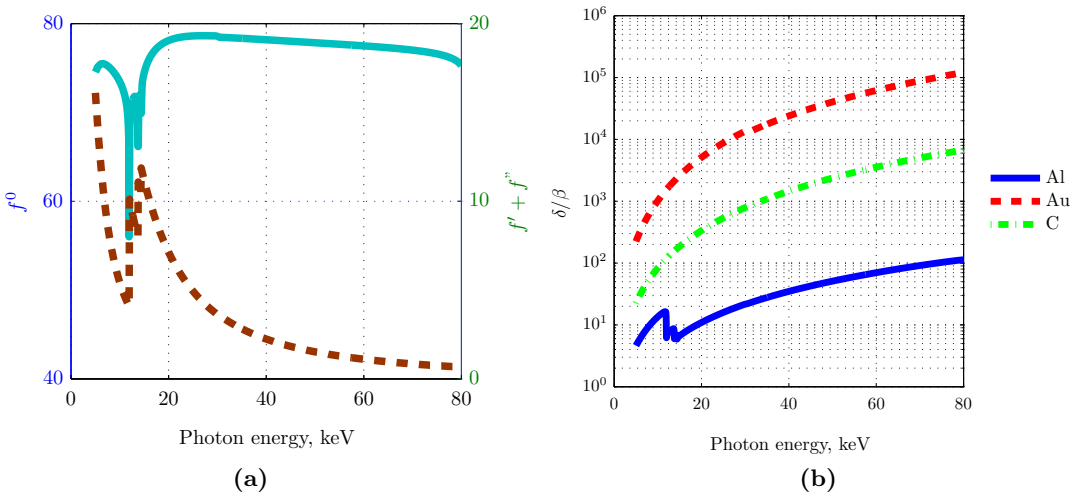

Figure 2.1: (a) The atomic scattering factor f^0, the anomalous contributions and the photoabsorption factor, $f' + f''$ for gold as a function of photon energy. (b) Ratio of real and imaginary part of the refractive index for aluminum, gold, and carbon. The data is calculated using the xop software (8, 24).

Fig.2.1 (a). For this particular case, we can observe anomalous behavior of the scattering factor for energies of about 14, 13 and 12 keV, corresponding to the $L_{1,2,3}$ binding energy levels (82). The δ to β ratio for some typical materials is shown in Fig. 2.1 (b). For the x-ray energy range of 20-100 keV, δ and β are small numbers in the order of 10^{-5} to 10^{-7}, thus the refractive index of x-rays is only slightly smaller than 1. For light elements like carbon δ can be up to 10^5 times larger than β. As scattering dominates over photoabsorption for light elements, in the hard x-ray energy range the phase contrast is significantly higher than absorption.

Throughout this work, the complex refractive index, its decrement and real part are used to describe the principles of grating interferometry. Taking into consideration how weak the photon - matter interactions are $(1 - n)$ will be used instead of n.

There are other x-ray interaction mechanisms, such as Compton scattering and pair production. Also photoelectron emission and different relaxation processes following photoabsorption, such as Auger electron and fluorescent x-ray emission are extensively used for chemical analysis and as means of studying for example the electron binding energies in solids (74). But they are not discussed within this work.

2.1.1 Absorption contrast

Let us assume an incident plane wave $\exp(i\boldsymbol{K}_0\boldsymbol{r})$ with a wave vector $\boldsymbol{K}_0$ along the optical axis z. We assume that the scattering of a sample is as weak or it's thickness is as small, that within a resolution of the detector there is no propagation effect on the wave field in the sample. It is called *projection approximation*, such that the field $E_T(\boldsymbol{r})$ just downstream of the object $z = 0$ is give by:

$$E_T(\boldsymbol{r}) = T(\boldsymbol{r}_\parallel)E_0(\boldsymbol{r}_\parallel)\exp(i\boldsymbol{K}_0\boldsymbol{r}). \tag{2.4}$$

with $\boldsymbol{r}_\parallel$ being a vector in x, y plane. The phase and amplitude changes within the object of the thickness L are approximated by line integrals of the refractive index distribution (x-ray transform), $p = \int_L\{\boldsymbol{K}(1 - n(\boldsymbol{r}))\}\mathrm{d}l$ and defined by the so-called transmission function of the object:

$$T(\boldsymbol{r}_\parallel) = \exp(-ip(\boldsymbol{r}_\parallel)) = A(\boldsymbol{r}_\parallel)\exp(i\phi(\boldsymbol{r}_\parallel)), \tag{2.5}$$

with the change in amplitude

$$A(\boldsymbol{r}_\parallel) = \exp\left(-\frac{2\pi}{\lambda}\int_L \beta(\boldsymbol{r})\mathrm{d}l\right), \tag{2.6}$$

and relative change in phase, so-called phase shift

$$\phi(\boldsymbol{r}_\parallel) = -\frac{2\pi}{\lambda}\int_L \delta(\boldsymbol{r})\mathrm{d}l. \tag{2.7}$$

The use of two-dimensional functions $A(\boldsymbol{r}_\parallel)$ and $\phi(\boldsymbol{r}_\parallel)$ is only applicable under the assumption that the Fresnel diffraction on the wave field within the object is negligible. This condition holds if the radius of the first Fresnel zone corresponding to propagation in the object is small compared to the spatial resolution SR: $\sqrt{\lambda L} < SR$ (49). According to Eq. 2.7 projection approximation sets an upper limit to the maximum tolerable phase shift. For example, for a resolution of 1 μm and an x-ray wavelength of 0.1 nm, the maximum thickness of a soft tissue is limited to 1 cm by the diffraction effect. Thus, the maximum phase shift is limited to $100{\cdot}\pi$ (19). It is clear that for thicker samples like a human body the projection approximation is not valid any longer. In such case, transmission of x-rays through the sample can be approximated by transmission through a set of N slices with the sample thickness ΔL, the so called

multi-slice approach (35). For the most theoretical and experimental results in this work, the projection approximation is valid.

In conventional (absorption-based) x-ray imaging experiments, such as radiography, we record the intensity of the wave front just behind the sample:

$$I_T(\boldsymbol{r}_\parallel) = |E_T(\boldsymbol{r}_\parallel)|^2 = I_0(\boldsymbol{r}_\parallel) \exp\left(-\frac{4\pi}{\lambda}\int_L \beta(\boldsymbol{r})\mathrm{d}l\right) = I_0(\boldsymbol{r}_\parallel) \exp\{\int_L -\mu(\boldsymbol{r})\mathrm{d}l\} \quad (2.8)$$

with the absorption coefficient $\mu(\boldsymbol{r}) = \frac{4\pi}{\lambda}\beta(\boldsymbol{r})$ describing the intensity loss due to photoabsorption. Eq.2.8 is the well-known *Lambert-Beer law*. Far from absorption edges, the recorded x-ray projection $I_T(\boldsymbol{r}_\parallel)$ is proportional to Z^4E^{-3}, thus allowing to differentiate between different elements (89). The amplitude of the transmission function and consequently the projection of the absorption coefficient can be obtained if $I_0(\boldsymbol{r}_\parallel)$ and $I_T(\boldsymbol{r}_\parallel)$ are measured (see Eq.2.8). Such type of x-ray imaging experiment is called absorption imaging. In absorption imaging, the information on scattering within the sample (phase) is lost.

2.1.2 Phase contrast

Phase modulations can only be detected by being turned into amplitude modulations whether through optical elements or after propagation. The propagation of x-rays in free space can be described by Huygens-Fresnel principle, stating that every point of the wave field may be considered as a source of interfering secondary wavelets (10). When the wavefront propagates from (x, y) plane into the (X, Y) plane (see Fig. 2.2), the propagated wavefront is the integration over all secondary wavelets of amplitude $E_0(\boldsymbol{r})$, according to *Kirchhoff diffraction integral*:

$$E(X,Y) = \frac{1}{i\lambda}\iint E_0(\boldsymbol{r}_\parallel)\frac{e^{iKR}}{R}\cos\theta \mathrm{d}x\mathrm{d}y. \quad (2.9)$$

In paraxial approximation with assumption that the wave field propagates along z with a small angle of deviation θ, we can say that $\cos\theta = 1$. In Eq. 2.9

$$R = \sqrt{(X-x)^2 + (Y-y)^2 + z^2}$$

and in the case of the short propagation distances can be further approximated in the denominator of Eq. 2.9 as $R \approx z$ and in e^{iKR}:

$$R = \sqrt{(X-x)^2 + (Y-y)^2 + z^2} \approx z + \frac{(X-x)^2 + (Y-y)^2}{2z}. \quad (2.10)$$

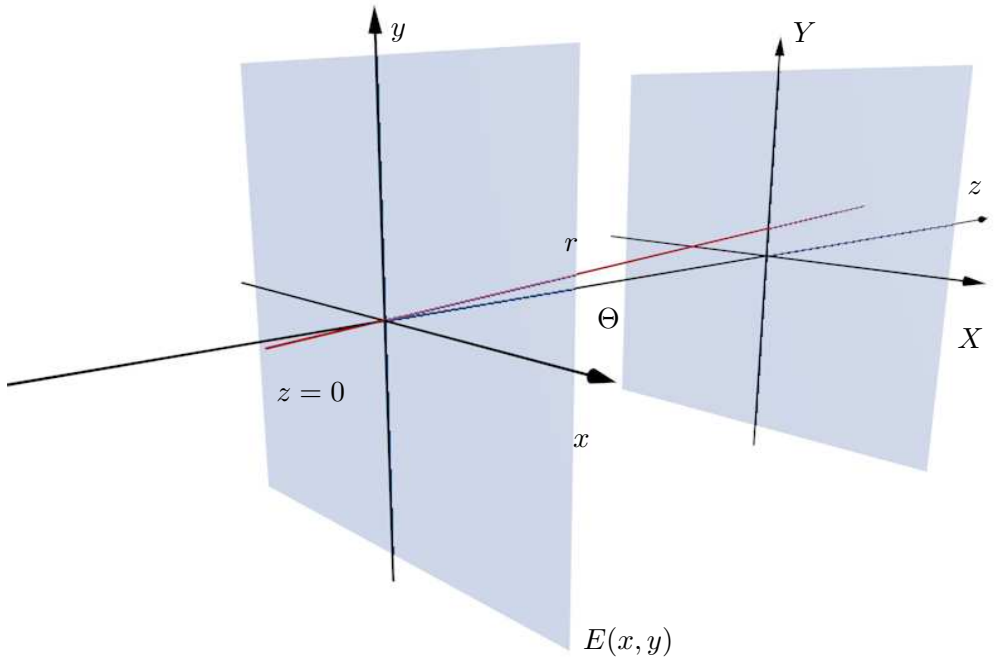

Figure 2.2: Axis schematics for free space propagation of x-rays. The wavefront $E(x, y)$ propagates along an optical path from $z = 0$ towards the observation plane (X, Y). The x-ray path $\boldsymbol{R}$ deviates by the angle θ from the optical path z.

Substituting it into Eq. 2.9 results:

$$E(X,Y) = \frac{1}{i\lambda}\frac{e^{iKz}}{z}\iint E_0(\boldsymbol{r}_\parallel)\exp\left[iK\frac{(X-x)^2+(Y-y)^2}{2z}\right]\mathrm{d}x\mathrm{d}y. \tag{2.11}$$

The propagation of the x-ray wave front in real space can be described via convolution of the wavefront with the propagator as:

$$E(X,Y) = E_0(\boldsymbol{r}_\parallel) * P_z(X,Y), \tag{2.12}$$

where $P_z(X,Y)$ is a propagator:

$$P_z(X,Y) = \frac{e^{iKz}}{i\lambda z}\exp\left[iK\frac{(X-x)^2+(Y-y)^2}{2z}\right]. \tag{2.13}$$

The convolution in real space can be carried out as a multiplication in Fourier space

$$E(X,Y) = \mathcal{F}^{-1}\left[\mathcal{F}(E_0(\boldsymbol{r}_\parallel))\mathcal{F}(P_z(X,Y))\right], \tag{2.14}$$

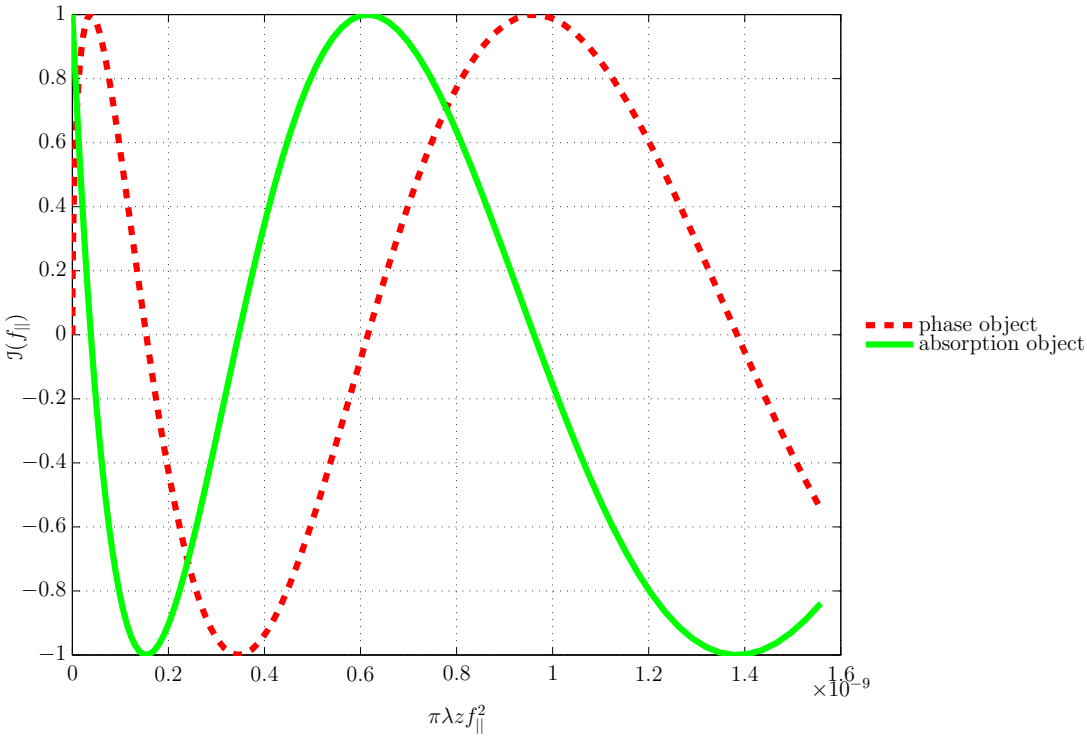

Figure 2.3: Contrast transfer function (Eq. 2.16) for pure phase and absorption objects.

with the propagator in reciprocal space being:

$$\mathcal{F}(P_z(X,Y)) = \mathcal{P}_z(f_X, f_Y) = \exp(iKz)\exp\left[-iz\frac{f_X^2 + f_Y^2}{2K}\right] \tag{2.15}$$

with spatial frequencies f_X and f_Y corresponding to respectively X and Y. Eq.2.14 allows to calculate the wavefront at any plane (X, Y) behind different optical elements or objects. Based on these main equations a simulation code was written in Matlab and used throughout this work for illustrating phenomena related to grating interferometry.

Taking into account weak absorption and phase variations (*linear approximation*) in Eq. 2.5 and substituting it into Eq. 2.14 yields the propagation of the wavefront after the sample (38):

$$\mathcal{I}(\boldsymbol{f}_\parallel) = 2\mathcal{O}(\boldsymbol{f}_\parallel)\sin(\pi\lambda z\boldsymbol{f}_\parallel^2) - 2\mathcal{M}(\boldsymbol{f}_\parallel)\cos(\pi\lambda z\boldsymbol{f}_\parallel^2). \tag{2.16}$$

Eq.2.16 is called *contrast transfer function* (CTF) in analogy to electron microscopy (84). The CTF describes absorption and phase variations within the sample depending

on spatial frequencies as cosine and sine functions of propagation distance z correspondingly (Fig. 2.3). The linear approximation holds under the condition that the phase shift is small $\mid \phi \mid \ll \pi$ and that it changes only slowly with the position in the object plane $\mid \phi(\boldsymbol{r}_\parallel - \lambda z \boldsymbol{f}_\parallel) - \phi(\boldsymbol{r}_\parallel) \mid \ll 1$ (21).

Considering the Kirchhoff diffraction integral Eq. 2.9 and the CTF in Eq.2.16, we can introduce the Fresnel number (37):

$$N_f = \frac{a^2}{z\lambda}, \tag{2.17}$$

with the wave with a wavelength λ, the aperture with the radius a and propagating to the distance z. The Fresnel number is a measure for diffraction during propagation of the x-rays. Let us distinguish three different diffraction regimes such as near-field ($z \ll \frac{a^2}{\lambda}$), Fresnel ($z \approx \frac{a^2}{\lambda}$), and Fraunhofer ($z \gg \frac{a^2}{\lambda}$). Based on the theory described above, a series of radiographic images for different propagation distances were simulated (Fig. 2.4). The phantom object consists of a set of spheres made of different materials: Au (200 μm radius), Al (300 μm radius), ethanol (200 μm radius) and polyethylene (100 μm radius). For the x-ray energy of 25 keV used in the simulations, the gold sphere is a good example of a pure "absorption object", while other materials can be considered as pure "phase objects". Fig. 2.4 (b) shows the image at $z = 0$ (radiography), where only the gold and aluminum spheres are visible according to Eq. 2.8. In the near-field regime, other spheres become slightly visible due to the propagation effect (Fig. 2.4 (c)). The effect of the propagation is even more visible in the Fresnel regime (Fig. 2.4 (d)). Further increasing the propagation distance towards the Fraunhofer regime does not provide any further additional information and poses a challenge for reconstructions of the original phase of the objects. In this example we can see that for propagation through a sphere acting as a phase object, the 1^{st} diffraction fringe appears black (destructive interference, see Fig. 2.4 (e)), while for the absorption sphere the 1^{st} diffraction fringe appears white (constructive interference, Fig. 2.4 (d)). Note that due to the limited raster (resolution) of the printer, Fig. 2.4 might show a Moiré pattern.

At hard x-ray energies, we may assume the objects to induce a pure phase shift variation such that in Eq. 2.16 $\mathcal{M} = 0$. If such an object is located in the near-field regime, $z \ll \frac{a^2}{\lambda}$, we can discard higher terms of $\sin(\pi\lambda z \boldsymbol{f}_\parallel^2)$ and expand Eq. 2.16, the intensity at the detector plane is (57, 72, 90):

$$I(X, Y) \approx \frac{\lambda z}{2\pi} \phi''(\boldsymbol{r}_\parallel). \tag{2.18}$$

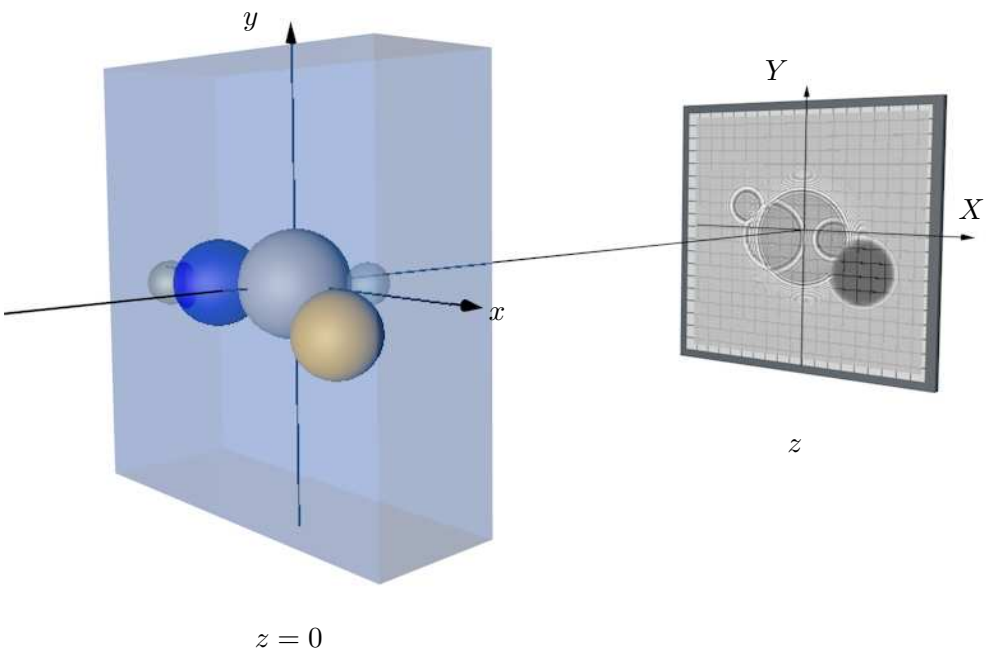

(a)

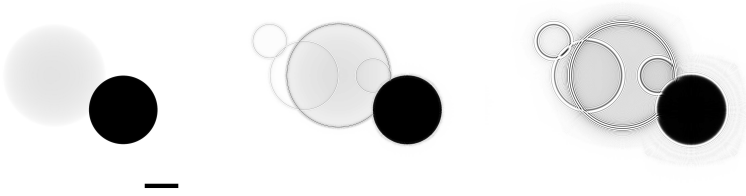

(b) **(c)** **(d)**

Figure 2.4: (a) Schematics of the experimental setup. The x-ray wavefront is propagated through spheres made out of Au (200 μm radius), Al (300 μm radius), ethanol (200 μm radius), and polyethylene (100 μm radius) and detected at the distance z by a 2-D detector. (b) Simulated x-ray projection at $z = 0$. (c) near-field regime, at $z = 0.1\,\mu m$. (d) Fresnel regime at $z = 1\,\mu m$. The scale bar is 100 μm. Color range on all images is from black (0% transmission) to 1 (100%). The results were generated with SRCLsim tool developed by Petr Mikulik (40).

In first approximation, the intensity distribution behind the sample depends on the Laplacian operator applied to phase $\phi(\boldsymbol{r}_\parallel)$ and on the propagation distance. Without reconstructions,in-line phase contrast imaging techniques within the sample consisting of a single material will be sensitive to it's edges, cracks or bubbles. However, the challenge is to retrieve *quantitatively* information about the object's refractive index. As the object transmission function consists of two unknowns, i.e. real and imaginary part (Eq. 2.5), minimum of two images are required.

Two other classes of phase-contrast imaging techniques, such as analyzer- and interferometry-based techniques are based on the usage of optical elements (crystals) as Fourier space filters in order to turn phase variations within the sample into an amplitude modulations. In the following, we will discuss the technique chosen for this thesis, namely Talbot grating interferometry.

2.2 Diffraction on gratings

The Talbot grating interferometers described and developed within this work are based on two diffraction gratings, one phase grating and one analyzer (absorption) grating. Therefore, understanding of x-ray diffraction and propagation after the gratings was an essential part of this thesis and the necessary formulas were derived and described in the following paragraphs. There are different types of diffraction gratings differing in shapes, material and application. Based on practical considerations the focus was on one shape of gratings (square-shape type).

Gratings

A grating is a periodic object, which in the Fourier space will have discrete peaks. From the diffraction point of view, the experiment is more illustrative to be described in reciprocal space via the Ewald sphere representation (Fig.2.5). The radius of the Ewald sphere in case of elastic scattering is determined by the wave vector of the incident beam K (74). The reciprocal lattice for a one-dimensional diffraction grating with a period p is a set of rods with the reciprocal grating vectors $|\boldsymbol{h}_m| = m2\pi/p$. The intersection of these planes with the Ewald sphere represent waves diffracted by the grating.

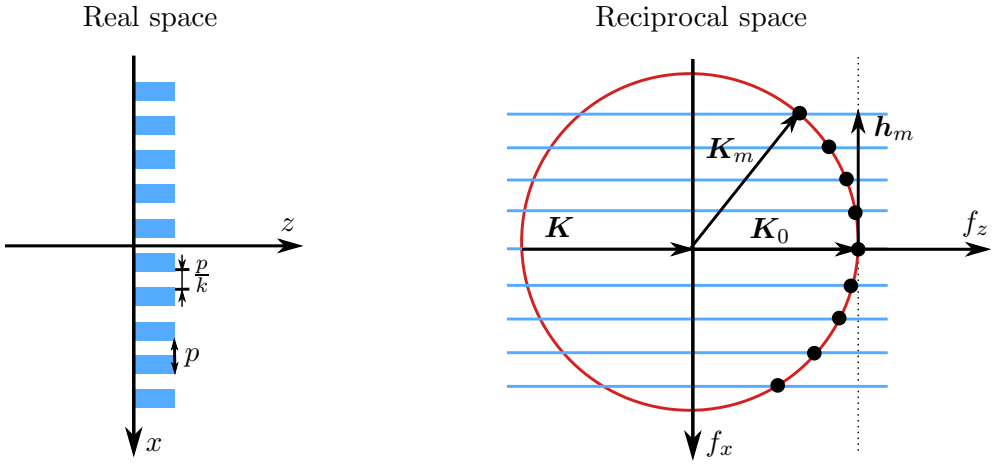

Figure 2.5: Real space representation (left) and the Ewald sphere construction (right) for the diffraction grating. The wavevector of the preliminary wave $\boldsymbol{K}, \boldsymbol{K}_0$ pointing to the origin of the reciprocal space, and diffracted by grating wave vectors $\boldsymbol{K}_m$ with reciprocal grating vectors $\boldsymbol{h}_m$.

Let us consider a square profile grating with a period of p and groove widths p/k with corresponding thicknesses t_1 and t_2 described by it's transmission function f as:

$$f(x) = \begin{cases} T_1, 0 < x < \frac{p}{k} \\ T_2, \frac{p}{k} < x < p \end{cases} \tag{2.19}$$

Here, T_1 and T_2 denote the transmission function according to Eq. 2.5 for thicknesses t_1 and t_2, respectively and k is the ratio of groove period to space period, where $1/k$ is also known as the grating duty cycle.

For reciprocal space representation, the grating transmission function (Eq. 2.19) is decomposed into a Fourier series S_N

$$(S_N f)(x) = T_2 + \frac{(T_1 - T_2)}{k} + \sum_{n=1}^{\infty} \left(\frac{T_1 + T_2}{\pi n} \right) \sin \frac{2\pi n}{k} \cos \frac{2\pi n x}{p} + \\ + \sum_{n=1}^{\infty} \left(\frac{T_1 + T_2}{\pi n} \cos 2\pi n - (T_1 + T_2) \cos \frac{2\pi n}{k} \right) \sin \frac{2\pi n x}{p}.$$

In the following, $k = 2$ (a duty cycle of 0.5) is assumed. Such grating is known as Ronchi type and widely used in interferometry. In this case, the Fourier series of grating transmission function becomes:

$$(S_N f)(x) = \frac{T_1 + T_2}{2} + \frac{2(T_1 - T_2)}{\pi} \sum_{m=1}^{\infty} \frac{\sin \frac{2\pi(2m-1)x}{p}}{2m - 1} \tag{2.20}$$

with $2m-1$, meaning that non-zero even diffraction orders after such gratings are forbidden.

In reciprocal space, the diffracted wavefield $E_G(x)$ behind the grating is the multiplication of the Fourier series of the transmission function with the propagator defined in Eq. 2.15. In the case of a 1-D grating $f_Y = 0$ and since even diffraction orders are forbidden, the reciprocal grating vector is $|\boldsymbol{h}_m| = 2\pi(2m-1)/p$ and we get:

$$E_G(x) = \frac{T_1+T_2}{2} + \frac{(T_1-T_2)}{\pi i}\sum_{m=1}^{\infty}\frac{\exp(ih_m x)}{2m-1}\exp\left[-iz\frac{h_m^2}{2K}\right] - \\ -\frac{(T_1-T_2)}{\pi i}\sum_{m=1}^{\infty}\frac{\exp(-ih_m x)}{2m-1}\exp\left[-iz\frac{h_m^2}{2K}\right]. \tag{2.21}$$

The first term in Eq. 2.21 corresponds to the 0^{th} diffraction order, whereas the second and third term accounts for positive and negative diffraction orders. The propagation term $\frac{e^{iKz}}{i\lambda z}$ is omitted as it is the same for all propagating wavefronts.

In order to optimize the method, it is necessary to identify parameters which can be influenced experimentally. In the case of grating diffraction, it is first of all the diffraction efficiency η_m of the grating, determined as $\eta_m = |c_m|^2$, where c_m are the Fourier coefficients of the corresponding diffraction orders (83). From the Eq. 2.20, the efficiency of a Ronchi type grating can be written as:

$$\eta_m = \left|\frac{T_1-T_2}{\pi i(2m-1)}\right|^2 \tag{2.22}$$

We can see that the highest efficiency of the grating can be achieved only by maximazing the difference between the two transmission values $|T_1 - T_2|$. As transmission functions are complex numbers, the first condition for maximum efficiency is that their amplitudes equal to unity $A_1 = A_2 = 1$. Such a grating will represent a pure phase object with $\beta_1 = \beta_2 = 0$. The second condition is a phase difference of these transmission functions of π (68). The diffraction efficiency for grating using pure absorption and pure phase with π and $\pi/2$ phase difference (further named as phase shift) are calculated according to the Eq. 2.5 and Eq.2.22 and are shown in Fig. 2.6. For the pure absorption grating, the maximum efficiency is always limited to 50% (or to its transmission value) see first term in the Eq. 2.22, therefore diffraction gratings are fabricated out of light materials with the negligible absorption at the energies to be used. For a π-shift grating, there is no 0^{th} diffraction order and most of the diffracted

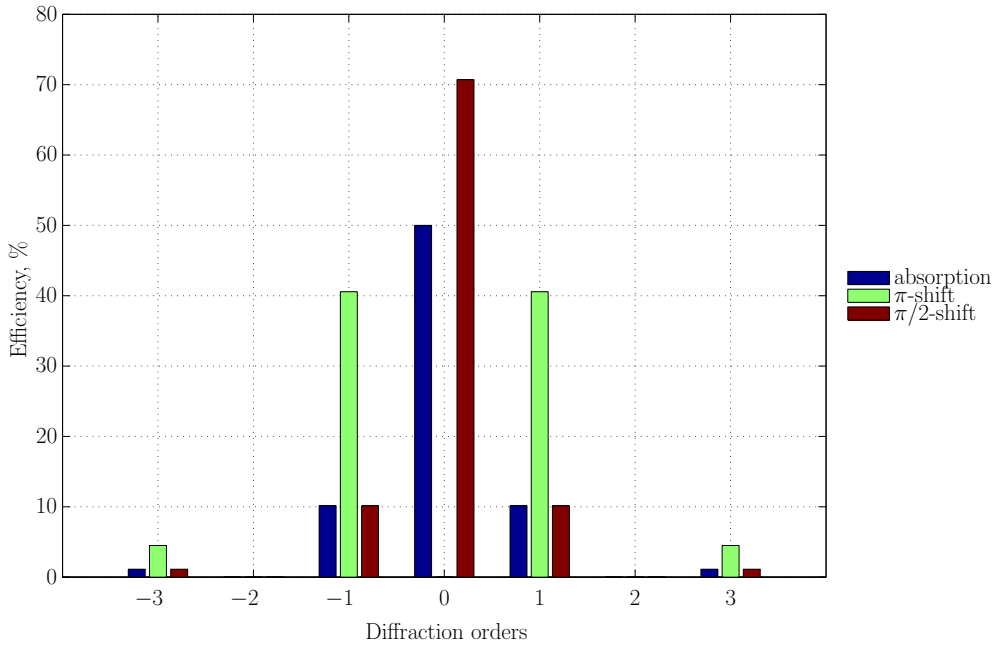

Figure 2.6: Diffraction efficiency of gratings using absorption and pure phase ($A_1 = A_2 = 1$) with π and $\pi/2$ phase difference for the diffraction orders $m = -3, .., +3$.

wave field will be distributed to the $\pm 1^{st}$ diffraction orders. For a $\pi/2$-shift grating, the 0^{th} diffraction order is the most dominant with 20% of diffraction distributed between the $\pm 1^{st}$ diffraction orders (68).

2.3 The Talbot effect

Let us further consider the propagation of the diffracted orders behind the grating. The propagation angles of the diffraction orders depend on $f_{\parallel}$ and f_z (see Fig. 2.5). Assuming that $K \gg h_m$ which is true for hard x-rays and gratings with the period in the micrometer range, we can write:

$$\tan\theta_m = \frac{f_{\parallel}}{f_z} = \frac{h_m}{\sqrt{K^2 - h_m^2}} \approx \frac{h_m}{K} \tag{2.23}$$

The angles of diffraction are in the range of microradians, thus the paraxial approximation remains valid for propagation of the leading diffraction orders.

From Eq. 2.21, we can conclude that the propagation phenomena are periodic along z and will be repeated every time as $z\frac{h_m^2}{2K} = n\pi$, with $n = 1, 2, 3, ...$ This effect is known

as self-imaging or Talbot effect, first observed in 1836 (80). We will define the Talbot distances corresponding to the self-imaging phenomena as $z_T = \frac{2np^2}{\lambda}$.

It is convenient to consider the self-imaging effect in the complex plane (56) (see Fig. 2.7(a)). For different types of gratings, the complex transmission functions T_1 and T_2 are positioned in the complex plane. The efficiency of diffraction orders is determined by the difference of these transmission functions (see Eq. 2.21). The propagation effect corresponds to the rotation of the difference of two transmission functions. Let us as before in consider three types of gratings in details:

1. absorption grating, where the absorption of x-ray radiation for lamellas is 100 % and for grooves 0 % the transmission functions in complex plane are ■ ($T_1 = 1$) and ▲ ($T_2 = 0$) correspondingly, see Fig. 2.7(a). The mean value of the transmission functions (zero diffraction order) is depicted as ◯. One full circle corresponds to the propagation over the Talbot distance z_T. The propagation of the diffracted wavefield would correspond to the translation of the mean value ◯ by $n\pi/2$. We can see that the mean and the difference of two transmission functions will be reproduced at the Talbot distance z_T. At the fractional distance $z = z_T/2$ the self-imaging effect takes place as well, however the role of bright and dark regions of the interference pattern is inverted (as ■ becomes positioned at 0 and ▲ at 1). The simulated diffraction of the absorption grating and the corresponding intensity pattern behind the grating over the Talbot distance is depicted in Fig. 2.7(b). The intensity variation at the fractional Talbot distances has the same periodicity p as the period of the diffraction grating. At the distance $z = z_T/2$, the intensity pattern is inverted as expected from the complex plane representation.

2. The phase grating with $\pi/2$ phase shift is represented by two transmission functions with the phase of $+\pi/4$ and $-\pi/4$ in the complex plane (Fig. 2.7(c)). The self-imaging takes place as well at the fractional distance $z = z_T/2$, however there are no intensity variations (pure phase grating introduce only phase modulations which are repeated at $z = z_T/2$). The self-imaging effect for $\pi/2$ phase grating is the same as for pure absorption grating but shifted by $z_T/4$ or $\pi/2$ in the complex plane (as cos and sin in the contrast transfer see Fig. 2.3). The simulated intensity pattern evidences this effect (see Fig. 2.7(d)).

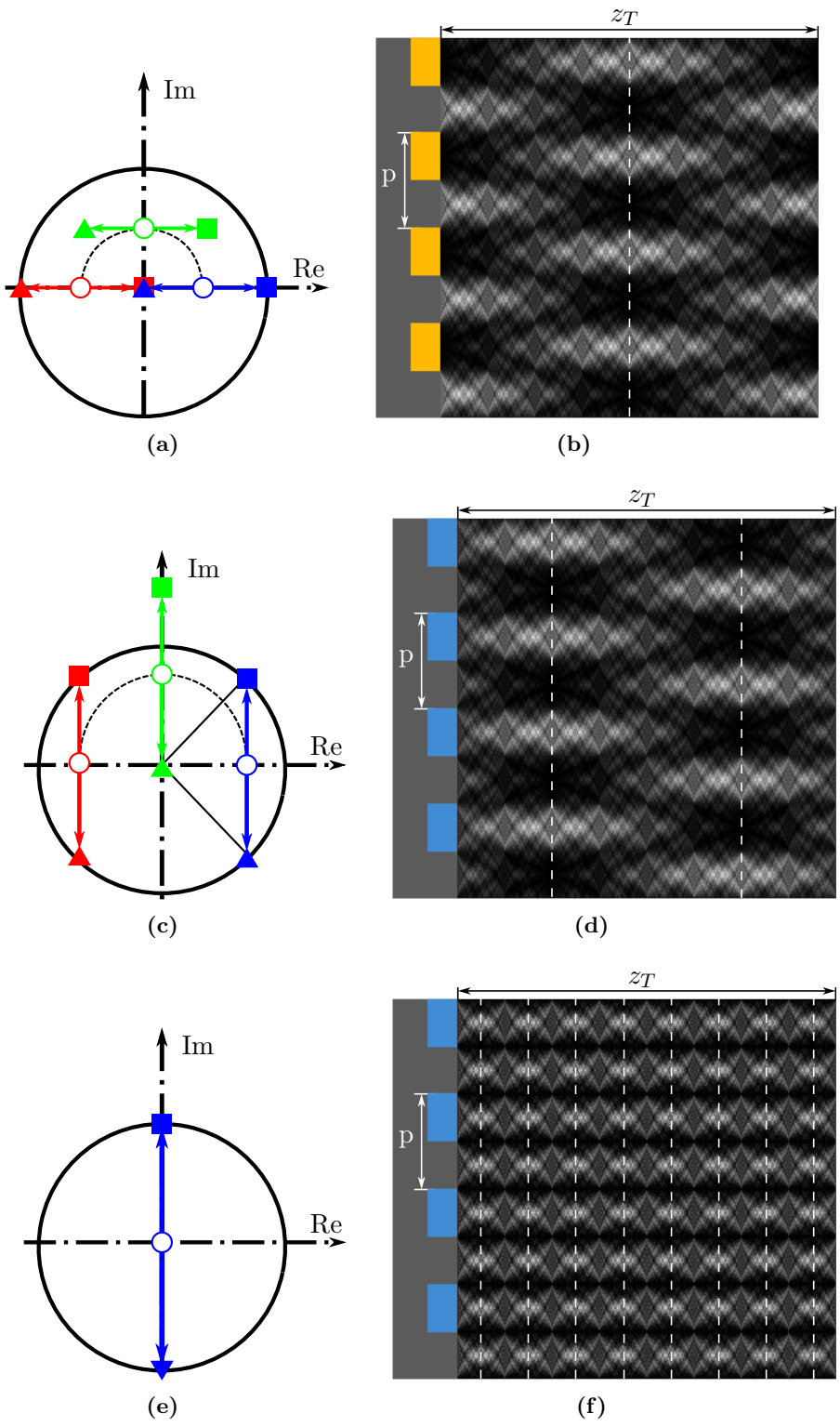

Figure 2.7: Complex plane representation and the Talbot carpets for pure absorption (a,b) and pure phase gratings with $\pi/2$ (c,d) and π (e,f) phase shifts. Figures were obtained by wavefield simulations written in Matlab. For all figures, the colormap is linear from black being equal to 0 to white equal to 3. The field of view of Talbot carpets is 4 mm horizontally and 10 μm vertically.

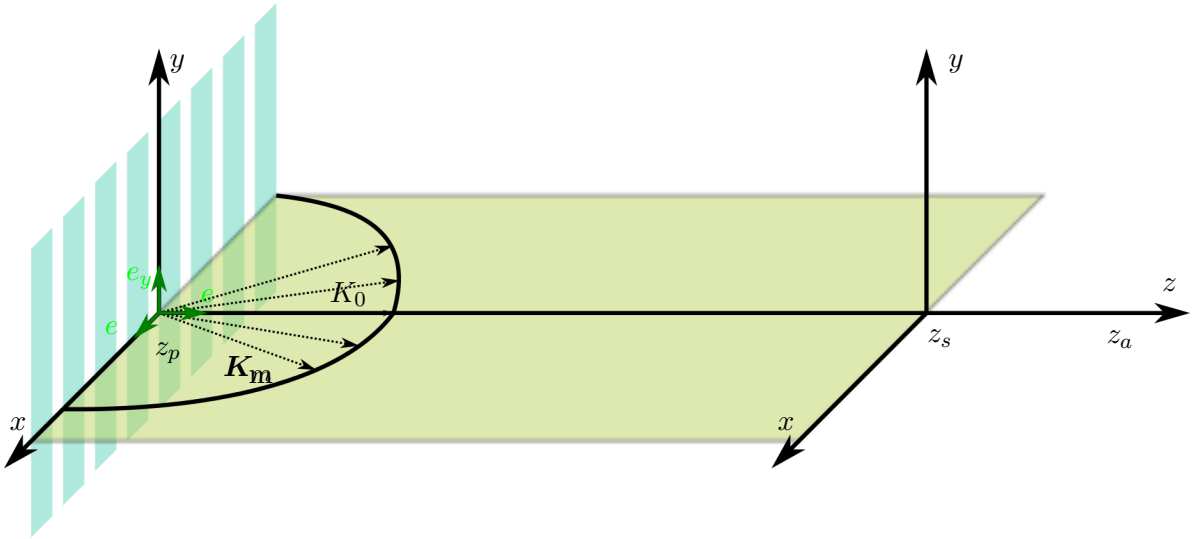

Figure 2.8: Propagation geometry and coordinate systems for grating interferometry: $\{u, v, w\}$ correspond to the specimen's fixed-body coordinate system, $\{x, y, z\}$ to the laboratory coordinate system with the corresponding unit vectors. $\boldsymbol{K}_0$ is the wave vector of the incident x-ray fronts. The cross section of the Ewald sphere and the grating rods define the wave vectors of the grating diffraction orders $\boldsymbol{K}_m$.

3. For the phase grating with π-shift, the self-imaging effect should be repeated more than a half or a quarter of the Talbot distance as can be seen from the complex plane representation. The self-imaging distances can be found from the simulation data in Fig. 2.7(f). The interference pattern behind the grating is reproduced at $\pi/8$ Talbot distances with the periodicity twice higher than original grating period.

2.4 Analyzer grating and Moiré effect

Let us now proceed from diffraction on a single phase grating and add a sample positioned before or after the phase grating (see Fig. 2.8). The diffracted wavefield behind the grating becomes perturbed by the specimen disturbance function: the x-ray transform that contains the phase and amplitude change $p(\boldsymbol{r}_\parallel) = p'(\boldsymbol{r}_\parallel) - ip''(\boldsymbol{r}_\parallel)$ (65). Within a sufficiently good approximation for grating interferometry, the specimen's x-ray transform $p(\boldsymbol{r}_\parallel)$ diffractionless propagates into a bundle of directions $\boldsymbol{K}_m$ of the plane-wave grating diffraction orders. Propagation without diffraction leads to

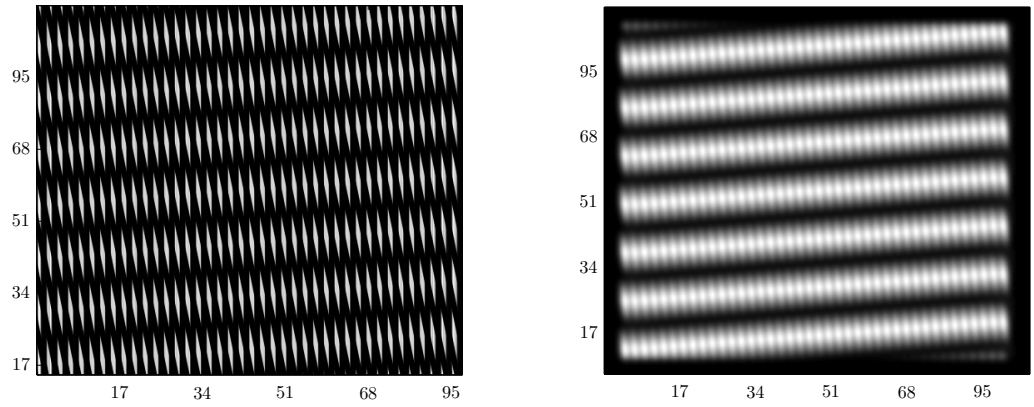

Figure 2.9: (a) Simulated Moiré fringes from two gratings separated by the Talbot distance in high resolution. The image axes are in μm. (b) The same Moiré pattern as in (a) but seen with an x-ray detector resolving 2.5 μm structures.

a geometrical projection. Due to the geometric intercept theorem, a non-zero angle between the $\boldsymbol{K}_m$ and the optical axis with increasing propagation distances Δz causes an increasing lateral shift $\Delta \boldsymbol{r}_\parallel = \Delta z \left[\boldsymbol{K}_{\parallel m}/K\right]$ in the x-ray transform projected along $\boldsymbol{K}_m$ onto the image plane. Thus from Eq. 2.21, the total perturbed wave field in the image plane at the position z_a consists of the superposition of field contributions of all perturbed grating diffraction orders:

$$E_P(\boldsymbol{r}_\parallel, z_a) = \sum_m T_m \ \exp\left(\, i(\boldsymbol{r}_\parallel \boldsymbol{h}_m - z'\, h_m^2/2K)\right) \ \exp\left(-ip(\boldsymbol{r}_\parallel + \tilde{z}\,[\boldsymbol{h}_m/K])\right). \quad (2.24)$$

Here $z' = z_a - z_p$ is the axial propagation distance between phase grating and image plane, and $\tilde{z} = z_a - max(z_s, z_p)$ denotes the axial propagation distance of the specimen disturbance with the grating diffracted field. Every summand in Eq. 2.24 comprises the contributions of the unperturbed grating diffraction order (first two factors), which are multiplied with a disturbance factor having the specimen's propagated x-ray transform in its exponent.

In linear approximation of $p(\boldsymbol{r}_\parallel)$ Eq. (2.24) can be rewritten in the form

$$E_P(\boldsymbol{r}_\parallel, z_a) = \exp\left(-ip(\boldsymbol{r}_\parallel)\right) \sum_m T_m \exp\left(-iz'\, h_m^2/2K\right) \exp\left(i\boldsymbol{h}_m \left\{\boldsymbol{r}_\parallel - \tilde{z}/K \boldsymbol{\nabla}_\parallel p(\boldsymbol{r}_\parallel)\right\}\right). \quad (2.25)$$

The sensitivity of a certain grating order with respect to the specimen is proportional to the scalar product of the reciprocal grating vector $\boldsymbol{h}_m$ with the local 2-D gradient vector of the specimen's x-ray transform $\boldsymbol{\nabla}_{\parallel} p(\boldsymbol{r}_{\parallel})$, and it is linearly magnified by the propagation distance $\tilde{z}$. Using the self-imaging properties of unperturbed grating-diffracted fields, the image plane will favorably be positioned at such suitable fractional Talbot orders, where propagation of the initially *phase* modulated wave field of the first grating has developed a strong *amplitude* modulation, and as a consequence a significant intensity modulation. The unperturbed intensity field of the grating can be expanded in to a Fourier series, $I_G(\mathbf{r}) = \sum_m I_m \ \exp(i\boldsymbol{h}_m \mathbf{r})$, and after incorporating the sample, the perturbed intensity pattern can be approximated by

$$I_P(\mathbf{r}) = \ \exp\left(-2p''_{\varphi,\theta}(\boldsymbol{r}_{\parallel})\right) \sum_m I_m \ \exp(i\boldsymbol{h}_m \widetilde{\mathbf{r}}) \tag{2.26}$$

with $\widetilde{\boldsymbol{r}} = \boldsymbol{r}_{\parallel} + \Delta\widetilde{\boldsymbol{r}}_{\parallel}$, where $\Delta\widetilde{\boldsymbol{r}}_{\parallel} = \widetilde{z}/K \ \boldsymbol{\nabla}_{\parallel} p'_{\varphi,\theta}(\boldsymbol{r}_{\parallel})$. This assumes that the effect of $\boldsymbol{\nabla}_{\parallel} p''_{\varphi,\theta}(\boldsymbol{r}_{\parallel})$ is subdominant and can be neglected.

Placing the second absorption grating into the image plane, the superposition of unperturbed intensity fringes of the phase grating and of the periodic intensity transmission function of the absorption grating, $A(\mathbf{r}) = \sum_l A_l \ \exp(i\boldsymbol{g}_l \mathbf{r})$, creates a characteristic Moiré fringe pattern, which then can be recorded in the detector plane, as shown in Fig. 2.9. This Moiré fringe pattern again becomes distorted if the specimen is introduced into the beam path. For sufficiently large pixel size, the perturbed Moiré fringe pattern (integrated over the grating periods) can be approximated as (1)

$$J(\mathbf{r}) \approx \sum_{m,l} I_{-l} A_l \ \exp\left(i\boldsymbol{h}_m \Delta\widetilde{\boldsymbol{r}}_{\parallel}\right) = \sum_{m,l} I_{-l} A_l \ \exp\left(i\boldsymbol{h}_m \ \widetilde{z}/K \boldsymbol{\nabla}_{\parallel} p'_{\varphi,\theta}(\boldsymbol{r}_{\parallel})\right), \tag{2.27}$$

and is later used for solving the inverse problem to reconstruct the object contrast functions.

2.5 The phase-stepping technique

The inverse problem in grating interferometry can be solved via different methods (22, 77, 79). Here, we apply a phase-stepping technique in order to retrieve absorption and phase information from the object (see Fig. 2.10). To do this, several interferograms with a different constant phase shift (phase of the interference pattern is varied

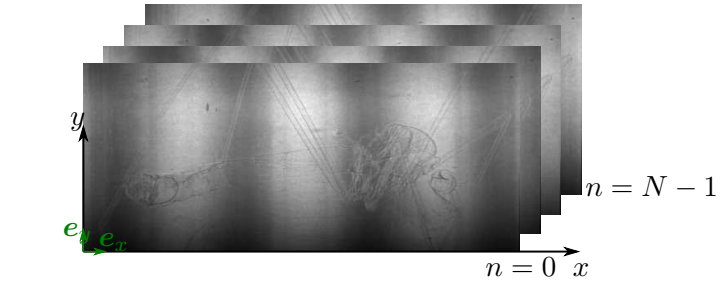

(a)

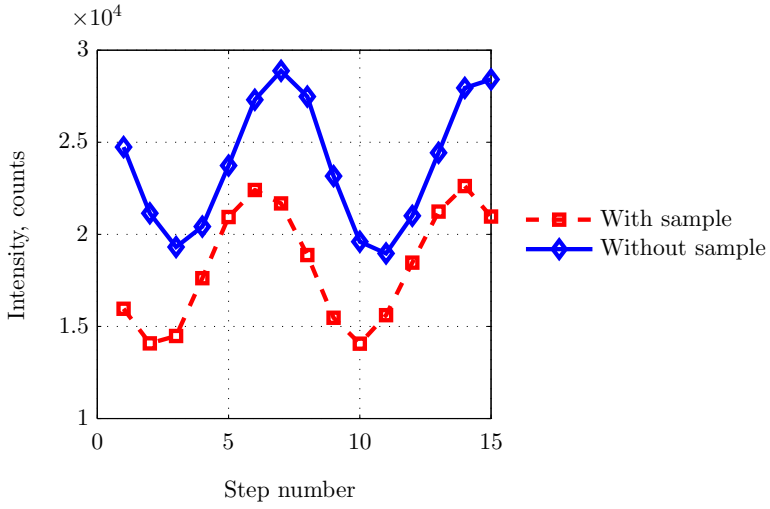

(b)

Figure 2.10: (a) A series of N interferograms in the (x, y) plane. Four Moiré fringes are shifted in x direction. (b) Phase-stepping curves for one pixel at (x,y) of the image with and without sample.

with respect to the absorption grating) are recorded and added to the reference interferometry pattern. For 1-D gratings, the phase-stepping technique is realized via displacing one of the gratings in the direction parallel to $\boldsymbol{e}_x$. Thus the perturbated N interferograms for grating displacements by $2\pi n/N$ are written as follows:

$$J_n(\mathbf{r}) \approx \sum_{m,l} I_{-l} A_l \, \exp\left(i \boldsymbol{h}_m \Delta \widetilde{\boldsymbol{r}}_{\|}\right) = \sum_{m,l} I_{-l} A_l \, \exp\left(i \boldsymbol{h}_m \, \widetilde{z}/K \boldsymbol{\nabla}_{\|} p'_{\varphi,\theta}(\boldsymbol{r}_{\|}) + \frac{h_m n}{N}\right), \tag{2.28}$$

Taking into account only the first diffraction orders ($l = \pm 1$), the well-known rules of ordinary two-beam interferometry can be applied. The differential phase map (the

gradient of the x-ray phase transform) may directly be determined from a summation over each of the N interferograms weighted by $\exp(-2\pi i n/N)$, where $n = 0, 1, 2, ..., N-1$, (1):

$$\triangle \boldsymbol{h}\, \widetilde{z}/K \boldsymbol{\nabla}_{\parallel} p'_{\varphi,\theta}(\boldsymbol{r}_{\parallel}) \approx \arg \left\{ \sum_{n=0}^{N-1} J_n(\mathbf{r}) \, \exp(-2\pi i \, n/N) \right\}. \tag{2.29}$$

If the grating displacement is equal to an exact multiple of the grating period for 2^M steps, we can analyze the series of the interferograms $\sum_{n=0}^{N-1} J_n(\mathbf{r}) \, \exp(-2\pi i \, n/N)$ for each pixel via Fourier analysis with respect to n. The extracted zero frequency component corresponds to the objects absorption, whereas the phase corresponding to the frequency equal to the displacement range in periods determines the differential phase of the object. One may also obtain the x-ray transforms of the effective scattering power $f(\boldsymbol{r})$, which results from the superposition of coherent Fresnel diffraction and the mesoscale diffuse scattering of the specimen (69). The effective scattering power will be further named as the dark-field contrast in analogy with optical microscopy (33).

From the Eq. 2.29, the range of the detectable phase shift (phase sensitivity) in grating interferometry depends on the reciprocal grating vector $\boldsymbol{h}$, wave vector K, and distance between a phase and an absorption grating $\widetilde{z}$. The larger the distance between grating $\widetilde{z}$ (Talbot order n) and the smaller the wave vector K and the reciprocal grating vector $\boldsymbol{h}$ the smaller phase shift are detectable by grating interferometry.

Thus three object contrast functions are accessible with grating interferometry: absorption, phase, and dark-field contrasts.

2.6 3-D reconstructions

In computed tomography, an increase of spatial resolution for a fixed number of pixels goes together with a decreasing field of view of the detector. This circumstance increasingly restricts the maximum lateral dimensions of the specimen. For objects with dimensions below the detectors effective field of view, for larger samples one has to accept compromises, for example to trim the specimen to fit the field of view by sample dissection, or by applying modified scanning schemes. Synchrotron radiation computed laminography represents such a modified scanning scheme which allows examining, without sample cutting, a class of specimen where lateral dimensions strongly exceed the effective field of view (flat specimens such as electronic circuit boards).

Reconstructions in computed tomography and laminography both rely on the set of a series of projections images where object is rotated around axis w by ϕ (Fig. 2.11).

Existing reconstruction algorithms are iterative reconstruction methods (34) and filtered back projection algorithms such as the Feldkamp-Davis-Kress (30). Although they are successfully applied to imaging in different application fields (6, 32, 76), their memory and time consumption is still prohibitively high in real applications (92). Here, a computationally efficient reconstruction procedure based on filtered backprojection adapted to the computed laminography with grating interferometry acquisition geometry is developed.

The procedure for reconstructions of a 3-D distribution of a refractive index in grating interferometry can be described as following: (a) retrieval of 2-D absorption, differential phase, and dark-field contrast images from the stepping scans of the Moiré fringe pattern (previous section), go into (b) reconstruction of the 3-D tomographic/laminographic object functions for the specimen's region of interest.

The estimation of the unknown 3-D object functions $\rho(\boldsymbol{r})$ (which could be the linear attenuation coefficients $\mu(\boldsymbol{r})$, the real part of the refraction index $\delta(\boldsymbol{r})$, or the effective scattering power $f(\boldsymbol{r})$) of a series of projections reconstructed via equation 2.29 from the measured phase-stepping scans under constant θ but different rotation angles φ is performed by using the fundamental Fourier slice theorem (45).

Here, we develop 3-D reconstructions for the laminographic geometry. It differs from the tomographic geometry as the object is tilted with respect to the optical axis by the angle θ. Thus, the reconstruction procedure will be valid for tomography as well, with $\theta = 90$ being a particular case of laminography.

For the laminography case, the 2-D Fourier transforms $\mathcal{P}_{\varphi,\theta}(k_x, k_y)$ of the projections $p_{\varphi,\theta}(x, y)$ correspond to the cross-sections of the 3-D Fourier transform $\mathcal{M}(k_u, k_v, k_w)$ of the object functions $\rho(\boldsymbol{r})$ through the reciprocal image plane $(\boldsymbol{e}_x \times \boldsymbol{e}_y) \cdot \boldsymbol{k} = 0$, that is

$$\mathcal{P}(k_x, k_y) = \mathcal{M}(k_x \cdot \boldsymbol{e}_x + k_y \cdot \boldsymbol{e}_y) \ . \tag{2.30}$$

Since in the case of laminography in the reciprocal space the 2-D Fourier transforms of the projections are inclined from the $\boldsymbol{k}_w$ direction by the laminographic angle θ, the set of unbounded projections for different rotation angles does fill (and even oversamples) the region outside a double cone with the opening angle π-2θ, while internal regions of the cone remain empty (non-sampled frequencies) (50). In consequence,

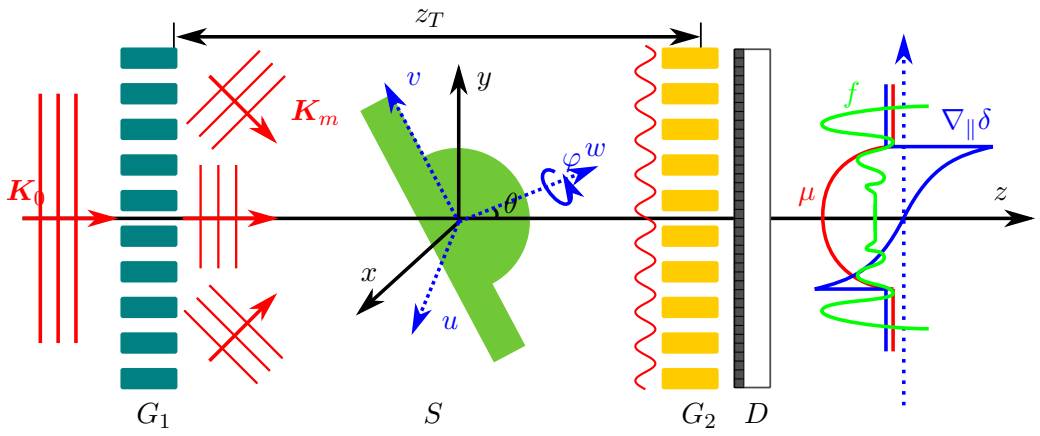

Figure 2.11: Schematic representation of the combination of Talbot grating interferometry with laminography. The phase grating G_1 splits incoming x-rays into diffraction orders which are disturbed by sample S. The absorption grating G_2 positioned at the self-imaging distance converts the interference pattern from the phase grating into a Moiré pattern, detected then by an x-ray detector D.

laminography reconstruction is an ill-posed inverse problem. The reconstruction process may provide only approximate object functions, while the reconstruction of the accurate object function is impossible.

At this point we remind that full tomographic scans for such type of laterally extended samples cannot acquire the complete frequency domain, and, beside representing also an ill-posed inverse problem, additionally suffer from strongly angle-dependent transmission values (93).

The analytical reconstruction of the object function $\rho(\boldsymbol{r})$ from its x-ray transforms can be performed by generating a so-called *compound image* g via back-projection and by its convolution with an *inverse filter function* h (50). The inverse filter function h depends on the 3-D point spread function which is determined by the experimental geometry.

Here the relation between the compound image and projection is described by[1]

$$\int_0^{2\pi} g_{\varphi,\theta}(u,v,w)\, d\varphi = \int_0^{2\pi} p_{\varphi,\theta}\left(T^{[1,3]}_{u,w}(\theta,\varphi)\cdot(u,v,w)^T\right) d\varphi \ , \tag{2.31}$$

[1] $^{[1,3]}$ denotes a matrix where only the 1st and 3rd row of the matrix T is retained.

with the laminographic transformation matrix

$$T_{u,w}(\theta,\varphi) = R_u(\theta-\pi/2)\cdot R_w(-\varphi) = \begin{bmatrix} \cos\varphi & -\sin\varphi & 0 \\ \sin\theta\cdot\sin\varphi & \sin\theta\cdot\cos\varphi & \cos\theta \\ \cos\theta\cdot\sin\varphi & \cos\theta\cdot\cos\varphi & -\sin\theta \end{bmatrix}. \quad (2.32)$$

Since

$$g(\boldsymbol{r}) = \{\rho\otimes h\}(\boldsymbol{r})\ , \quad (2.33)$$

where $\otimes$ denotes a 3-D convolution, one obtains a *reconstruction equation*

$$\rho(\boldsymbol{r}) = \mathcal{F}_3^{-1}\left\{\mathcal{M}(\boldsymbol{k})\right\} = \mathcal{F}_3^{-1}\left\{[\mathcal{G}\cdot\bar{\mathcal{H}}](\boldsymbol{k})\right\} = \left\{g\otimes\bar{h}\right\}(\boldsymbol{r})\ , \quad (2.34)$$

with $g = \mathcal{F}_3^{-1}\{\mathcal{G}\}$ and $\bar{h} = \mathcal{F}_3^{-1}\{\bar{\mathcal{H}}\} = \mathcal{F}_3^{-1}\{1/\mathcal{H}\}$.

Two reconstruction approaches can be employed for the laminography case: the so-called *filtering after backprojection* and *filtering before backprojection* (64). Filtering before backprojection has advantages concerning time and memory consumption and it is based on the relation

$$\left\{\mathcal{G}_{\varphi,\theta}\cdot\bar{\mathcal{H}}\right\}(\boldsymbol{k}) = \left\{\mathcal{P}_{\varphi,\theta}\cdot\bar{\mathcal{H}}_{\varphi,\theta}\right\}(T_{u,w}^{[1,3]}(\theta,\varphi)\cdot\ \boldsymbol{k})\times\delta(T_{u,w}^{[2]}(\theta,\varphi)\cdot\ \boldsymbol{k}), \quad (2.35)$$

which holds when $\bar{\mathcal{H}}_{\varphi,\theta}$ is a 2-D section of the 3-D inverse filter function $\bar{\mathcal{H}}$ in the reciprocal space through a plane defined by a projection $\mathcal{P}_{\varphi,\theta}$ as

$$\bar{\mathcal{H}}_{\varphi,\theta}(k_x,k_y) = \bar{\mathcal{H}}(T_{u,w}^{-1}(\theta,\varphi)\cdot(k_x,0,k_y)^T). \quad (2.36)$$

According to the above statement, the 3-D convolution in equation 2.34 can be substituted by 2-D convolutions of projections with the filter function. The filter function can be derived from the 3-D inverse filter, which are less time consuming and leading to

$$\mathcal{F}_2\{\bar{h}_{\varphi,\theta}\} = \bar{\mathcal{H}}_{\varphi,\theta}(k_x,k_y) = \frac{\sin\theta}{2}|k_x|\ . \quad (2.37)$$

Moreover, since the filter neither depends on the laminographic rotation angle φ nor the reciprocal vector component k_y, the projection filtering can be efficiently implemented by a series of 1-D fast Fourier transforms.

Let

$$\mathcal{Q}_{\varphi,\theta}(k_x,k_y) = \left\{\mathcal{P}_{\varphi,\theta}\cdot\bar{\mathcal{H}}_{\varphi,\theta}\right\}(k_x,k_y) \overset{\mathcal{F}_2}{\Longleftrightarrow} q_{\varphi,\theta}(x,y) = \left\{p_{\varphi,\theta}\otimes\bar{h}_{\varphi,\theta}\right\}(x,y) \quad (2.38)$$

be a *filtered projection*. Applying (2.36), the reconstruction equation (2.34) can be rewritten in the following two forms

$$\rho(\boldsymbol{r}) = \mathcal{F}_3^{-1}\left\{\int_0^{2\pi} \underbrace{\mathcal{Q}_{\varphi,\theta}(T_{u,w}^{[1,3]}(\theta,\varphi)\cdot\boldsymbol{k})\,\delta(T_{u,w}^{[2]}(\theta,\varphi)\cdot\boldsymbol{k})}_{\mathcal{M}_{\varphi,\theta}(\boldsymbol{k})}\,d\varphi\right\} = \int_0^{2\pi} q_{\varphi,\theta}(T_{u,w}^{[1,3]}(\theta,\varphi)\cdot\boldsymbol{r})\,d\varphi\ . \tag{2.39}$$

The above equation offers two fundamental ways to implement a reconstruction procedure. The reconstruction can be performed either directly in reciprocal or in the real space. For reconstructions of the experiments in this thesis the second approach was used.

It should be noted that equation 2.39 can be directly applied for the reconstruction of the object function $\mu(\boldsymbol{r})$. The reconstruction of the object phase map $\delta(\boldsymbol{r})$ from the phase gradient projections requires an adaption of the filter function (equation 2.37).

$$\mathcal{F}_2\{\bar{h}_{\varphi,\theta}\} = \bar{\mathcal{H}}_{\varphi,\theta}(k_x,k_y) = \frac{\sin\theta}{2}|k_x|. \tag{2.40}$$

The same conventional filter function holds for effective scattering power $f(\boldsymbol{r})$, where for quantitative reconstruction, a parameter defined by the sensitivity of the grating interferometry setup is included (85).

$$\mathcal{F}_2\{\bar{h}_{\varphi,\theta}\} = \frac{-p^2}{2\pi^2 z_T^2}\frac{\sin\theta}{2}|k_x|. \tag{2.41}$$

The differential phase map determined from Eq. 2.29 needs to be integrated along the scanning axis x before being processed by computed laminography algorithms. To avoid linear artifacts resulting from the integration we apply a filter function similar to the case of differential phase microscopy with visible light (29), corresponding to the Hilbert transform in real space (70):

$$\mathcal{F}_2\{\bar{h}_{\varphi,\theta}\} = \begin{cases} 0 & \text{for } k_x = 0 \\ \frac{\sin\theta}{2}\frac{1}{2\pi i}sgn(k_x) & \text{elsewhere} \end{cases} \tag{2.42}$$

Applying the reconstruction procedure to the recorded projections with the corresponding filter functions, absorption, phase, and dark-field 3-D volumes can be reconstructed from the same data set.

2.7 Partial coherence effect

So far, we described the forward problem and the inverse problem of 3-D imaging based on grating interferometry. This theory (based on plane wave approximation) is sufficient to understand the principles of grating interferometry and retrieve three object contrast functions.

In practice also the properties of the source, gratings, and x-ray detector would influence the performance of grating interferometry and is thus crucial for imaging. While x-ray gratings and detector depend on the grating interferometer design, the properties of the x-ray source are given by the facility and have to be considered beforehand of any instrumentation.

From the theory described above we can conclude that the two main phenomena in grating interferometry are the Talbot and Moiré effects. The strength of the Talbot effect behind the grating depends on the phase relations between all diffraction orders, thus on the degree of coherence of the incoming x-rays. As the contrast of any fringes is known as visibility (10), we will distinguish effects in grating interferometry by following notations: the *interference curve* - is the interference pattern behind a phase grating at the Talbot order (Fig. 2.12 (a)), the *transmission curve* is reffed to the transmission function of the analyzer grating, and the *contrast curve* is a convolution of the interference curve with the transmission function of the analyzer grating laterally shifted according to the phase-stepping technique, see Fig. 2.12 (c).

The strength of the Moiré effect is determined by both: the visibility of the interference pattern and transmission of the second grating, further called as the visibility of the contrast curve. On Fig. 2.12 typical interference curve, transmission function of the absorption grating, and contrast curve are shown.

The properties of the x-ray source affect primarily the visibility of the interference curve and as a secondary effect the visibility of the contrast curve. In this section we will consider influence of the source properties on the interference pattern downstream the phase grating.

In our context, relevant properties of the x-ray source are source size, energy spectra, and flux density. While the last one would affect only the exposure time required for imaging, x-ray coherence (source size and energy or energy spread) defines the contrast

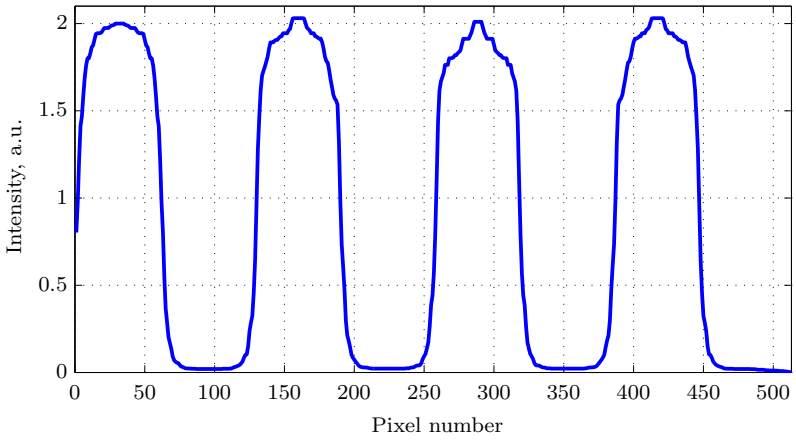

(a) The interference curve

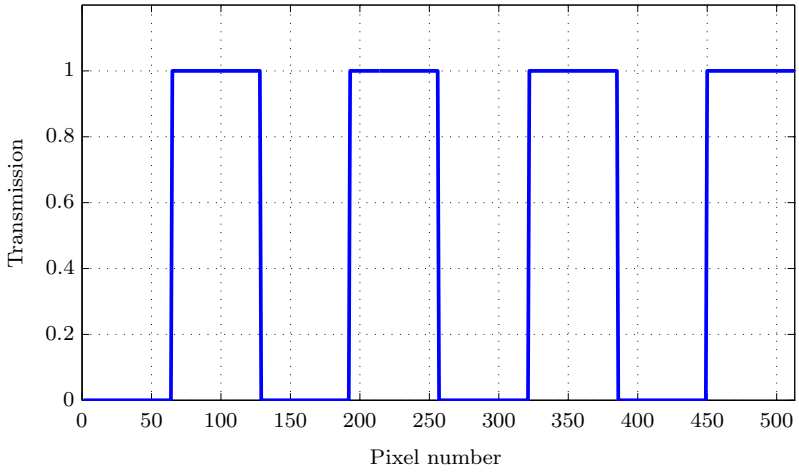

(b) The transmission function of an absorption grating

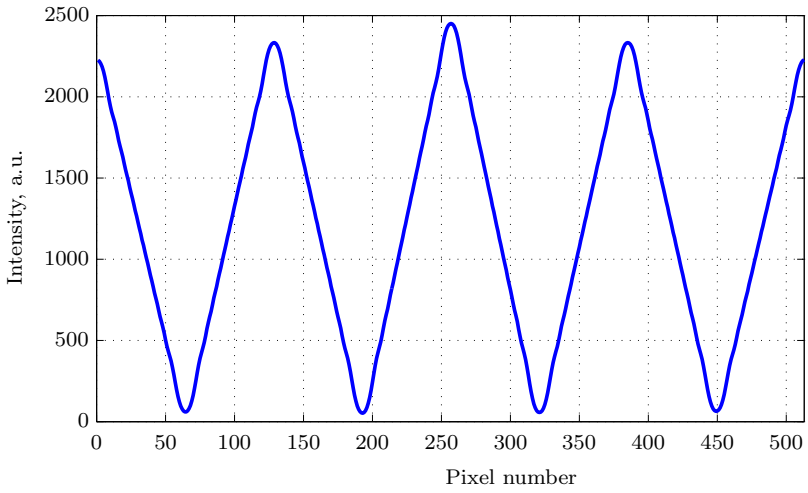

(c) The contrast curve

Figure 2.12: (a) The interference curve at the Talbot distance of the phase grating. (b) The ideal transmission function of the absorption grating. (c) Resulting from convolution of (a) and (b) contrast curve, demonstrating contrast of the Moiré fringes. Simulations have some numerical artifacts.

of the interference pattern. For simplicity, let us discuss the effect of monochromaticity and limited transverse coherence length separately.

Monochromaticity

The monochromaticity is determined by the energy spread of the x-ray wavefront as $\frac{\Delta\lambda}{\lambda}$ is the deviation from the original (desired) λ (43). The degree of monochromaticity of the x-ray beam will affect diffraction on gratings in three ways: 1) the grating diffraction efficiency will be reduced, 2) the waves of the same grating diffraction orders for different λ will propagate under different angles, Eq. 2.23, and as a consequence 3) the self-imaging effect will take place at a different fractional Talbot distance for different λ (78). Imposed by the temporal coherence, the difference in diffraction efficiency and angles would result in a superposition of the Talbot carpets for different wavelengths with a shift of maxima along the optical axis z. This effect will increase with the propagation distance, resulting in higher loss of visibility for higher Talbot orders.

According to the contrast transfer function Eq. 2.16 and Eq. 2.21 the Talbot effect for phase gratings varying along z is:

$$C \propto \sin\left(\frac{\pi}{2} n(2m-1)^2 \frac{\Delta\lambda}{\lambda}\right), \tag{2.43}$$

where n is a Talbot order and m is the diffraction order of the grating. Only $\Delta\lambda$ smaller than the period of the sine wave would allow to use self-imaging effectively (87), thus the minimum degree of monochromaticity required for grating interferometry is:

$$\Delta\lambda \leq \frac{\lambda}{n(2m-1)^2}. \tag{2.44}$$

The higher the Talbot order n, the higher degree of monochromatisation is required. To demonstrate the influence of monochromaticity on the propagation of the interference pattern behind the phase grating, Talbot carpets for x-ray energy spread $\Delta\lambda/\lambda$ of 10^{-3}, 10^{-2}, and 10^{-1} were simulated. The energy spread of 10^{-3} would require use of a double crystal monochromator (Si111), 10^{-2} to a double multilayer monochromator and 10^{-1} to the filtered x-ray beam from a bending magnet (see Fig. 2.13 (a)). Talbot carpets were simulated for $\pi/2$-shift phase grating over three Talbot orders, corresponding to six fractional Talbot orders where self-imaging takes place (marked by white lines) in Fig.2.13 (b),(c), and (d). The visibility of the interference curve

along the propagation axis is shown on Fig. 2.13 (e). Please note that high frequency oscillations are result of numerical simulations (high sampling rate, limited field of view and size of a phase grating) and are not considered as an affect of propagation. One observes a decrease of visibility of the interference curve with each next Talbot order. The effect is more noticeable for the filtered white beam with $\Delta\lambda/\lambda$ 10^{-1}. Yet, considering ± 1 being the main diffraction orders, even for a Talbot order $n = 5$, a bandwidth of 10^{-1} is still acceptable. This tolerance to the bandwidth makes grating interferometry most promising for use in x-ray laboratory sources.

Transverse coherence

The transverse coherence is determined by the spread of $\boldsymbol{K}_{||}$ (divergence) in the direction of propagation. In first approximation, the degree of transverse coherence depends on the source size D and the distance R in which it propagates until the phase grating. The transverse coherence length is defined as:

$$L_T = \frac{\lambda}{2}\frac{R}{D}. \tag{2.45}$$

The incident mutual intensity at two points $\boldsymbol{x}_1$ and as $\boldsymbol{x}_2$ a function of the source intensity $S(\boldsymbol{r})$ of an extended incoherent source is given by the Van Cittert-Zernike theorem (10, 19):

$$J_{inc}(\boldsymbol{x}_1, \boldsymbol{x}_2) = \exp i\frac{\pi R}{\lambda}(x_1^2 - x_2^2) \int S(\boldsymbol{r}) \exp\left[-2\pi i \boldsymbol{r}\frac{(x_1 - x_2)}{\lambda R}\right]. \tag{2.46}$$

The extended source size affects the interference pattern behind the phase grating by blurring the images.

Let us interpret the influence of the transverse coherence length on grating diffraction in a simple geometrical manner (see Fig.2.14 (a)). The propagation angles of the different diffraction orders are determined according to Eq. 2.23. If the transverse coherence length of the primary beam is on the order of the grating period, the self-imaging effect takes place at the Talbot order $n = 1$ only. To make the self-imaging effect happen at higher Talbot orders, diffraction orders from grating lamellas further apart have to interfere. Thus, the transverse coherence length has to be longer. From Fig. 2.14, we can conclude that the minimum transverse coherence length for which the self-imaging effect behind the grating is visible can be defined as:

$$L_T \geq n(2m - 1)p. \tag{2.47}$$

The larger L_T, the better is the interference between different diffraction order and the higher the visibility of the interference curve.

To demonstrate the effect of transverse coherence length on the interference behind the phase grating, Talbot carpets for monochromatic x-ray source with extended source sizes of 50, 200, and 800 μm were simulated. The source sizes chosen for simulations correspond to the imaging beamlines at ANKA (TopoTomo beamline) and ESRF (ID19). The Talbot carpets were calculated for a phase grating with a $\pi/2$ phase shift and a source to grating distance of 200 m.

We observe that even for 50 μm source size the interference pattern at higher Talbot orders become blurred. With the increase of the source size, the interference is getting blurred already at shorter distances. The visibility of the interference pattern along the optical axis is shown on Fig. 2.14 (e) for all three cases. For a source size of 800 μm for example, grating interferometry would be possible only at the first Talbot order $n = 1$.

The conditions given by Eq. 2.44 and Eq. 2.47 are the minimum requirements for the use of grating interferometry and it is limited only by the number diffraction orders m and the Talbot order n. However, the higher spatial and temporal coherence of the x-ray source size the higher is the visibility of the interference curve, providing better image quality for imaging. The limited coherence properties of the x-ray beam will not be considered further in the theoretical framework, however they will be discussed and evaluated later in the implementation and optimization of grating interferometry.

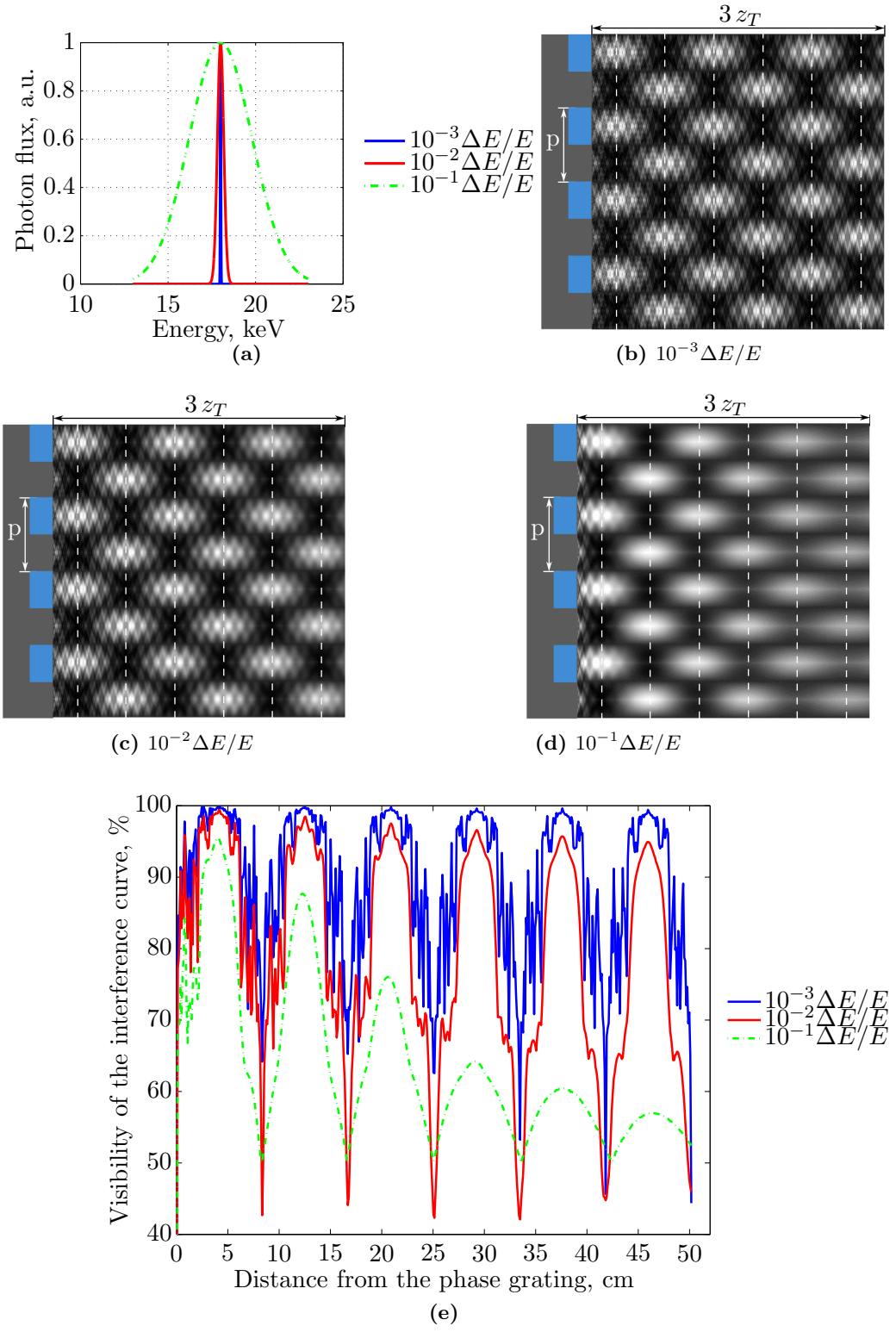

Figure 2.13: (a)Three energy spectra are considered in the simulations: $\Delta E/E$ of 10^{-3}, 10^{-2}, and 10^{-1}. The corresponding Talbot carpets behind a phase grating with a phase shift of $\pi/2$ are shown in (b),(c), and (d). (e) Visibility of the interference curve with respect to the propagation distance behind the phase grating. The colormap is linear from black being equal to 0 to white being equal to 3.

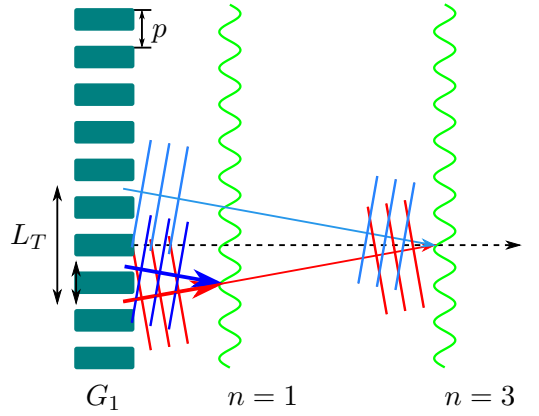

(a)

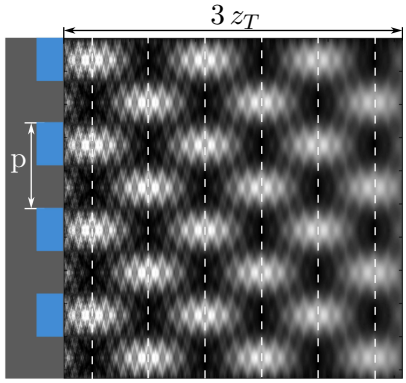

(b) 50μm

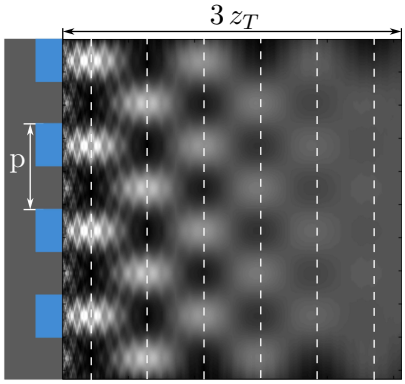

(c) 200μm

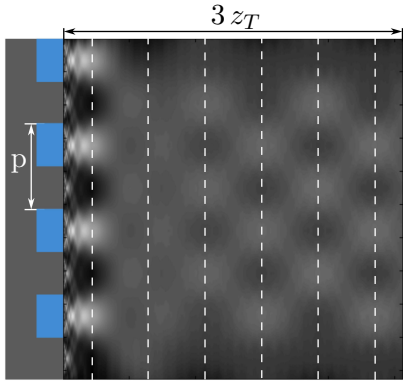

(d) 800μm

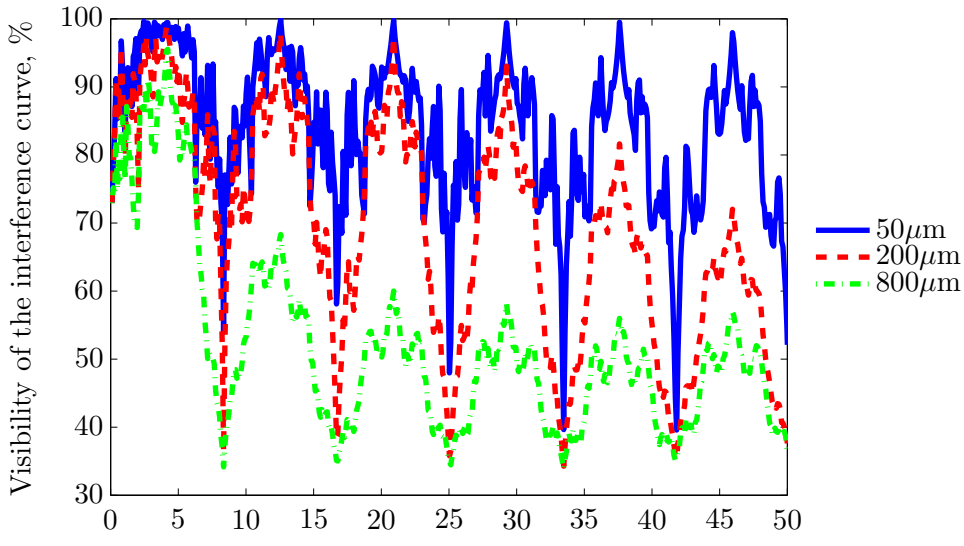

(e)

Figure 2.14: (a) Schematics of the transverse coherence length required to produce the interference pattern at the Talbot order n. (b),(c), and (d) Talbot carpets behind a phase grating with a phase shift of $\pi/2$ simulated for source sizes of 50μm, 200μm, and 800μm. The colormap is linear from black being equal to 0 to white being equal to 3.

3 The gratings

Contents

Fabrication of optics for x-rays has been a challenge for the last century. Weak interaction of x-rays with matter allow to use a limited number of materials which has high δ/β ratio. Meanwhile, short x-ray wavelength requires structures of micrometer size for the optical components. In this chapter, we briefly describe a recently emerging technique for the fabrication of diffraction gratings. It is based on a fabrication technology developed at KIT and used to create high-aspect-ratio structures. Here, we summarize the currently available gratings and the main parameters required for imaging with grating interferometry. Procedures for the quality assurance of both phase and absorption gratings in terms of gratings thickness, thickness inhomogeneity, period, and period distortions are discussed. A novel design for fabrication of phase gratings with various periods is evaluated and experimentally demonstrated.

3.1 Grating fabrication

Within this work, both phase and absorption gratings were produced by the Institute for Microstructure and Technology using deep x-ray lithography available at ANKA. The fabrication process is called LIGA - a German acronym for "Lithographie, Galvanoformung und Abformung". As a substrate for the grating microstructures, 4-inch Si wafers with the thickness of 525 μm were used, which are conventional for microstructure technology. For higher adhesion, it is first covered with a titanium layer of 2.5 μm

Parameters	Phase grating	Absorption grating
Area	20 mm x 60 mm, 70 mm diameter	20 mm x 60 mm, 50 mm diameter
Material	SU8, Ni	Au
Substrate	Si, Kapton foil	Si, Kapton foil
Si thickness	200 μm, 525 μm	200 μm, 525 μm
Duty cycle control	0.5 $\pm$ 0.03	-
Period [μm]	2.4, 3.57, 4.37, 4.8, 5.4, 5.8, 10 and 24.39	the same as G_1
Height variation	$\pm$ 5% over the patterned area	$\pm$ 10% over the patterned area
Design	1-D/2-D	1-D/2-D
Aspect ratio	5-30	up to 100

Table 3.1: Parameters of available gratings fabricated by deep x-ray lithography (73).

thickness exhibiting a thin oxidized layer on top (28), see Fig.3.1. In the next step, the photoresist (IMT uses MR-X) from micro resist technology is applied on top of the titanium oxide. In order to structure the resist, x-ray masks consisting of thin titanium membrane and gold absorber lines fabricated by electron-beam lithography and subsequent electroforming are used. The mask comprises certain design parameters: grating period, duty cycle, and layout of the structures independent of whether it is later used as a phase or an analyzer gratings. After deep x-ray lithography (Fig.3.1 (a)), the non-exposed areas are removed by the development process (Fig.3.1 (b)). At this step, the fabricated photoresist grating can already be used as phase grating in the experiment if the thickness of the photoresist corresponds to the desired phase shift (π or $\pi/2$). In order to fabricate the analyzer grating, the areas which were removed are then filled electrochemically with a metal layer (Fig.3.1 (c)). Here, we can use nickel for fabrication of phase gratings due to its favorable δ/β ratio or gold for analyzer grating due to its high absorption.

The x-ray gratings currently available for phase contrast imaging are summarized in Table 3.1. The most crucial parameters for the phase gratings are height, height variation, duty cycle, and duty cycle variation as they define the Talbot carpet behind the grating. For the absorption grating, these parameters are period, height (100% x-ray absorption) and height variation. All of these parameters influence the performance of the grating interferometer and thus the image quality.

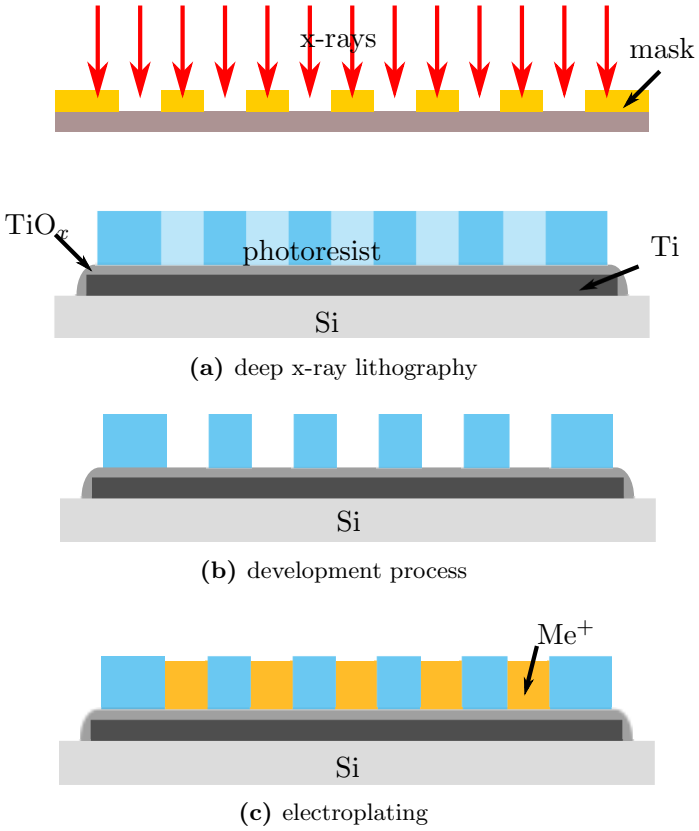

(a) deep x-ray lithography

(b) development process

(c) electroplating

Figure 3.1: Sketch of the gratings fabrication steps: deep x-ray lithography and electroplating.

One of the main challenges in gratings fabrication is to achieve the high aspect ratio of the absorption grating required for low dose (hard x-ray) imaging in medicine. Thus, the fabrication process of the gratings is in constant development searching for improvements of the grating quality. The quality control (assurance) and characterization is an essential part pinning down modification of the fabrication process. These challenges will not be described in detail, but a short outline of the characterization methods and the gratings development which was performed within this work will be given.

3.2 Grating characterization

3.2.1 Phase grating

As was already mentioned, phase gratings for grating interferometry have to meet the following requirements: 1) produce a specified phase shift, 2) have a duty cycle of 0.5 (currently there are attempts to use other duty cycles (16)), and 3) have an active area equal to the beam size to be used in the experiment. While the last one is easy to fulfill for synchrotron facilities where the typical beam size is a few millimeters vertically and horizontally, the other two requirements can not be perfectly met.

First of all it is hard to control the thickness of the grating during the electroplating. All gratings have a thickness variation, which is undefined and possible to detect only after fabrication was done with SEM (47). Variation in the thickness of the phase grating would lead to a different number of diffraction orders and their efficiency for each groove, resulting in lower visibility of the interference pattern at the Talbot distance. The same would hold for a variation of the duty cycle over the grating area.

We investigated these parameters by high resolution (1 μm size of resolvable feature) x-ray radiography. Since the gratings are designed to be pure phase shifting elements, it is not possible to visualize them in transmission geometry within hard x-ray energy range as in conventional radiography. However, scanning along the optical axis, the 1^{st} Talbot distance is detected and the self-image at this position is acquired as seen in Fig. 3.2 (a). Please note that while the grating lamellas are results of a self-imaging, supporting bridges are result of propagation effect and thus appear more pronounced. The x-ray radiography image shows single grating lamellas, reinforcing bridges, distortion of lamellas close to the bridges, and contrast differences over the field of view. The fact that we can detect the self image means by itself that the thickness, duty cycle, and thickness inhomogeneities of the grating are acceptable for phase contrast imaging. For comparison Fig. 3.2 (b) shows an optical microscope image of the phase grating. While both images depict very well the layout of the grating (bridges, period, duty cycle), the distortions nearby the bridges and the loss of contrast in a few grating regions (top right part of Fig. 3.2 (a)) can only be observed by imaging the phase grating with x-rays.

It is important to mention that it is possible to characterize a phase grating by measuring visibility of the interference curve (see Section 2.7). For the phase grating

in Fig. 3.2 the visibility of the interference curve is 24.12±0.86%. Please note that the visibility of the contrast curve which is typically used to conclude upon performance of grating interferometry, will also be influenced by the absorption grating and thus the measurements will be indirect, giving no conclusions on the phase grating parameters.

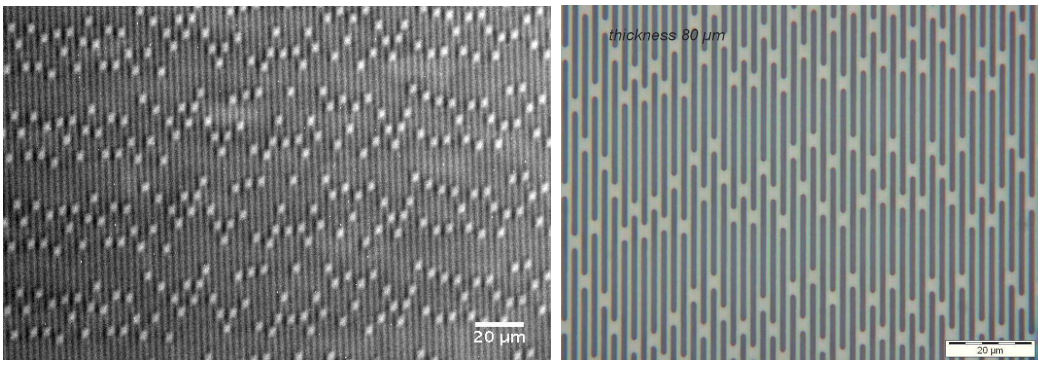

(a) **(b)**

Figure 3.2: (a) High resolution x-ray radiography of the phase grating acquired at the TopoTomo beamline, (b) Optical microscope image of the phase grating, courtesy to E. Reznikova.

3.2.2 Absorption grating

The height and the height variations of the absorption grating are the main parameters which influence image quality. The grating height determines the visibility of the contrast curve behind the phase grating, resulting in the visibility of the contrast curve or Moiré pattern. The influence of the absorption grating thickness on the visibility of the contrast curve can be found from the transmission function of the absorption grating and expressed by:

$$Visibility = \frac{1 - \exp(-\mu l)}{1 + \exp(-\mu l)}, \tag{3.1}$$

where l is the thickness of the absorption grating and μ is it's mass attenuation coefficient. For hard x-ray energies, the height of the absorption grating has to exceed $50\,\mu$m, resulting in a high aspect ratio which is difficult to fabricate. Reinforcement bridges need to achieve this high aspect ratio would result in a decrease of the visibility of the contrast curve.

Let us consider absorption gratings of different thicknesses with and without bridges. Phase gratings for 19, 29, 36, and 52 keV and 7 different absorption gratings were fabricated. The thickness of the absorption grating was then measured by SEM. Absorption gratings fabricated with the standard mask (bridges) are 60, 83, 86, 90, 95, and 100 μm thick and the new "sun-rays" design having reinforced structures inclined by 45 degrees (details of the design are described in (47)) has a thickness of 75 μm. The visibility values of the contrast curve for each phase grating at in the grating interferometer was measured at the ID19 beamline of the ESRF and is shown in Fig. 3.3.

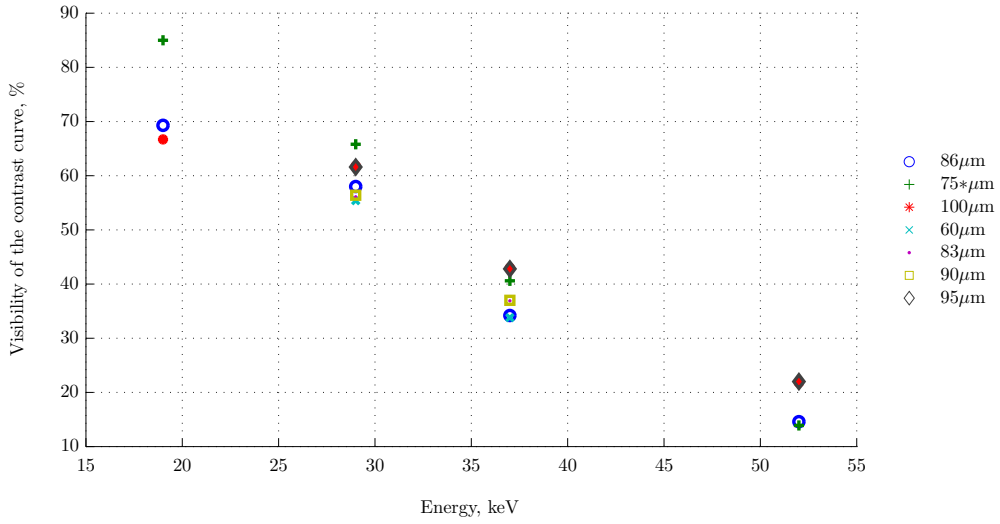

Figure 3.3: Experimental visibility of the contrast curve for absorption gratings of different thickness at discrete x-ray energies. The new "sun-rays" layout grating is marked by *.

For the x-ray energy of 19 keV, all absorption gratings should absorb 100% of the incoming x-rays. Due to the transmission by the bridge areas (≈10 %) as well as due to the non-ideal visibility of the interference pattern from the phase grating, the standard gratings reach only 70% visibility of the contrast curve. This value is significantly improved by the bridge free "sun-rays" design, which reaches a visibility of the contrast curve of approximately 85% at 19 keV. At higher x-ray energies the transmission of the absorption gratings becomes higher, resulting in lower visibility of the contrast curve. At 52 keV, the highest visibility is achieved with the thickest gratings which represent the limit of highest visibility for the current design and fabrication process of absorption

gratings.

Furthermore, the theoretically expected visibility of an analyzer grating of 100 μm thickness (measured by SEM) was calculated without taking a phase grating into account and measured as a function of x-ray energy using a phase grating optimized for an x-ray energy of 54 keV. The results of the measurements are shown on Fig. 3.4 in comparison with the theoretically predicted values. We can see that the grating interferometer performs very well at energies slightly lower than the designed energy due to the thickness deviation of the phase grating and increased absorption of the analyzer grating. At higher energies, the absorption of the analyzer grating has dominating effect and the visibility decreases as we would expect while at energies below 46 keV, visibility decreases due to the phase grating (not included in the calculations). The difference of 30 % between theoretical values and experimental results comes from the variation of the duty cycle, thickness, and layout design which were not taken into account for the calculations.

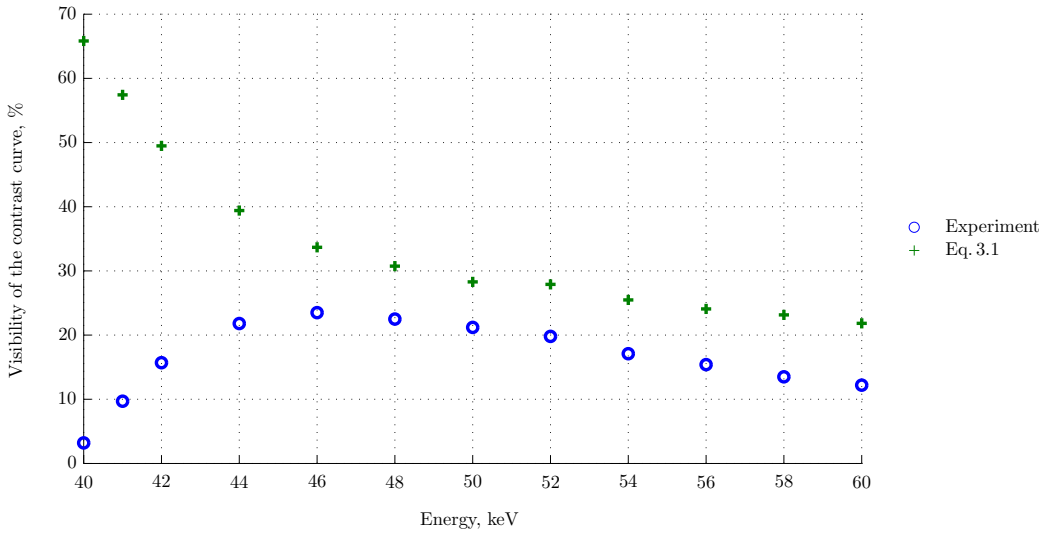

Figure 3.4: Visibility of the contrast curve of the grating interferometer as a function of x-ray energy. The upper curve shows the theoretically expected visibility based on the thickness and layout of the absorption grating. The bottom curve is the experimentally obtained data.

The visibility of the contrast curve is the main efficiency parameter of the gratings chosen for the experiment and performance of the grating interferometer setup. It

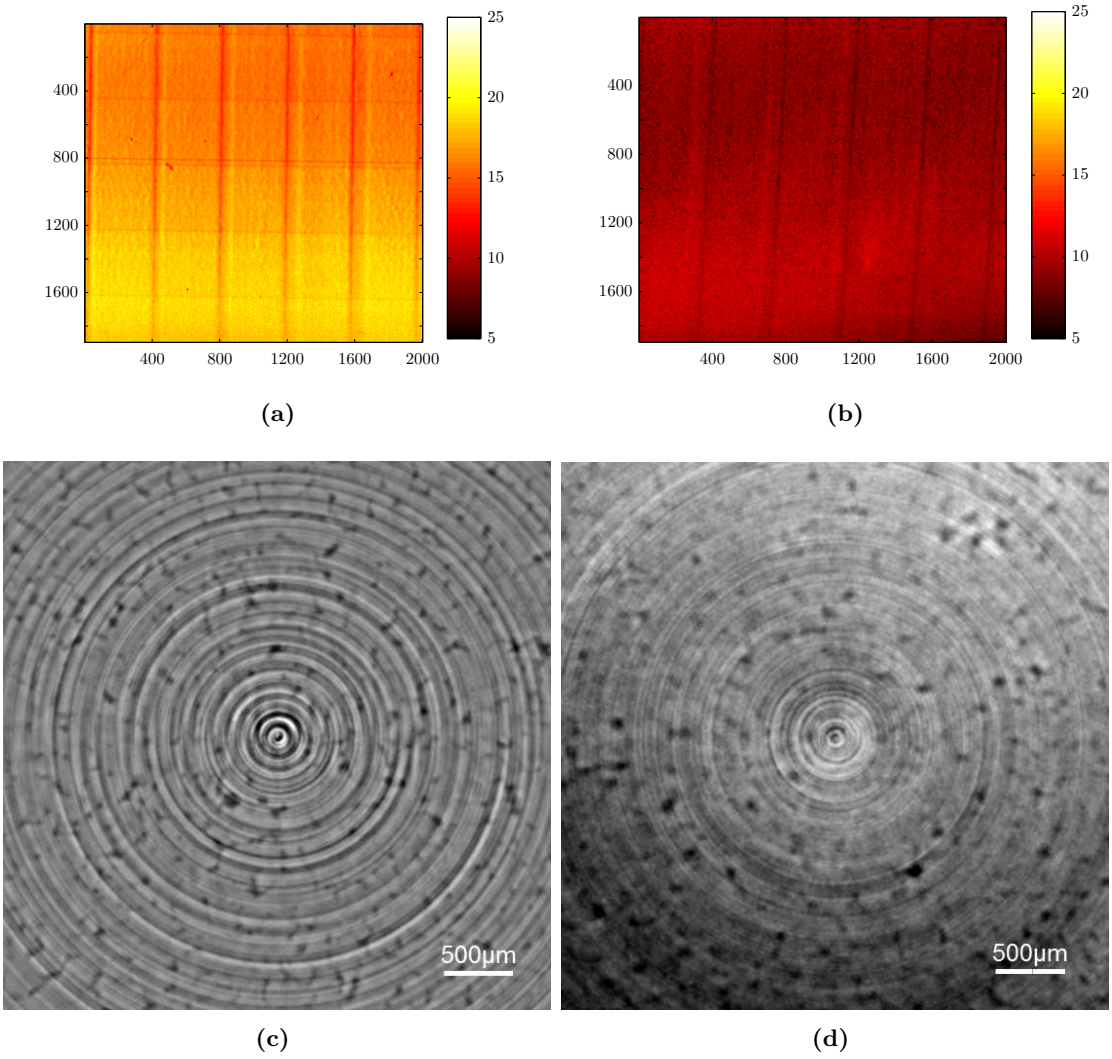

Figure 3.5: The visibility map (colorbar is visibility in %, image axes are in μm) and slice through the reconstructed 3-D volume for two different absorption gratings (a),(c) and (b),(d). In (a), the mean visibility is 16.96±0.16 %, in (b) the mean visibility is 9.45±0.09 %.

determines the signal to noise ratio of the obtained object contrasts. Any defects on the gratings will result in noise in the reconstructed images and artifacts in the reconstructed 3-D volume. As an example, let us consider defects on the absorption grating, e.g. grating lamellas with inhomogeneous thickness. The effect can be seen on the visibility map. We compare two absorption gratings used in the same grating interferometer setup where one grating demonstrates a good and homogeneous visibility map (9.45±0.09 %) and another one though with better visibility value (average over

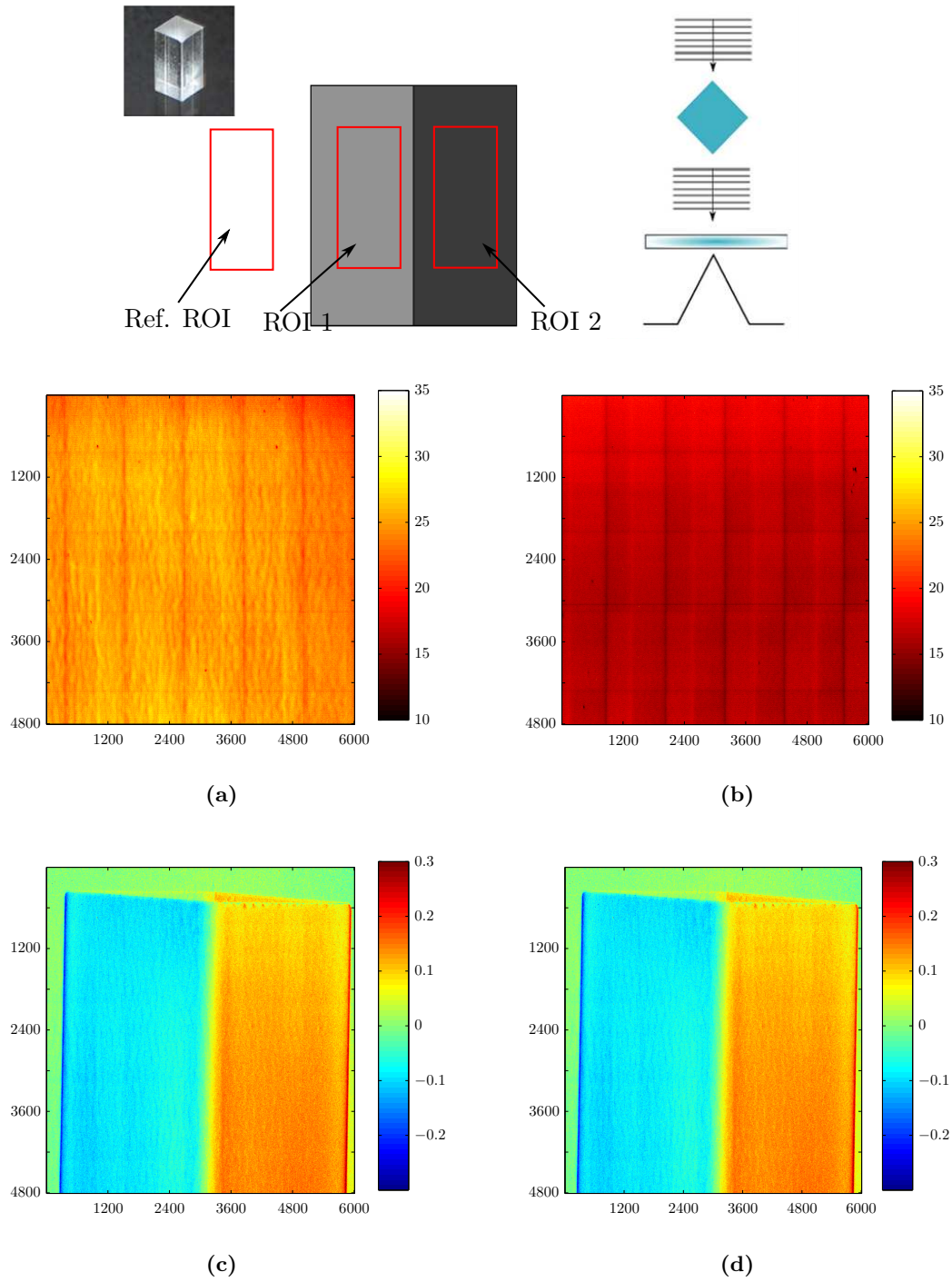

Figure 3.6: (a) The schematics of the quantitative analysis for characterization of gold gratings. (b)(c) examples of visibility maps (colorbar is in %). (d),(e) corresponding phase gradient images of the phantom sample (colorbar is in μrad). Images axes are in μm.

field of view, 16.96±0.16 %) has a higher standard deviation and inhomogeneous field of view as seen in Fig. 3.5. A porous polymer plate (UHMWPE-based scaffold) was visualized with both of the absorption gratings. Slices of the transverse plane through the reconstructed 3-D volume in phase contrast are shown on Fig. 3.5. The polymer material is homogeneous with pores within the volume. The rings are not part of the sample. Strong and abrupt changes in its thickness due to the inhomogeneties in the absorption grating result in clearly visible on the reconstructed slice ring artifacts. The more homogeneous absorption grating leads to a reconstructed volume without visible (strong) artifacts, making a further quantitative analysis of the volume possible.

As the choice of gratings is crucial for the imaging in grating interferometry, the protocol for optimizing set of gratings for imaging is summarized in Fig. 3.6. In order to obtain quantitative characterization of gratings, the phantom sample with simple geometric form (plastic cuboid) was fabricated (see Fig. 3.6). Tilted by 45° such cuboid produces very defined phase shift of a rectangular profile (differential of the triangular). The phantom sample is scanned with the chosen set of the phase and the absorption grating. On the reconstructed differential phase map, and the visibility image of the contrast curve, three regions of interest (ROI) are selected. Two regions with positive and negative phase shift on the differential phase map are selected on the sample. The reference ROI is selected on the background (no sample). For each of these regions we calculate signal to noise ratio, providing an estimate of the noise level. Subsequently contrast to noise ratio (CNR) is calculated for ROI 1 and ROI 2 as $CNR = S_1 - S_2/\sqrt{\sigma_1^2 + \sigma_2^2}$. Contrast to noise ratio gives quantitative evaluation of the phase contrast quality achievable with the grating interferometer setup.The Rose criterion states that a signal to noise ratio of at least 5 is necessary to distinguish features (15). The visibility of the contrast curve and differential phase contrast images are shown in Fig. 3.6 (a-d). One of the absorption gratings demonstrates higher visibility of the contrast curve of ca. 23 % (Fig. 3.6 (a)). However, low signal to noise ratio of 1.58 and CNR of 0.74 does not allow for high quality imaging. At the same time, another grating (Fig. 3.6 (b)) with the lower visibility of the contrast curve of 19 % provides sufficient signal to noise ratio of 11.05 and contrast to noise ratio of 6.68.

Such grating characterization procedure was established for the TopoTomo beamline and performed with every new type of gratings available. Visibility of the contrast curve, signal to noise ratio and contrast to noise ratio are stored for each experiment.

According to these parameters, all grating sets are ranked allowing to choose the best from image quality gratings for the next experiment.

3.2.3 Tilted grating design

In Chapter 2, the principles of the Talbot grating interferometer and the effect of partial coherence on its performance was discussed, for a parallel x-ray beam. However, the x-ray beam is divergent at synchrotron facilities. While for understanding of the grating principles the x-ray beam divergence can be neglected, in practice it is almost not possible to meet the condition where the period of the interference pattern behind the phase grating matches the period of the absorption grating:

$$p_2 = \left(\frac{l + d_T}{l}\right) p_1, \tag{3.2}$$

where l is the distance between the source and the phase grating and d_T is the fractional Talbot distance. The magnification factor $M = \frac{l+d_T}{l}$ is close to 1 for the most synchrotron sources. Even though the magnification factor is small, it is significant in terms of the grating period. For example, behind the phase grating ($\pi/2$) of period 2.4 μm the self image will be increased to a periodicity of 2.41 μm leading to a Moiré pattern with a periodicity of $p_1^2/2(p_2 - p_1)$=288 μm producing about 4 Moiré fringes in field of view of the image. As for high quality imaging only one Moiré fringe is required, the Talbot distance, experimental conditions, and magnification has to be taken into account in order to fabricate one set of gratings. Thus, for each energy, Talbot order, and x-ray source different pairs of gratings has to be designed. Up to now fabrication of such pair of gratings was not efficient in terms of time and costs.

Here, we describe a new concept for fabrication of gratings with slightly smaller period then the period of the mask. By inclining the grating by the angle α, the effective grating period felt by x-rays can be reduced to $\tilde{p} = p \cos \alpha$ (see Fig. 3.7 (a) and (c)). However, at the same time the transmission function of the grating will not have anymore square shape, shifting the incoming wavefront not only by $\pi/2$. This results to the Ewald sphere not crossing most of the diffraction orders, as shown in Fig. 3.7 (e). Note that due to the limited field of view and high sampling, high frequency numerical artifacts might be present in the calculated reciprocal space maps.

To gain the same effect, the mask can be tilted during fabrication (Fig. 3.1) of the grating by the same angle α, producing a tilted grating as illustrated in Fig. 3.7 (b).

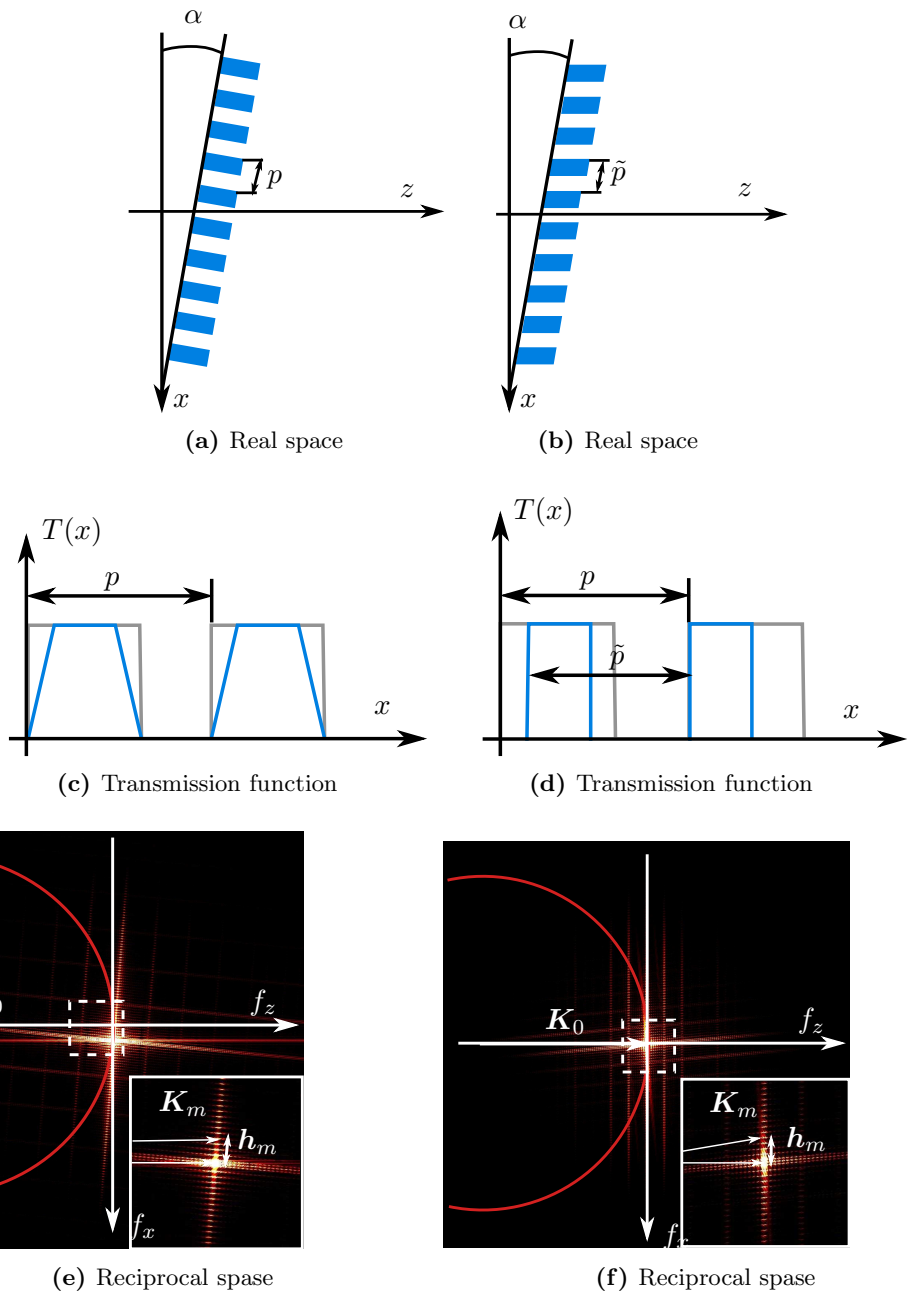

(a) Real space **(b)** Real space

(c) Transmission function **(d)** Transmission function

(e) Reciprocal spase **(f)** Reciprocal spase

Figure 3.7: (a) Schematics of the grating in the real space tilted by the angle α. (b) Schematics of the tilted grating in the real space tilted by the angle α. (c) and (d) are the transmission functions for the case of normal and tilted grating respectively. (e) and (f) are the calculated reciprocal space maps for the normal grating and tilted grating.

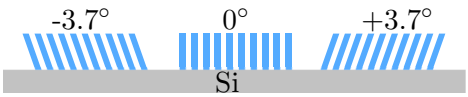

Figure 3.8: Schematics of the fabricated phase grating profile.

The transmission function of such a grating has the required square profile with the period being smaller than the original mask (Fig. 3.7 (d)). If we position the tilted grating under the same angle α in the beam, the leading diffraction order will be inline with the optical axis and the transmission function will have a square profile but with the smaller period $\tilde{p}$ (Fig. 3.7 (f)). Thus, different grating periods can be fabricated without the need of a new mask (most expensive step of the fabrication process).

The concept of a tilted grating was verified at the TopoTomo beamline at the ANKA light source. A phase grating was fabricated with three active areas: -3.7, 0, and +3.7 degrees tilt as sketched in Fig. 3.8. The chosen angle corresponds to an x-ray energy of 25 keV, the 1^{st} Talbot order, and an absorption grating of 2.4 μm period. A set of phase-stepping images was acquired for these three areas of the grating positioned within the interferometer into the x-ray beam. The visibility values of the contrast curve and number of Moiré fringes are shown in Fig. 3.9 (a) as a function of angle. According to the obtained data, the visibility values are the same for the tilted gratings as for the conventional grating at $\alpha = 0$ when they are positioned at the right inclination angle. The visibility curves are periodic along the tilt angle axis. The main peaks correspond to the aligned gratings when the main diffraction order propagates along the optical axis.

At the same time the number of Moiré fringes decreases for each grating area when the angle alpha is close to ± 3.7 degrees as seen in Fig. 3.9 (b). As number of Moiré fringes was calculated by fitting cos wave function on each image, it can be non-integer number and have inaccuracy for the number of fringes less than two. The conventional grating positioned at the angle ± 3.7 degrees exhibits no Moiré fringes, the visibility value is 4 times smaller and thus it is not efficient for imaging. Meanwhile, the achieved visibility and number of Moiré fringes for tilted grating makes imaging possible and these gratings are thus an essential improvement for the grating interferometer. The grating interferometry setups and results discussed throughout this work are based on the measurements with the tilt grating design.

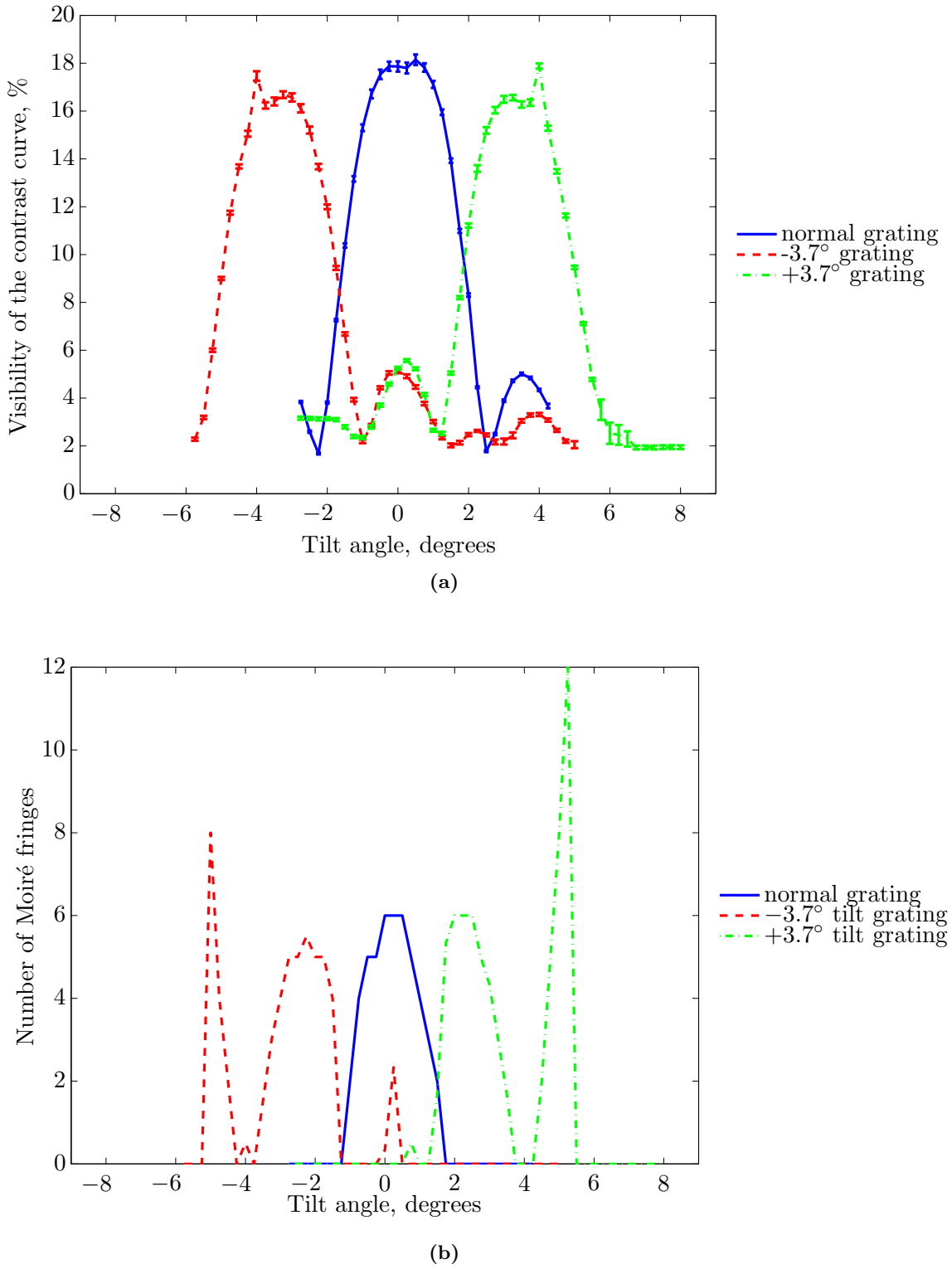

Figure 3.9: (a) Visibility values for the three regions of the phase gratings versus positioning angle in the beam. (b) Corresponding number of Moiré fringes with respect to positioning angle in the beam.

At last, we would like to mention that the development of the x-ray gratings and their combinations in grating interferometers remains an active area of research. Some of the recent developments include: fabrication of x-ray gratings for 82 keV (91), application of gratings with different duty cycle (16), and different shape profile (94).

4 High-speed phase contrast imaging

Contents

To this date, grating interferometry has been used with highly coherent x-ray synchrotron sources only. A high degree of coherence guaranteed great imaging quality, however at the cost of photon flux, thus increasing time for acquisition.

In this chapter, it is demonstrated how high-speed imaging with grating interferometry can be achieved. The optimization of the x-ray energy bandwidth is discussed, keeping balance between visibility of the grating interferometer and acquisition time. This chapter starts with an outline of the properties of the TopoTomo beamline where the implementation of high-speed grating interferometer took place. Subsequently, the design of the system is discussed in detail, focusing on the optimization of the available degree of coherence. The high-speed acquisition scheme developed within this thesis is demonstrated by imaging the egg of the insect *Peruphasma schultei*. In the end of the chapter, the high-speed grating interferometer to investigate is used to investigate the porosity in polymer-based scaffolds.

4.1 The TopoTomo beamline

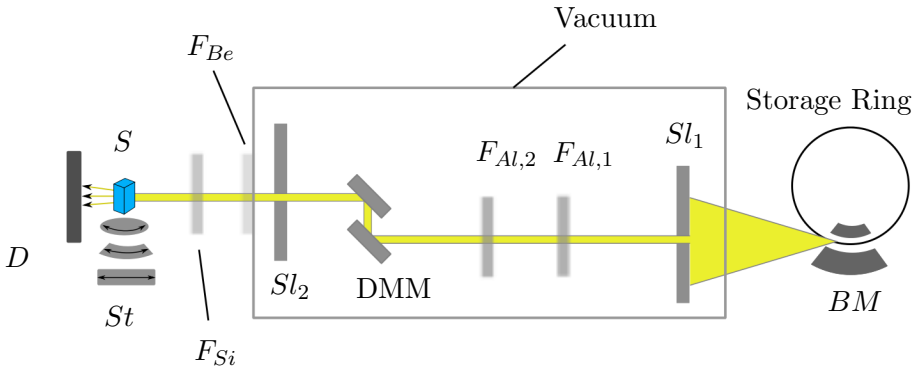

Figure 4.1: Schematics layout of the TopoTomo beamline.

The implementation of high-speed grating interferometry was done at the synchrotron radiation source ANKA. Producing a wide range of radiation from infrared to hard x-rays, ANKA operates more than 13 beamlines focusing on different characterization techniques and application fields. The TopoTomo beamline started operation in 2008 for white beam topography and tomography experiments. It provides a white beam from a bending magnet (BM, critical energy 6.1 keV) and pink beam (bandwidth of 10^{-2}) with the use of a double multilayer monochromator (DMM, available since 2010). The beamline optics include two sets of slits (horizontal and vertical), DMM, a number of filters, and as the last component at the beamline a berillium window (see Fig. 4.1). At the end of the station, which is 30 m downstream of the source, a tomographic manipulator with an x-ray detector is installed. The parameters of the TopoTomo beamline are listed in the Table 4.1.

In order to realize 3-D scanning of the sample in tomography or laminography, an accurate positioning of the rotation axis with respect to the x-ray beam is performed by the sample manipulator. The sample manipulator utilizies 4 degrees of freedom (3 of them are shown in Fig. 4.1). Translation in the (x, y) plane is required for positioning the sample in and out of the x-ray beam. Rotation around the y axis is required for acquiring projections for different angles over 360 degrees. Additional horizontal rotation around the x axis is utilized to adjust the laminographic angle Θ. The sample manipulator is flexible, allowing to perform radiography through an aperture in the

Parameters	Values and descriptions
Energy range	6 keV-40 keV
Energy resolution [ΔE/E]	white light (optional 2% bandwidth)
Source	1.5 T Bending magnet (E_c=6.1 keV)
Divergence	2 mrad x 0.5 mrad (H x V)
Source size	800 μm x 200 μm (FWHM, H x V)
Distance source-sample	30 m
Flux at sample position	1x10^{16} ph/s (10 mm x 10 mm), white beam
Filter stage, F_1	Al 1 mm; Al 0.2 mm; Be 0.6 mm,
Filter stage, F_2	Cu 0.05 mm; Al 0.5 mm; Be 0.2 mm
Optics, F_3	slits, Be window 0.5 mm thick

Table 4.1: TopoTomo beamline characteristics.

sample rotary stage without dismounting the specimen (17). The object positioned on the sample manipulator is limited in size to 6 mm x 80 mm, which is the maximum beam size at the TopoTomo beamline.

The x-ray detector system is located downstream of the sample manipulator and was designed and developed at ANKA (27). The x-ray detector system includes a CCD camera pco.4000 coupled with visible light optics and a scintillator (typically LuAG of 200 μm thickness). The total magnification of this detector system can be varied from 1 x to 25 x, which allows to chose the spatial resolution and field of view dependent on the specific application.

4.2 The grating interferometer setup

The grating interferometer has been implemented in the existing tomography (laminography) setup and is positioned between the sample manipulator and the detector system. For for phase contrast imaging with the high-speed grating interferometer, the following degrees of freedom are necessary. The phase grating with tilted structures requires a rotation axis (around the y axis) to position the grating at the corresponding angle α such that the optimal number of Moirŕ fringes and the visibility of the contrast curve can be adjusted (see Fig.3.7). The parallelism between the gratings is reached when a single Moiré fringe covers the whole detector's field of view. Addition-

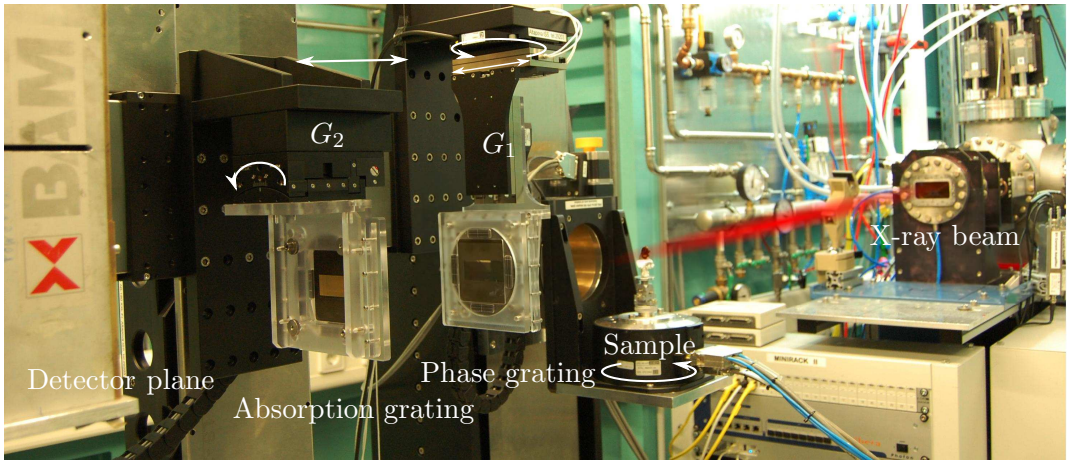

Figure 4.2: Photograph of the built up grating interferometer setup implemented at the TopoTomo beamline.

ally, it needs to be equipped with a translation degree of freedom, along the x axis for phase-stepping curves. The precision of the stepping is crucial for correct retrieval of the phase,and is realized via a piezo actuator with a minimum step size of 6 nm. The absorption grating needs to be positioned at the fractional Talbot distances, depending on the x-ray energy and the period of the gratings chosen for the experiment. Thus, it is mounted on the motorized stage along z. A photograph of the implemented grating interferometer is shown on Fig. 4.2. Similar to the sample manipulator, the system is equipped with translation in the (x, y) plane to position the grating interferometer in the beam for phase contrast imaging or out of the beam for conventional absorption imaging.

For grating interferometry experiments, the phase-stepping technique with a minimum of 4 steps over 1 grating period is performed for each tomographic or laminographic rotation angle. A series of projection phase-stepping curves over 360 degrees are then detected by the detector system. For imaging with grating interferometry, the pixel size of the detector has to be not smaller than the period of the absorption grating due to the Nyquist-Shannon sampling theorem (75). With the available magnification an effective pixel size of 2.5 μm was chosen, resulting in a field of view of $10 \times 6.7\,\mathrm{mm}^2$.

In summary, the procedure for grating interferometry imaging at the TopoTomo beamline is summarized in Fig. 4.3.

The alignment and installation procedure of the grating interferometer is typically

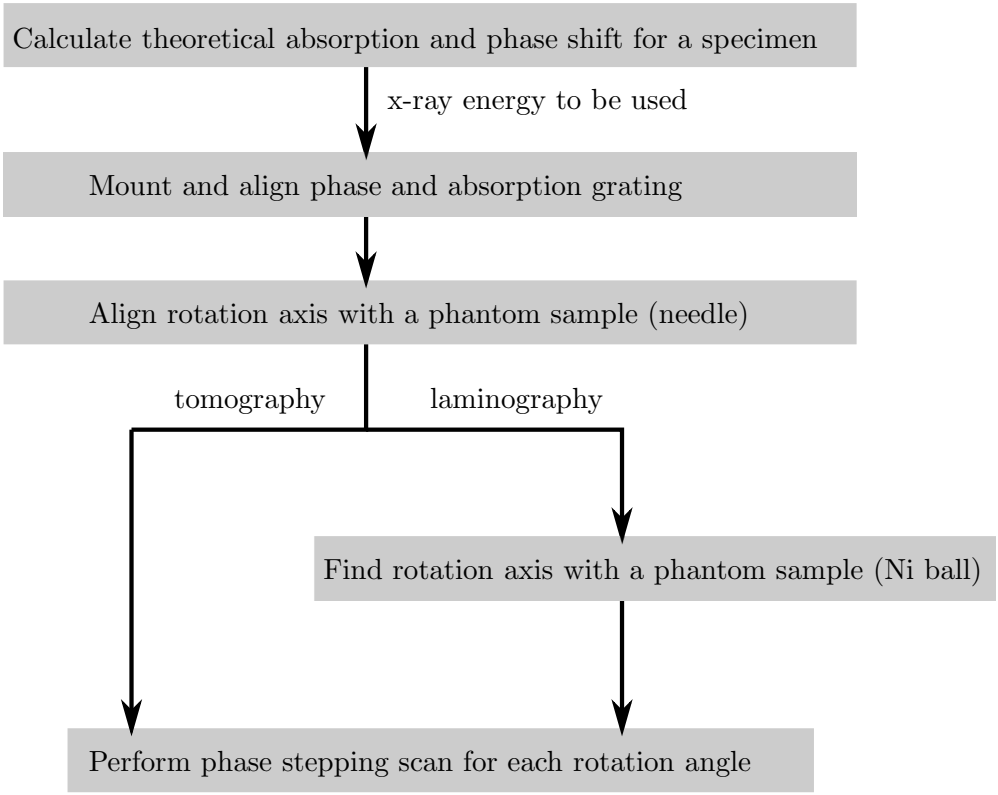

Figure 4.3: The flow chart of imaging with grating interferometry at the TopoTomo beamline.

realized within 4 hours. Then if the samples are of similar properties 3-D acquisition is performed for each object with total time of a few hours to a few seconds depending on the acquisition schemes, which will be later discussed in section 4.4.

For analysis of the data obtained in the experiments we wrote set of scripts in Matlab unified in one library for grating interferometry, which allows to perform corrections of the obtained data, normalization and reconstruction of absorption, phase and dark-field contrasts for each rotation angle. The 3-D volume in each contrast function is reconstructed by reconstruction library developed by KIT and the Saint Petersburg State University of Civil Aviation (64).

4.3 Optimisation of the exposure time

For high-speed experiments, shortening of the exposure time requires high photon flux densities. Thus, for high-speed grating interferometry the monochromator available at the TopoTomo beamline was not used and moved out of the x-ray beam path. In this case, the coherence volume of the beamline has to be optimized in order to guarantee satisfactory data quality for grating interferometry.

The peak maximum of bending magnet spectrum of the TopoTomo beamline is at 6.1 keV (see Fig. 4.4). In order to check whether grating interferometry is possible with such a broad energy spectrum, the propagation of such a beam behind a $\pi/2$-shift phase grating was simulated using the coherence properties of the beamline (grating imperfections and detector efficiency are not included). Figure 4.4 (b) shows the Talbot carpet for the bending magnet spectrum behind a phase grating over three Talbot distances. We observe that the self-imaging effect does not take place, making imaging with grating interferometry impossible.

To achieve a self-imaging effect, an optimization of the temporal coherence is required, which can be achieved by employing beamline filters existing at the TopoTomo. Utilizing an 1.5 mm thick Al filter (the most attenuating material), we obtain a Talbot carpet in which the self-imaging effect is visible for the first Talbot order (see Fig.4.4 (c)). However it's contrast is rather low and the position along the z axis does not correspond to the theoretical first Talbot order. In order to increase the interference contrast, a set of silicon wafers with a total thickness of 6 mm was used additionally. The Si wafers were highly polished to avoid degradation of the transverse coherence due to surface scattering effects. The resulting spectrum is a distribution with an energy resolution of $\Delta E/E \sim 1$ centered at an energy of 25 keV. The obtained Talbot carpet (Fig. 4.4 (d)) exhibits the self-imaging effect at the correct Talbot distance, allowing for imaging with the grating interferometer.

The visibility of the interference pattern along the z axis is shown in Figure 4.4 (e). The shift along the optical axis and the increase in contrast is clearly observed after optimization of the spatial coherence. At the first Talbot order and with use of filters at the beamline, 60 % of visibility can be reached. The spatial coherence length required for grating interferometry was adjusted by a slit aperture of $500 \times 500\ \mu\text{m}^2$ placed 24 m

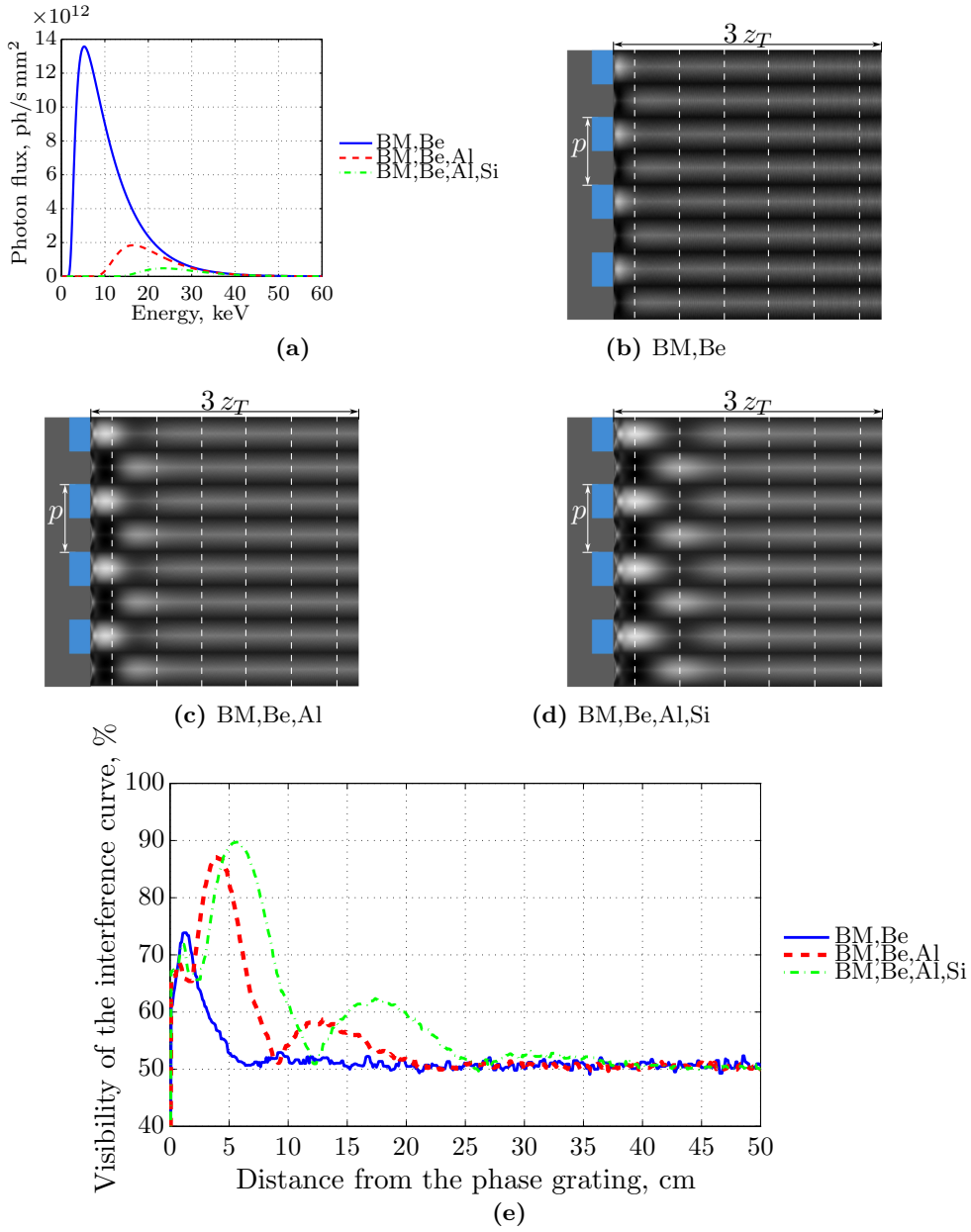

Figure 4.4: (a) Normalized photon flux spectra for 1 - BM with Be window, 2 - BM, Be window and 1.5 mm Al, and 3 - BM, Be window, 1.5 mm Al, and additional Si filters. Talbot carpets behind the grating are shown in (b) for BM with Be window, (c) BM, Be window, and 1.5 mm Al, and (d) BM, Be window, 1.5 mm Al, and additional Si filters. (e) Expected visibility of the interference pattern behind a $\pi/2$ phase shift grating corresponding to the spectra in (a). The white dashed lines mark the theoretical positions of the fractional Talbot orders. The colormap is linear from black being equal to 0 to white being equal to 3.

upstream from the experiment. The resulting spatial coherence length of 2.4 μm was sufficient to perform imaging at the first Talbot order (see Eq. 2.47 and Figure 2.14).

Though the use of the 1^{st} Talbot order limits phase sensitivity of grating interferometry (see Eq. 2.29), for most applications it is sufficient for imaging. The optimized x-ray spectrum allows for approximately 10 times shorter exposure times as compared to the monochromatic beam (utilizing DMM).

4.4 High-speed acquisition scheme

Apart from the optimization of the exposure time for each image, it is also important to optimize the acquisition scheme based on the available mechanics. The phase grating stepping is controlled via a piezo-electric signal that is very fast. However, the rotation is performed with a stepping motor. This would imply the following procedure: rotation to a certain angle, stop, correction of the position, stopping the motor, acquiring an image, going to the next position. All these steps can be avoided by using a continuous rotation of the sample and performing the phase-stepping between the tomograms.

In such an experiment the phase grating will be shifted (stepped) only once every 360 degrees, resulting in four tomograms as illustrated in Fig. 4.5. The speed of rotation and frame rate of the camera are adjusted in such a way that the required optimal number of projections are obtained. The optimal number of projections is determined by the number of pixels M in the row of the detector used to reconstruct a slice, that is $\frac{\pi}{2}M$ (41). At the same time, the number of images acquired in the high-speed acquisition scheme is determined by the speed of rotation v_{rot} and the frame rate of the camera v_{cam} as $2\pi v_{cam}/v_{rot}$. Thus, both should be adjusted such that $v_{cam}/v_{rot} = M/4$. With the typical sensor size of 2000 pixels, the frame rate of the camera has to be 500 times higher than rotation of the sample. This condition is easily met with currently available cameras (frame rate of 60000 frames per second) (55) and rotation stages (20 rounds per second) (2). This high-speed acquisition scheme additionally allows to speed up imaging with grating interferometry by a factor of approximately 900, giving a total improvement of about 4 orders of magnitude.

The continuous rotation in particular the acceleration phase at the beginning, does not allow to start and stop the data acquisition exactly before and after 4 tomograms (if 4 phase-stepping steps are used). Thus, in the second step a start and end point of

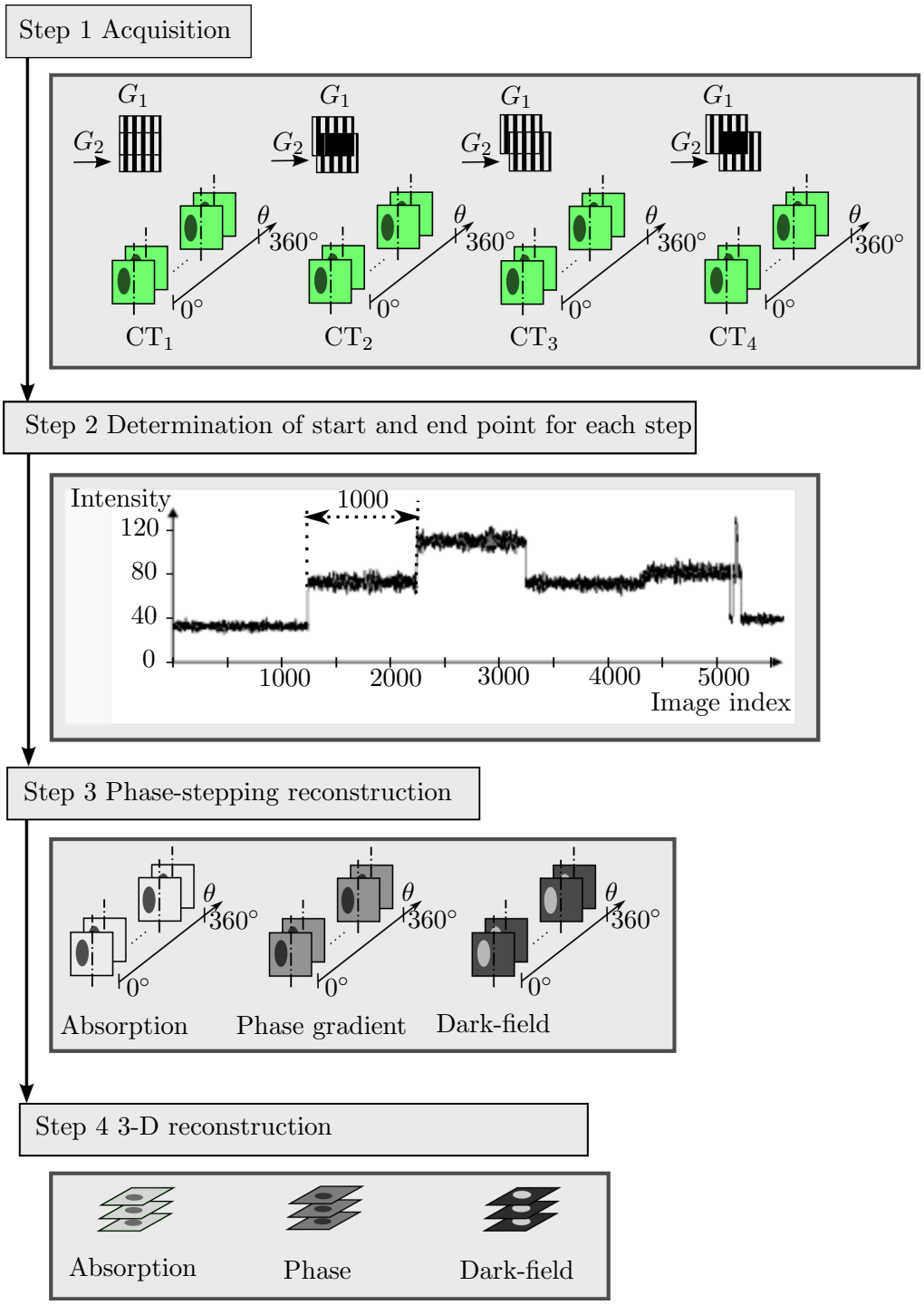

Figure 4.5: Flow chart of the high-speed acquisition scheme with a grating interferometer at ANKA.

the individual tomograms need to be determined independently. For this, the average intensity over a region of interest where the sample is not located is computed and potted as a function of image number as shown in Fig. 4.5. Every rapid change of the intensity correspond to the changed phase grating position. By calculating the time derivative of such a profile, start point, end point, and number of projections taken over full sample rotation are obtained. In the finale two steps, phase-stepping and tomographic reconstructions are performed as described in Chapter 2.5.

4.5 Proof of principle experiments

For high-speed grating interferometry, spatial resolution, phase sensitivity, 3-D volume reconstructions, and application to the real application case has to be confirmed.

4.5.1 Spatial resolution

The quality of any imaging setup is first of all determined by its spatial resolution defined by the smallest feature to be distinguished. In grating interferometry, the spatial resolution is limited by the pitch of the analyzer grating (sampling rate), the detector pixel size (blurring the image) and the reconstruction technique. On the other hand, a high resolution of the imaging system will not help if the contrast in the image is too low. Grating interferometry provides three independent contrast signals and is thus more likely to give a suitable contrast for two given (similar) materials than pure absorption contrast. However, the sensitivity of phase and dark-field contrasts is governed by the pitch of the analyzer grating, the Talbot order and the visibility of the contrast curve (Eq. 2.29).

In order to check the imaging quality of the grating interferometry at high-speed, a resolution test pattern (similar to the Siemens test patterns) was designed and fabricated by electron beam writing within the Karlsruhe Nano and Micro Facility (KNMF). The obtained 2-D absorption, phase, and dark-filed contrast images are shown on Fig. 4.6. The resolution is best in the case of pore absorption but the line profiles through the test pattern (Fig. 4.6(d)) indicate that the contrast of large features in the phase image (integrated differential phase) is up to 4 times higher than in absorption.

The spatial resolution in 2-D does not guarantee the same resolution in 3-D imaging. Thus the resolution in 3-D was investigated by imaging the test pattern with grating

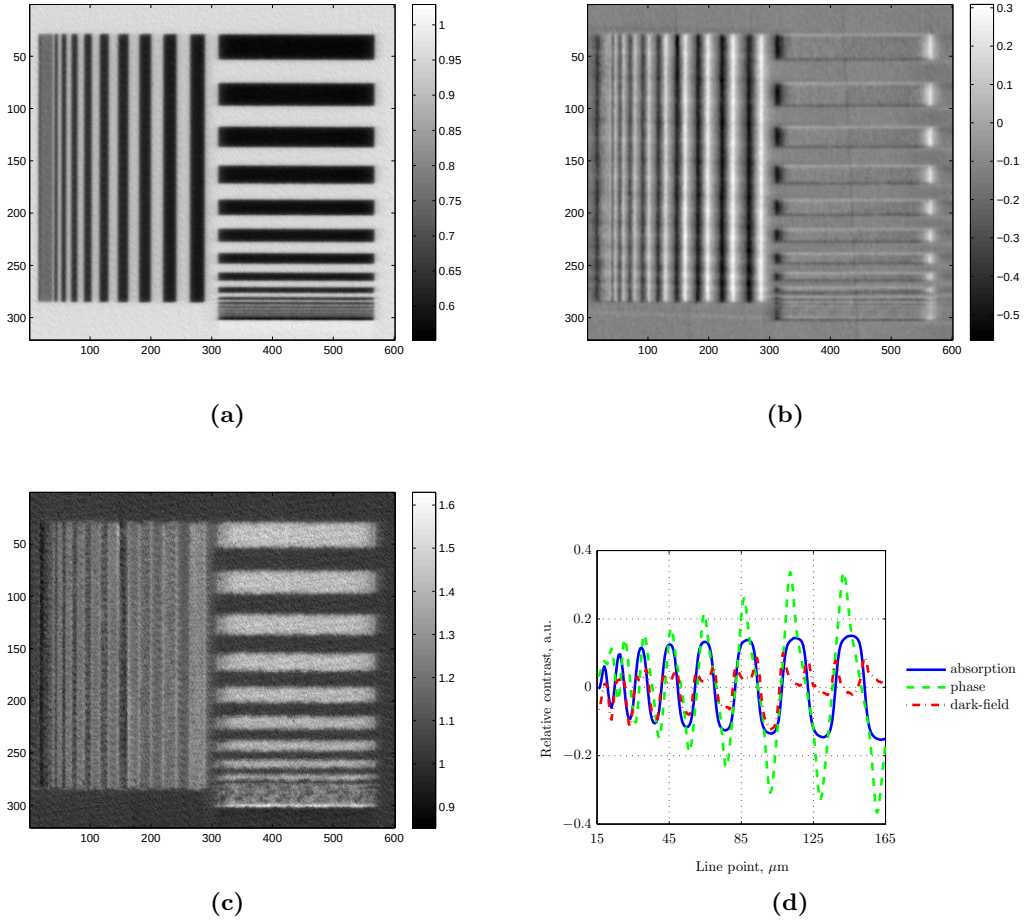

Figure 4.6: The resolution test pattern (largest feature of 15 μm and smallest feature of 1 μm size). (a), (b) and (c) are absorption, differential phase and dark-field contrasts. Line profile through the vertical lines of all three images in (d). Field of view for images (a-c) is 360 x 360 μm.

interferometry in laminographic geometry. Reconstructed 3-D volumes in absorption, phase, and dark-field contrast are demonstrated in Fig. 4.7 (a-c). The resolution was quantitatively analyzed in all three contrast modes, by calculating the modulation transfer function $((I_{max} - I_{min})/(I_{max} + I_{min})$, where I_{max} and I_{min} are the maximal and minimal pixel value, respectively) for each feature size (frequency) as shown in Fig. 4.7 (d). Results show that the resolution of grating interferometry in 3-D volume is limited to 10 μm distinguishable feature.

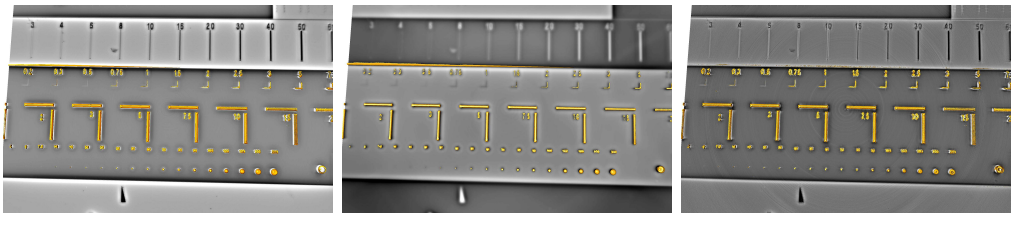

(a) absorption **(b)** phase **(c)** dark-field

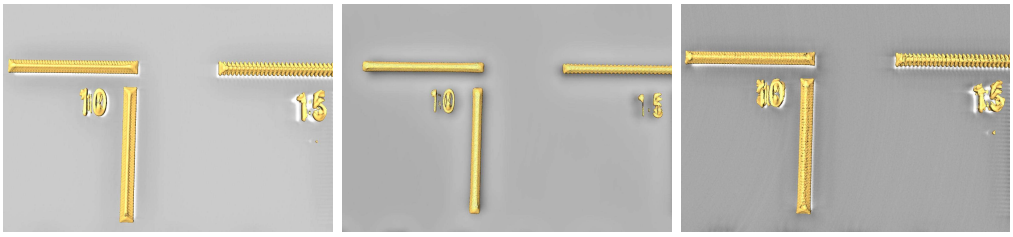

(d) absorption ROI **(e)** phase ROI **(f)** dark-field ROI

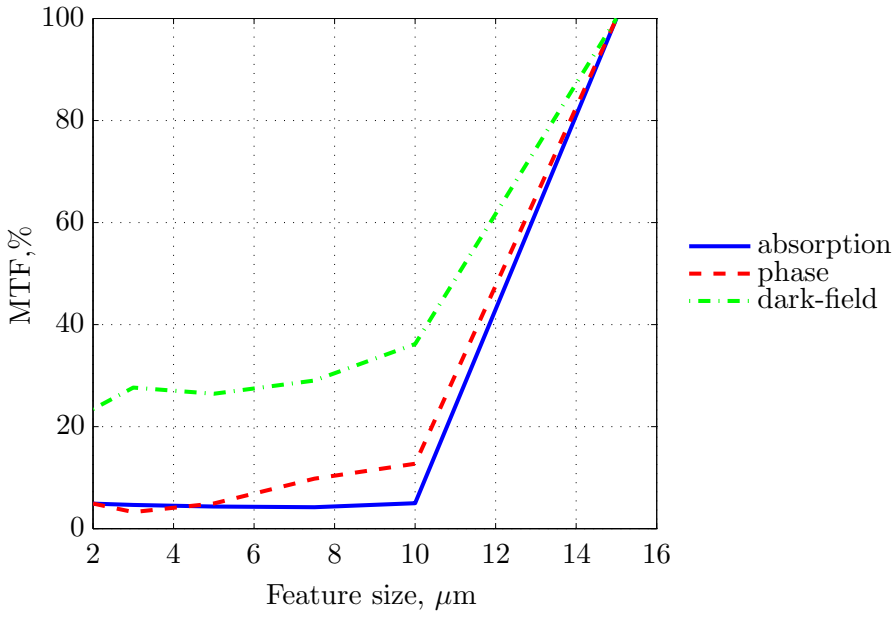

(g) MTF

Figure 4.7: (a)(b),(c)Absorption, phase and dark-field renderings of the resolution test pattern. (d) Calculated from the 3-D volume MTF for feature sizes of 2,3,5,7.5,10 and 15μm.

4.5.2 Phase contrast imaging

High-speed phase contrast imaging with a filtered white beam was demonstrated by imaging a two-dimensional teflon mesh. An example of reconstructed images is illustrated in Fig. 4.8. All images were extracted from the same dataset with a total exposure time of 2 s. For the images, the conventional transmission image shows the shape of the mesh with the main structures. The differential phase image enhances the contrast at the interfaces of the fibers. Because the phase-stepping was performed along x direction, only vertical fibers of the mesh are visible. The dark-field image is generated by small-angle scattering from the sample. Note that here small-angle scattering is defined as the signal that corresponds to the refraction angle larger than the maximum measured phase-contrast image angle p_2/z_n (69). The dark-field signal is most prominent at the knots of the mesh, visible as white horizontal lines, and produced by the scattering at the borders of the fibers with air.

4.5.3 High-speed imaging with grating interferometry

A feasibility experiment of high-speed acquisition scheme of grating interferometry was performed on an egg of the stick insect specimen *Peruphasma schultei*. The experiment was done with the filtered white beam, continuous rotation stage (maximum speed 1200 rpm) and an Photron camera with a maximum of 10000 fps and a pixel size of 6 μm x6 μm. The egg of *Peruphasma schultei* with 1000 fps, 4 steps over 1 grating period, and 1000 projections, resulting in only 4 seconds total acquisition time per tomogram. Slices through the reconstructed volume in absorption and phase contrast are shown on Fig. 4.9.

From the x-ray tomogram we can see that the egg shell has fine wrinkles and is granulated. It has a cap (bottom part of the shell) and a length of about 4 mm. The egg yolk is partially attached to the walls of the shell. The air cavities within the yolk, the yolk and the shell morphology is clearly visible in both contrasts.

The renderings of the egg in 3-D are shown on Fig. 4.9 (c) and (d) in absorption and phase contrast. The granulated structure of the egg and the yolk that only occupies 10% of the volume are clearly resolved. High-speed grating interferometry in this particular example will be further used for the *in vivo* study of embryogenesis in insects and other model organisms.

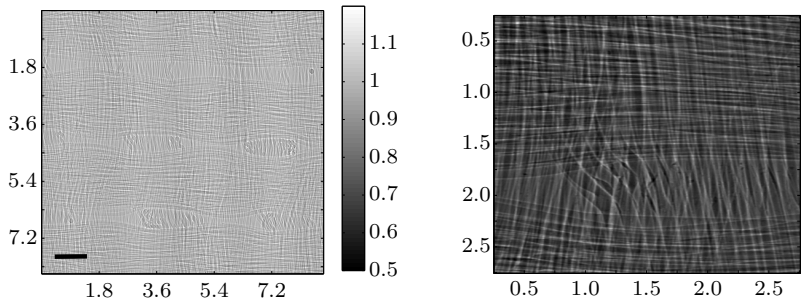

(a) absorption

(b) absorption ROI

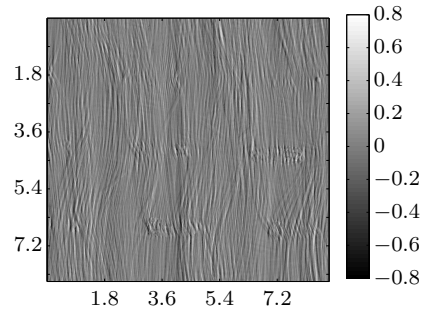

(c) differential phase

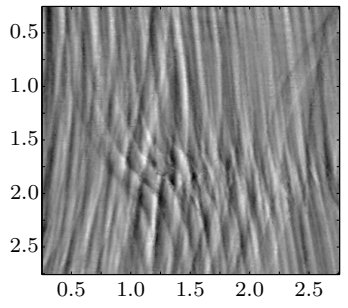

(d) differential phase ROI

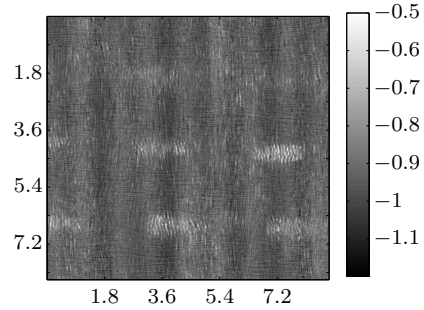

(e) dark-field

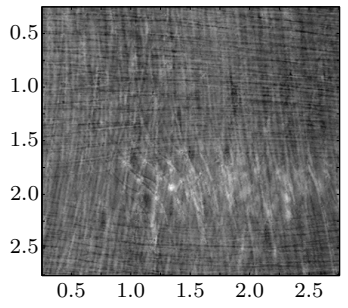

(f) dark-field ROI

Figure 4.8: Absorption (a), differential phase (c), and dark-field contrast (e) and corresponding regions of interests in (b),(d), and (f) of a Teflon 2-D mesh. The image axes are in mm.

In this way, even 3-D real-time phase-contrast imaging could be conceivable, opening application in new fields, especially for imaging of dynamical processes.

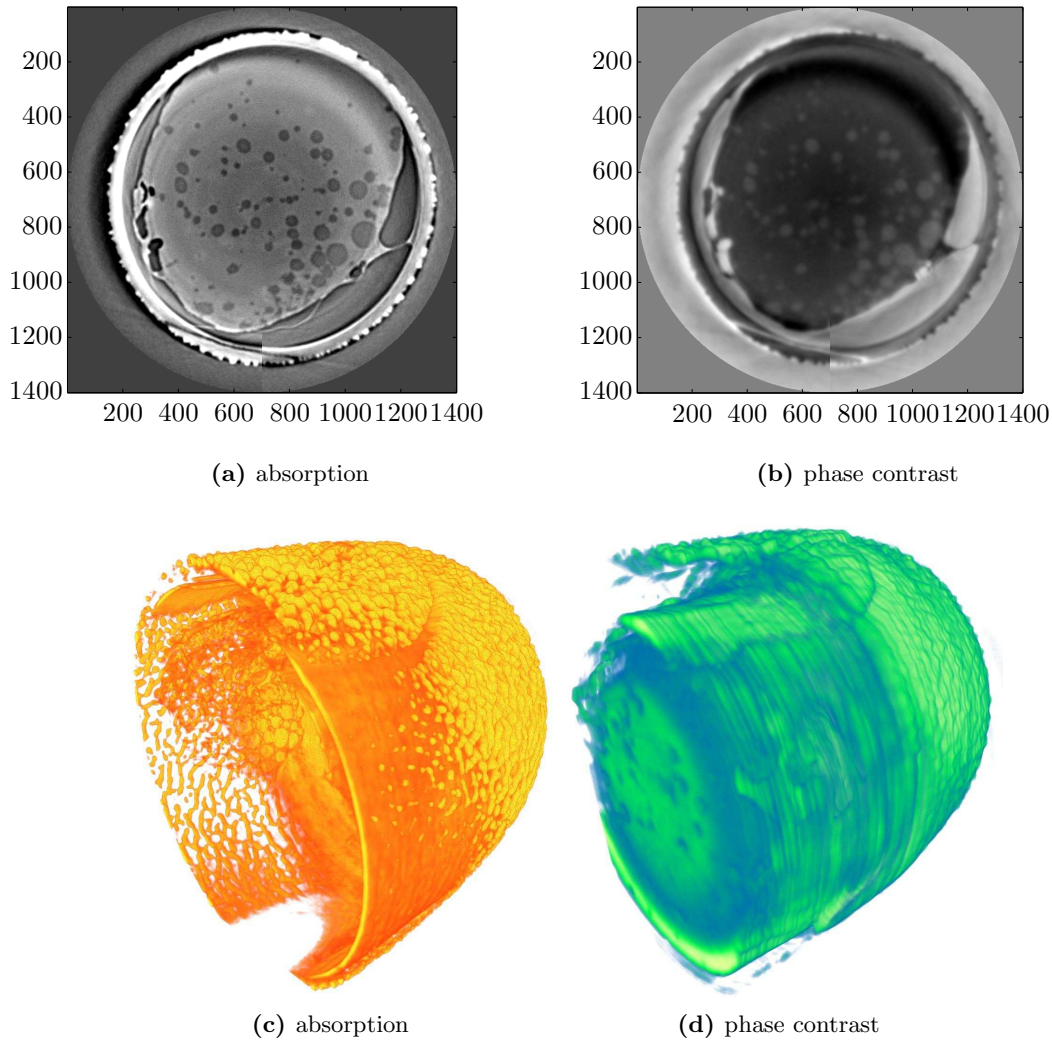

(a) absorption **(b)** phase contrast

(c) absorption **(d)** phase contrast

Figure 4.9: Slices through the reconstructed volume of the *Peruphasma Schultei* egg in (a) absorption and (b) phase contrasts. The 3-D volume rendering of the *Peruphasma Schultei* egg from the high-speed grating acquisition scheme in (c) absorption and (d) phase contrast. Image axes are in μm.

4.6 Porosity in polymer-based scaffolds

Biomaterials are natural or synthetic materials which are used to replace or repair damaged tissue or to interface with the biological environment. Today a key component of the approach for tissue regeneration is to produce a natural or artificial material that acts as a template for cells providing structural support and guiding them to the newly formed tissue (36). The main function of the scaffold is to support the growing tissue

♯	UHMWPE	Additive	Density, (g/cm^3)
1	UHMWPE	-	0.930
2	90 % UHMWPE (GUR4022)	10 %PVDF	0.590
3	UHMWPE (GUR4022)	-	0.550
4	80 % UHMWPE	20 %LDPE-g-SMA	0.940
5	80 % UHMWPE	20 %LDPE-modified (ozon)	0.928

Table 4.2: Fabricated UHMWPE-derived scaffolds.

by cell migration and proliferation. To fit these functions it must have an appropriate porosity, adequate surface area, and a defined three-dimensional shape. All of these properties must be tailored to arrange of the requirements of different types of tissue (44).

In this section, we focuses on the characterization of samples made of ultra high molecular weight polyethylene (UHMWPE) and its copolymers possessing porous and dense structures. The work was done in the collaboration with the Tomsk Polytechnic University and the State Siberian Medical University, Russia. Synchrotron radiation x-ray phase contrast imaging using grating interometry is applied to analyze the inner architecture and microstructure of virgin samples.

The scaffolds used in the present work were fabricated out of UHMWPE and its copolymers and their main parameters are summarized in Table 4.2. The UHMWPE samples scaffolds were produced by the compression moulding technique, where the properties of the materials depends on the process temperature, pressure and time (3). UHMWPE powder was pressed at a controlled pressure (15 kN), and a temperature 170 ∘C was applied to the mould using an electrically heated system. Pure UHMWPE is difficult to process due to its high viscosity. Thus UHMWPE was combined with short chain polymers such as LDPE and PVDF. For higher stability, adhesion, and better mechanical properties of the obtained copolymers, styrene maleic anhydride (SMA) was used as a reactive group. It is chemically bound to the polymer components of the mixture to form covalent bonds, significantly reducing the interfacial energy between the different polymers. For fabrication of porous samples, we used UHMWPE GUR4022 (Ticona LLC) powder with an average particle size of 120-150 μm.

The formed polymers and copolymers possess a both porous and dense internal

structure. The materials have the shape of round or rectangular plates with s thickness around 0.8-1 mm, that were cut into square samples of $1 \times 1\, cm^2$ size. All samples were cleaned in an the ultrasonic bath with ethanol and then washed in distilled water with subsequent drying in air.

The rate of cell penetration and growth in the polymeric porous structures is directly related to the pore size and distribution in the material and varies according to the size of the invading cells and the properties of the implant. For this reason, the pore distribution, their interconnectivity and size are of significant interest for biomaterial characterization. Investigation of the 3-D scaffold structure gives further information about the bulk properties of these materials. Images, obtained using x-ray grating interferometry in laminography mode are shown in Figure 4.10.

From the five types of polymer samples, three of them - pure UHMWPE, UHMWPE with GUR4022, and copolymer of UHMWPE with LDPE-g-SMA - are without any pores within the volume. Inclusions and impurities can be seen on a few slices, see for example Fig. 4.10 (c) and (d) for UHMWPE polymer with GUR4022, however in too low a concentration such that the material can not be used for implants. The polymer type 5 which is 80 % UHMWPE and 20 %LDPE-modified (ozon) demonstrates large pores within one slice of the volume from Fig. 4.10 (e) and (f). However, the pore size is of about 1 mm in diameter and too large for a scaffold material.

The structure of the polymer specimen 2 which is copolymer with 90 % UHMWPE (GUR4022) and 10 %PVDF shows round pores with and an average size of around 100 μm. Even though different samples from polymer type number 2 possess different pore distribution, its size range is suitable for biomedical application. The pores are interconnected and look like agglomerations of smaller units.

For quantitative analysis of the pores and their distribution, the ratio of the real part of the refractive index and its decrement was computed, see Fig. 4.10 (a). The use of this combination of two contrasts modes allows to increase the contrast between polymer material and air (or low density polymer) within the volume, making standard threshold segmentation possible, see Fig. 4.11. The binary image obtained from the ratio of absorption and phase contrast was further processed in the image processing software MAVI- Modular Algorithms for Volume Images (42).

Of the complete sample volume of 600 μm^3, the pores make out around 15%. 90% of the pores are interconnected, meaning that there is low number of isolated pore units,

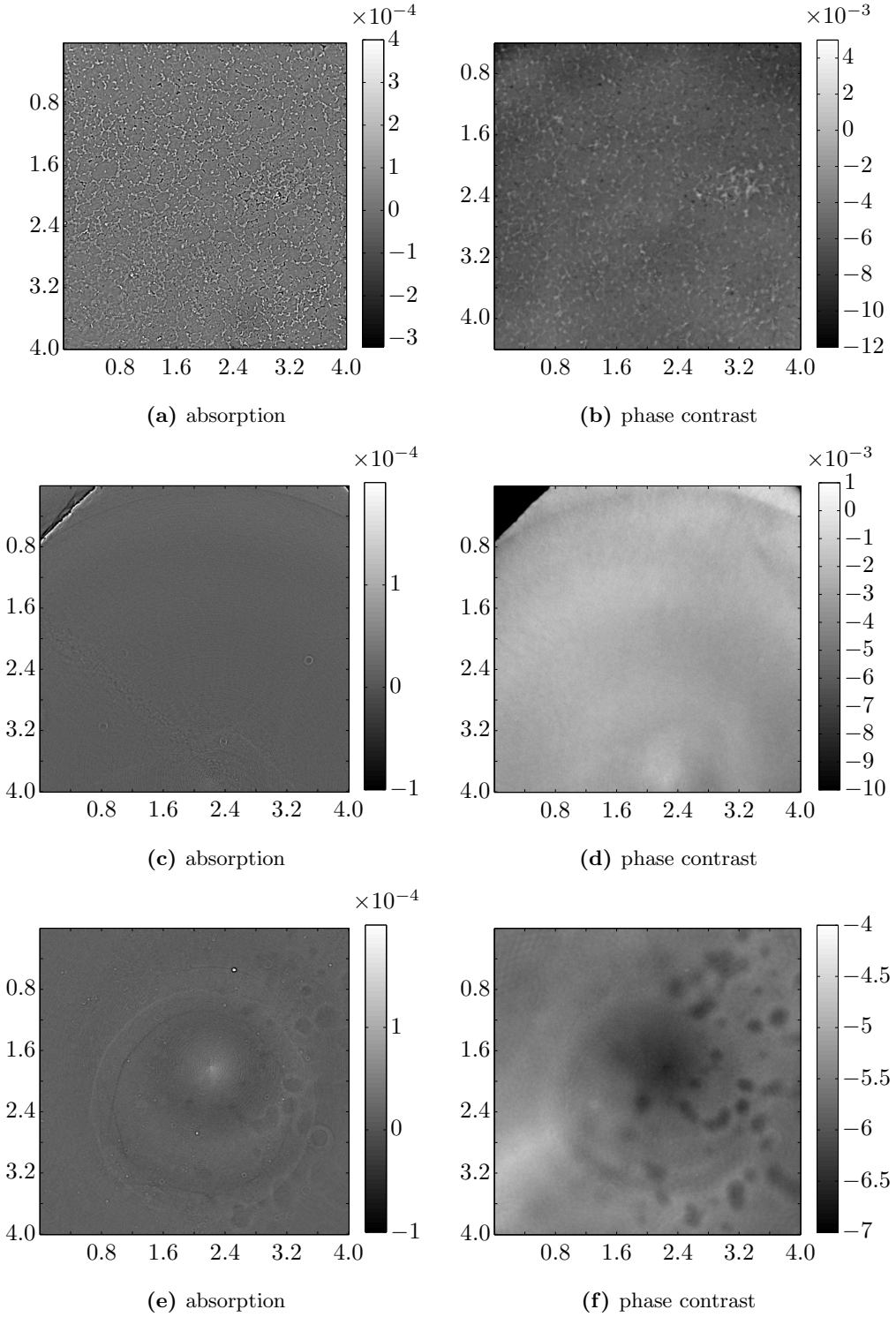

(a) absorption **(b)** phase contrast

(c) absorption **(d)** phase contrast

(e) absorption **(f)** phase contrast

Figure 4.10: Slices through the reconstructed 3-D volumes of the biopolymers 2-90 % UHMWPE (GUR4022) and 10 %PVDF, 3-UHMWPE (GUR4022) and 5-80 % UHMWPE 20 %LDPE-modified (ozon) acquired with grating interferometry. Image axes are in mm.

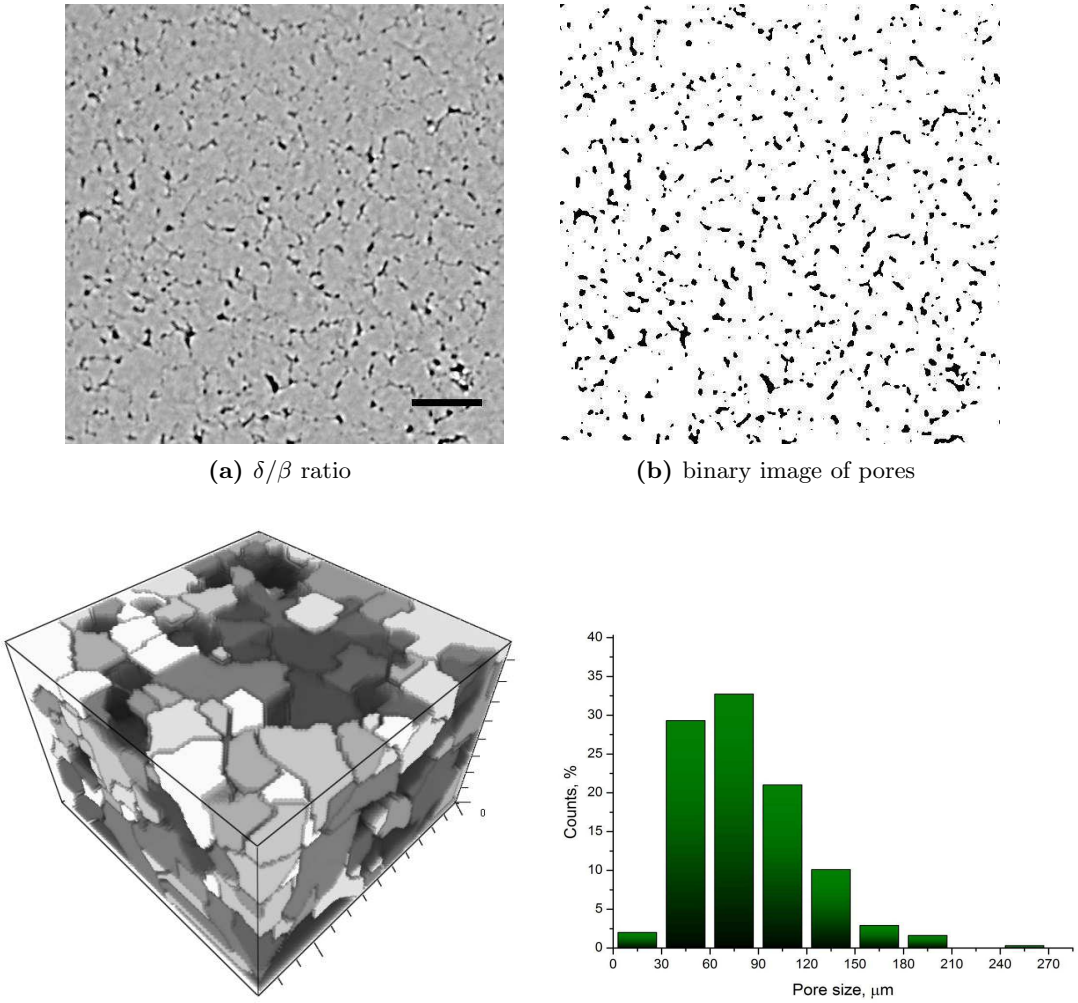

(a) δ/β ratio **(b)** binary image of pores

(c) 3-D pore distribution **(d)** statistics

Figure 4.11: (a) the ratio of the real part of the refractive index and it's decrement. (b) binary mask obtained from the image (a). (c) 3-D rendering of the pores within the sample. (d) pore distribution within the polymer scaffold. The scale bar is 200 μm.

which makes them similar to organic cartilage or bone tissue. The average diameter of the pores varies from 28 to 245 μm.

The derived pore size distribution of the 3-D volume shows an average diameter of pores between 60-90μm, around 21% have diameters of 90-120 μm and 14% of the pores are bigger than 120 μm. The latter one is considered as the optimal pore size for bone tissue integration. Around 32% of the pores are smaller than 60 μm. The relevant cell type in articular cartilage are Chondrocytes which have a diameter of 10-13 μm and

can prolifirate in the bigger nishes. The low average pore size of $<100\mu$m and the low porosity may potentially limit the access to nutrients in comparison to the larger pores in the investigated material.

Still, the combination of UHMWPE and PVDF demonstrates high potential as material for scaffolds and implants. Further increase of porosity and pore size might increase its biocompatibility and regeneration of the tissue. Future experiments in this project aim on fabricating more porous materials and visualizing the tissue integration within the implant *in vitro*, which will be possible for the first time with the new grating interferometer approach described in the chapter.

5 High-sensitivity phase contrast imaging

Contents

This chapter describes the development of a modular grating interferometer at the 3^d generation synchrotron ESRF, Grenoble, France utilizing high photon flux and high degree of monochromatisation for phase contrast imaging. The realization of multiple contrast laminography imaging based on Talbot grating interferometry is reported. By implementation of the grating interferometer into a dedicated laminography setup the advantages of both methods were brought together. The instrumental implementation, the range of the detectable phase shift and the possibility to adjust it for different application cases. Then, the dependance on the secondary structure of the three object contrast functions is demonstrated by studying the folding mechanism in bat wing membranes. Finally, the method is exemplarily applied for x-ray diagnostics of new and historical parchment from the so-called Dead Sea scrolls.

5.1 The ID19 beamline

The European Synchrotron Radiation Facility is an international research facility. It is a third generation synchrotron facility with an operating energy of 6 GeV. The ID19

Parameters	Values and descriptions
Energy range	7 keV-100 keV
Energy resolution [ΔE/E]	bandwidth of 10^{-2} or 10^{-4}
Source	two undulators (U32/U17), wiggler (W150)
Divergence	2 mrad x 0.5 mrad (H x V)
Source size	135 μm x 25 μm (FWHM, H x V)
Distance source-sample	145 m
Flux at sample position	$\approx 10^{11}$ ph/s/mm^2 (DCM)
Optics	slits, C 0.3 mm and Be X mm windows

Table 5.1: ID19 beamline characteristics (88).

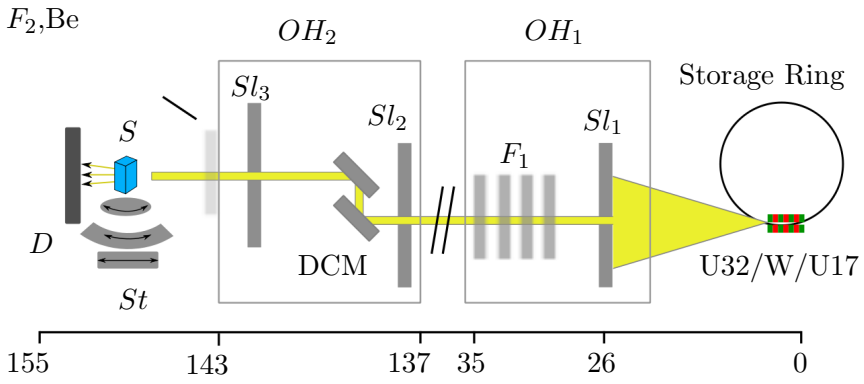

Figure 5.1: Schematics of the ID19 beamline layout.

beamline at the European Synchrotron Radiation Facility is dedicated to x-ray micro-tomography experiments, including in-line phase contrast imaging (88). The source size of ID19 and the length of the (145 m) guarantee more than sufficient transverse coherence for grating interferometry at higher Talbot orders. The parameters of the ID19 beamline are summarized in Table 5.1. The large energy range and the high coherence of the ID19 beamline makes it an apparent choice for high-sensitivity grating interferometry.

The ID19 beamline layout and the propagation distances between the optical elements are shown on Fig. 5.1. Three exchangeable insertion devices, a double crystal and a double multilayer monochromator are part of this beamline.

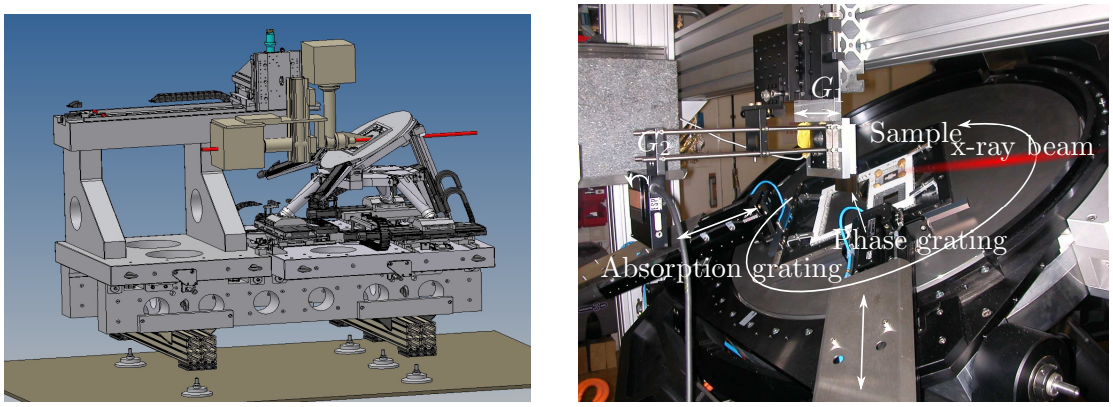

(a) Laminograph **(b)** GI unit

Figure 5.2: The 3-D drawing of the laminograph installed at ID19 and the photograph of the grating interferometer modular unit.

One of the end stations at ID19 beamline positioned at 145 m downstream of the source is the laminogrpahic instrument developed, implemented and operated by KIT. The setup consists of two main manipulation system units: the laminography sample stage and the detector manipulator which is movable along the optical axis to perform inline phase contrast imaging. Within this work, the Talbot grating interferometer was integrated, into the existing instrument.

5.2 Interferometer design

In the laminographic setup (see Fig. 5.2), the sample manipulation unit is designed to perform measurements in both tomography and laminography geometries. The laminography angle can be easily adjusted in the range from 45 ° to 70 °. The detector manipulator holds a pixel array x-ray detector with a specified resolution down to 0.5 μm pixel size. It also permits detector translation along the optical axis to set the wavefield propagation distances between the object and the detector plane (up to max. 1 m downstream of the sample rotation center).

The principal advantage of the laminography setup at ID19 is a dedicated large-diameter sample rotation table with a large aperture for x-rays. When laminography measurements are performed, the rotational table is tilted versus the optical axis, such that the x-ray beam passes through the center of the rotation table, where the large

aperture allows the x-rays to travel through the specimen without hitting the table itself or any specimen holder which could introduce an additional disturbance of the wavefield. Moreover, an external positioning systems perform sample translation for 2-D scanning over an area up of to 158 x158 mm^2. As a result, employing the laminographic rotation geometry, 3-D measurements of selected regions of interest (ROI) can be recorded with variable resolution and without special preparation, i.e. sample extraction. Also, continuous high-resolution 3-D imaging of large specimen areas can be performed by repeating full-field computed laminography and systematically translating the sample through the center of the rotation table. In this way, combining the inherent full-field method with translational scanning, an enlarged effective field of view can be realized without additional artifacts.

Within this thesis, a compact grating interferometer setup with phase and absorption gratings downstream of the sample was implemented. The grating interferometry setup was suspended above the sample manipulator from a frame-bridge system with two translation stages for the positioning of the gratings into the beam path and with a rotational stage for grating alignment (see Fig. 5.2). The grating interferometer was further equipped with a piezo actuator in order to perform the phase-stepping scan. The system allows manually to adjust any required Talbot distance in the range from 2 cm to 40 cm.

The phase and absorption gratings with pitches of 2.4 μm were fabricated by the LIGA process at KIT (see Chapter 3.1), the first was made of 4 μm thick Ni (acting as a $\pi/2$-shift grating), the latter made of gold with a aspect ratio of 100. The Moíre patterns were detected using CCD based "Frelon 2k" camera developed at the ESRF (with a 2048 x 2048 pixel array) (51). Using an optical lens coupled to a thin-film crystal scintillator (LuAg 125 μm), an effective pixel size of 5.02 μm was providing a field of view of about 10 mm x 10 mm.

5.3 Selection of the source at ID19

In order to achieve high-sensitivity grating interferometry, the coherence volume of the x-ray source has to be optimized. The undulators are the source of choice as they provide less divergent x-ray beam and narrow spectra than the wiggler. Since the transverse coherence length is developed during propagation (see Eq. 2.45) it is

important to avoid the usage of any optical elements to preserve the coherence length. Thus, no filters and no monochromators were used. The choice of undulator and its gap was done based on the respective spectra shown in Fig. 5.3 (a). The U32 undulator provides a rather soft x-ray spectrum for large gaps, which becomes harder but also broader (acting as a wiggler) for small gaps. In contrast, it was possible to optimize the gap of the U17 undulator a peak energy of 18 keV and with an energy bandwidth of dE/E of about 0.1 well suited for the experiments.

This is underlined by the Talbot carpets for the two undulator, shown in Fig. 5.3 (c-e). While the carpets for the U32 undulator are not satisfactory, the Talbot carpet of the U17 undulator clearly allows for the use of high Talbot orders. The visibility of the grating interferometer is high enough (ca. 60 %) to perform imaging even at the 5^{th} Talbot order.

5.4 Proof of principle experiments

After implementation of high-sensitivity grating interferometry setup to dedicated laminographic station, the phase sensitivity, selectivity and correlation of three contrast functions in high quality has to be confirmed.

5.4.1 Sensitivity calibration

In order to characterize the sensitivity of the grating interferometer, a phantom sample was imaged in laminographic geometry. The sample consists of two meshes made of similar in density and chemical composition polymers, such as polyethylene and polyamid. The polyethylene mesh has 41 μm thick fibers spaced by 21 μm. The polyamid mesh consists fibers of 39 μm thick fibers spaced by 50 μm. The polyethylene mesh was placed closely on top of the polyamid mesh and imaged at 18 keV with 1600 projections over 360 degrees. 2-D slices through the reconstructed volume are shown in Fig. 5.4 for absorption, phase, and dark-field contrasts.

Even though the meshes are closely packed and at the limit of the spatial resolution of the system, they are clearly resolved in all contrast modes. The phase shift introduced to the wave-field by these two meshes were calculated based on the chemical composition, density, and thickness of fibers. The theoretically expected phase shift at 18 keV is only $2.74{\cdot}10^{-11}$ rad for polyethylene and $3.10{\cdot}10^{-11}$ rad for polyamide. Even though

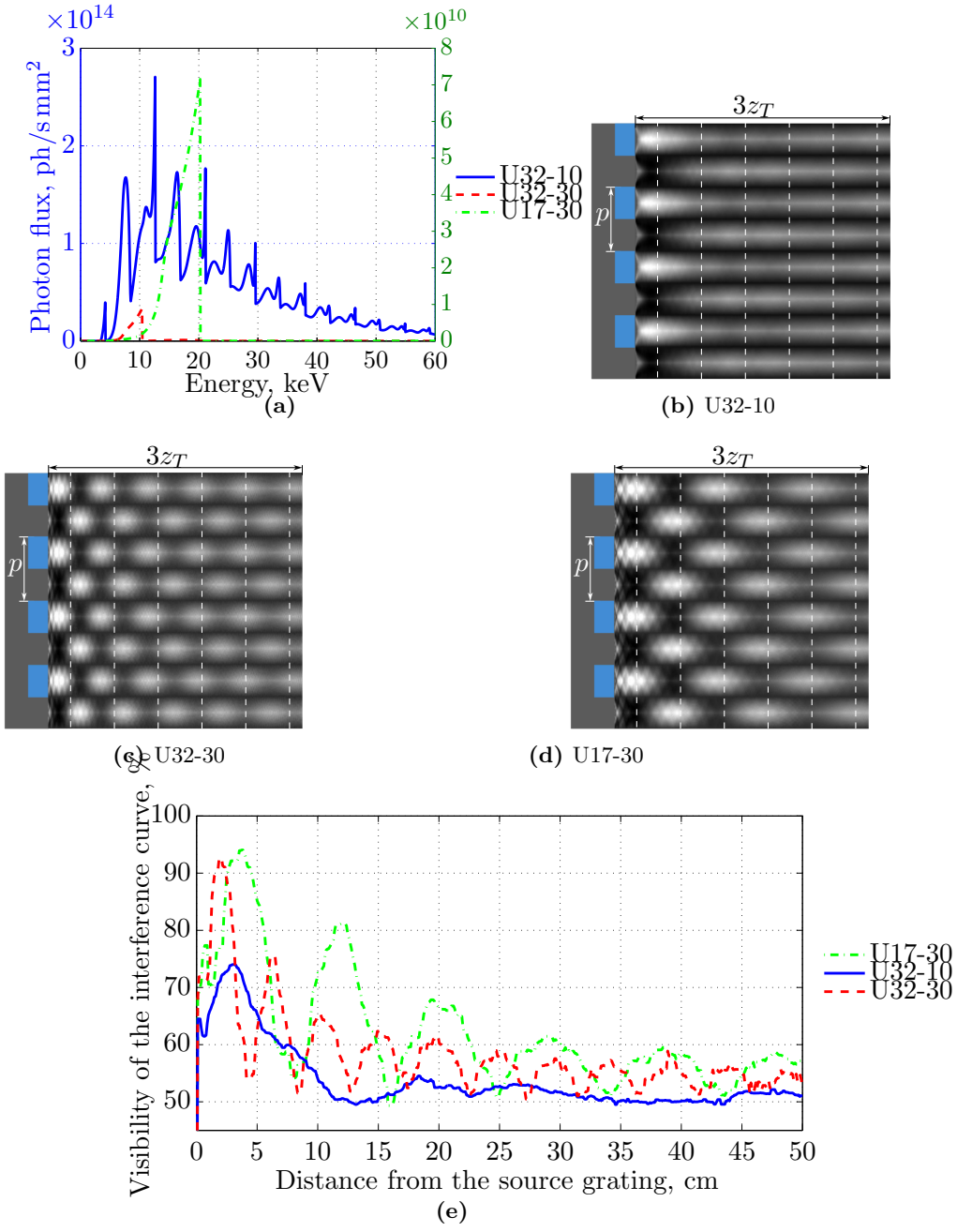

Figure 5.3: (a) The normalized photon flux spectra of the undulator with 32 mm period length with gaps of 10 mm and 30 mm and the undulator with 17 mm period length with a gap of 30 mm. All spectra include a 0.3 mm thick C window and a 500 μm thick Be window. The Talbot carpets behind the grating corresponding to the (b) U32 with a gap of 10 mm, (c) U32 with a gap of 30 mm, and (d) U17 with a gap of 30 mm. The expected visibility of the interference pattern behind $\pi/2$ phase shift grating (e) corresponding to the spectra in (a). By white dashed line marked theoretical fractional Talbot orders.

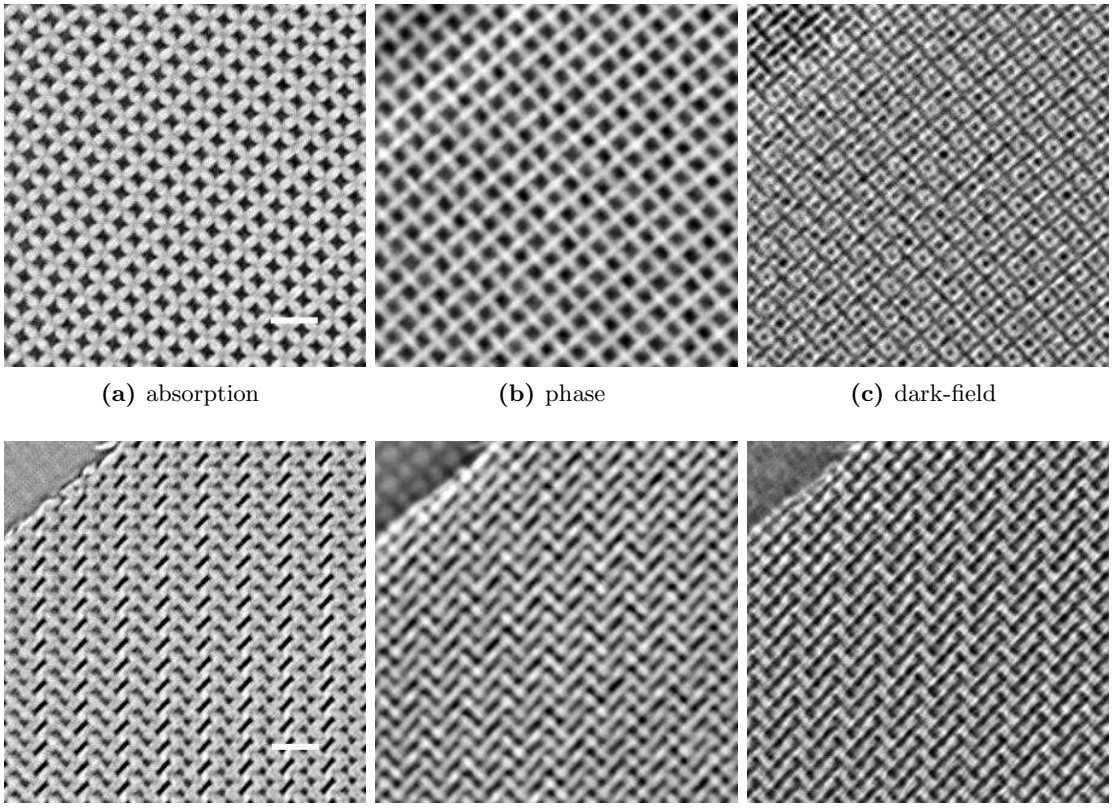

(a) absorption **(b)** phase **(c)** dark-field

(d) absorption **(e)** phase **(f)** dark-field

Figure 5.4: Reconstructed slices of polyamid (a-c) and polyethylene (d-f) meshes in absorption, phase, and dark-field contrasts. The scale bar is 100 μm.

the phase shift difference between two meshes is not significant, the experimental data is in good agreement with theoretically predicted. The phase shift introduced by the polyethylene mesh is $2.89 \pm 0.62 \cdot 10^{-11}$ rad and by the polyamide is $3.12 \pm 0.62 \cdot 10^{-11}$ rad. Experimentally found phase shift is in close agreement (20 % of error) with the theoretically calculated values. Thus, materials with very small difference in refractive index can be distinguished with high-sensitivity grating interferometry.

5.4.2 Phase selectivity

The high-sensitivity grating interferometry can be adjusted to be selective to particular phase shifts depending on it's application. As both phase and dark-field contrasts are determined by the detectable refraction angle, the phase selectivity of grating interfer-

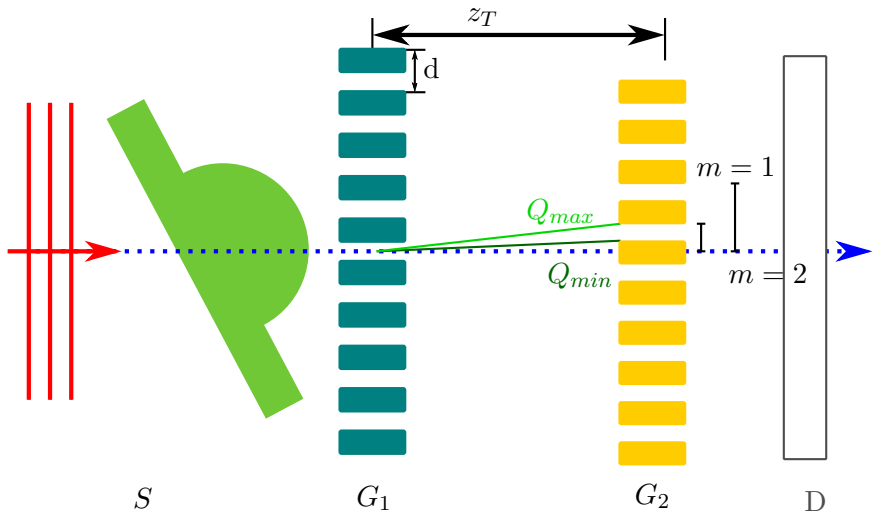

Figure 5.5: Determination of the minimal and the maximal scattering vector in the first-order component of the interference pattern produced by the phase grating.

ometry can be understood using the reciprocal scattering vector Q. Figure 5.5 shows a schematic of a grating interferometer. The angular range of the interference pattern produced by the phase grating and recorded by the detector downstream of the absorption grating is limited by the two scattering vectors Q_{min} and Q_{max}. The theoretical calculation of the Q_{min} and Q_{max} depend on the energy of the x-ray photons, period of the absorption grating p, and the Talbot distance z_T used during the experiment (as previously described in Eq. 2.29).

Considering higher orders m, the minimum and maximum detectable angles can be defined as follows:

$$\begin{aligned} \Theta_{min} &= arctan\left((m-\tfrac{3}{4})\tfrac{p}{z_T}\right) \\ \Theta_{max} &= arctan\left((m-\tfrac{1}{4})\tfrac{p}{z_T}\right) \end{aligned} \tag{5.1}$$

The minimum and maximum detectable scattering vector then follows from $Q = \frac{4\pi}{\lambda}\sin(\Theta)$. Taking into account that the Talbot distance is determined by the period of the grating and the wavelength of the x-rays as well, the sensitivity of the grating interferometry can be tuned via Talbot order n and wavelength (typically the period of the grating is remaining constant).

As proof of principle, a historical parchment was imaged with the grating interferometer at two different settings: 18 keV, 5^{th} Talbot order, and 25 keV 3^d Talbot order.

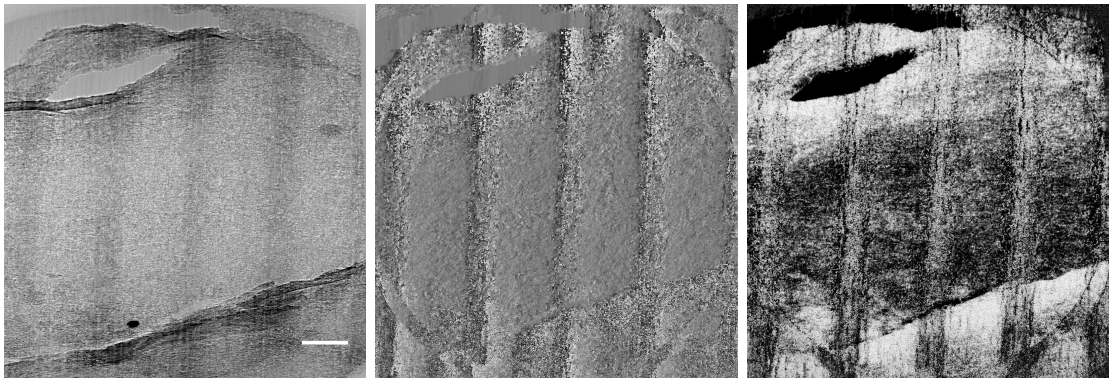

(a) absorption **(b)** phase **(c)** dark-field

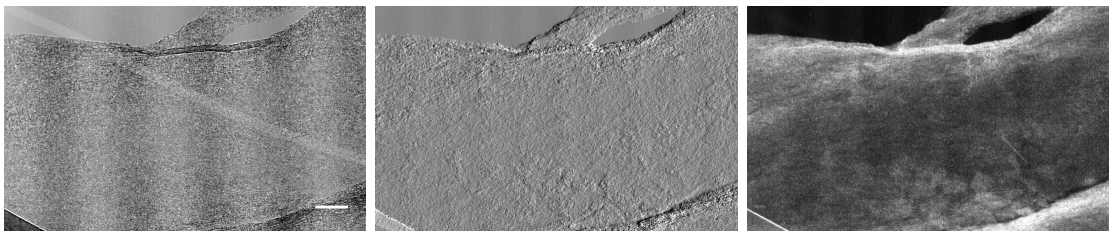

(d) absorption **(e)** phase **(f)** dark-field

Figure 5.6: 2-D radiographs of the historical parchment (Dead Sea Scrolls) measured in the 5^{th} (a-c) and 3^{d} (d-f) Talbot orders. The scale bar is 500 μm.

The 2-D projections in absorption, phase, and dark-field contrasts are shown on Fig. 5.6.

The historical parchment consists of collagen fibers (ca. 50 nm in diameter) randomly oriented and thus is a highly scattering material. At 18 keV and with the 5^{th} Talbot order (Fig. 5.6, top), only absorption contrast shows the sample structure. The dark-field contrast is very strong, especially at the edges of parchment. At the same time, the phase contrast image of the same regions looks like a speckle pattern without any visible features. In this case, the scattering from the sample was so high that the phase-stepping curve didn't possess any wave profile anymore as can be seen in Fig. 5.7, right.

The same region of the historical parchment was investigated at 25 keV and 3^{d} Talbot order (Fig. 5.6, bottom), keeping the other settings of the experiment constant. The images in Fig. 5.6, (bottom) exhibit a significantly improved image quality since these settings, now result in a reasonable phase stepping curves (see Fig. 5.7, left). In

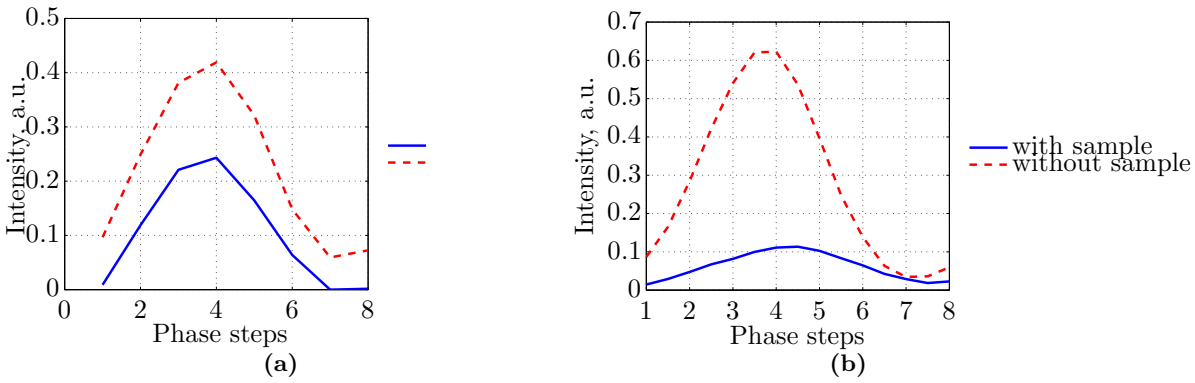

Figure 5.7: Phase stepping curves for radiographs in Fig. 5.6 for different Talbot orders: left 3^d and right 5^{th}.

conclusion, the grating interferometer can be tuned to allow for highest phase-sensitivity depending on the sample composition.

5.4.3 Multiple contrast imaging

In this work, the full advantages of both laminography and high-sensitivity grating interferometry are employed: that is to enable large effective fields of view for large specimens, to zoom with high resolution into a region of interest (ROI), and finally to obtain the correlated information of absorption, phase, and dark-field contrasts. For demonstration the wing membrane of a bat (*Microchiroptera, Pipistrellus pipistrellus*) was imaged.

The large "mesh-scanned" radiograph of the entire bat wing in the folded state (Fig. 5.8) give a first overview. In addition, laminographic 3-D zooms into ROIs of the wings are depicted. In Fig. 5.9: one 3-D rendering of the reconstructed volume for the folded and one for the unfolded states respectively. All contrast functions were individually reconstructed and later correlated into a single multiple contrast image, according to the depicted color coding. For all figures, identical color coding (yellow: absorption, red: phase shift, and blue: dark-field), thresholds and visualization parameters, such as brightness and transparency have been used. In the images, all anatomic features of considered length scales and resolution are recognized, in particular: bones and joints, blood vessels, the scaffold of transversal elastine fibres, and the membrane with

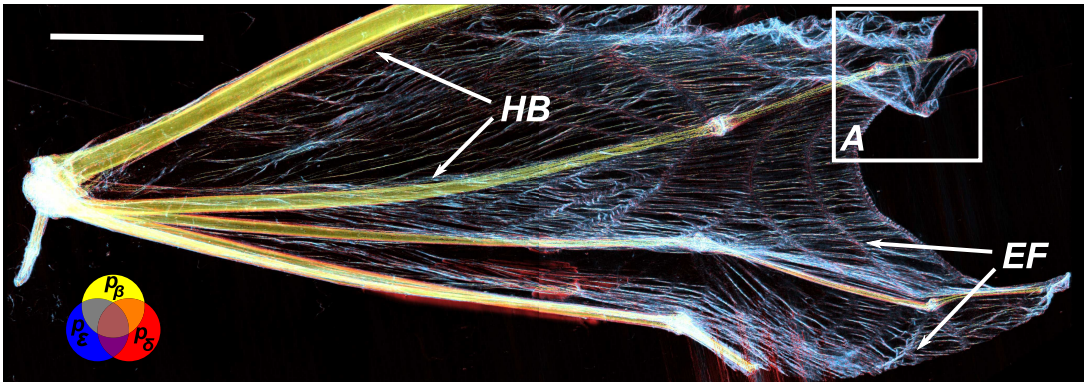

Figure 5.8: 2-D multiple contrast radiograph of a bat wing in folded state. All contrast functions are combined in the single multiple contrast image as depicted by the color coding. Line integrals along the beam path p_β, p_δ, and p_ϵ are absorption, phase and dark-field projection functions correspondingly. All contrasts have a linear gray scale, where p_β is ranging from 0.7 to 0.9 a.u., p_δ from 0 to 0.76 a.u., and p_ϵ from -1 to -0.48 a.u.. Here, HB means hollow bone and EF-elastine fibres. The area A depicts the region for 3-D visualisation shown in Fig. 5.9. The scale bar is 5 mm.

additional longitudinal fibre bundles carrying the skin. In the individual figures the various anatomic features are highlighted by different contrast composition.

The predominance of a certain contrast function for a given anatomic feature, for example the membrane, is strongly depended on its secondary morphology, such as the membrane superstructure in the folded and unfolded states. In the radiograph (Fig. 5.8), absorption contrast clearly dominates the hollow bones. Dark-field reveals the complete network of fibre bundles. Phase contrast slightly enhances elastine fibres and the ultrastructure of the trailing edge. In the 3-D rendering of the unfolded wing, where the membrane fans out into a stretched "accordion bellow" in order to predetermine the potential folding direction (Fig. 5.9), the phase gives a significant contrast contribution. Sole phase contrast depicts the elastine fibres and parts of the stretched membrane. It is superposed only by slight contributions of absorption and dark-field and interrupted by "black" regions, where no sufficient signal from any contrast mechanisms is available. Different contrast composition characterises the reconstructed 3-D image of the folded wing. The membrane is rather dominated by dark-field contrast with slight contributions of an absorption signal. This can be explained by the peculiarity of the absorption, phase, and dark-field contrasts. The absorption contrast is recon-

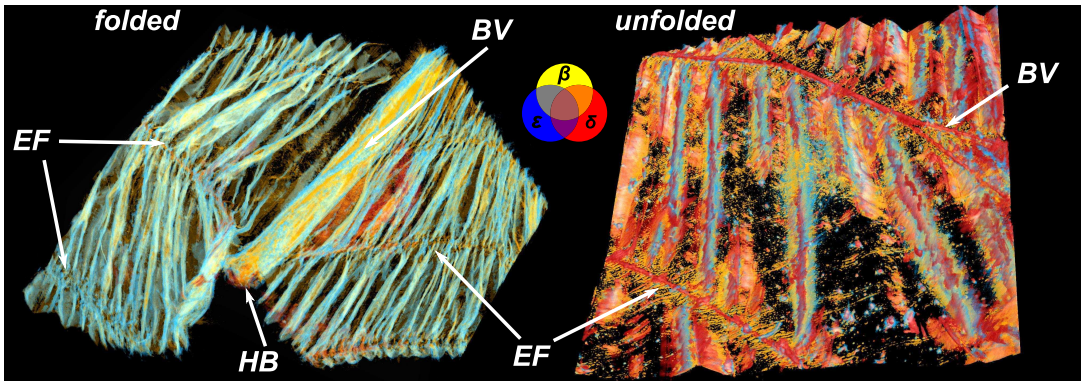

Figure 5.9: Multiple contrast 3-D renderings of the thin wing membrane in folded and unfolded states. Dark-filed contrast is represented by linear diffusion coefficient ϵ, absorption and phase contrast is represented by imaginary β and real δ part of the complex refractive index n, correspondingly. (HB-hollow bone, EF-elastine fibres, BV-blood vessels).

structed from the projections of the purely material-dependent absorption coefficient $\mu(\boldsymbol{r})$. From the theoretical description, the phase contrast in grating interferometry depends on the scalar product of the grating diffraction vector and the gradient vector of the specimen's electron density projection - the so-called differential phase. Dark-field contrast is generated by scattering, including Fraunhofer and Fresnel diffraction by the specimen's nano- and micro-structures respectively. Especially the contribution of Fresnel diffraction to the dark-field contrast, which is believed to be major for the specimen and experimental setup, is inherently dependent on the secondary structure of the wing and its orientation in the beam path. Evidently, for the investigated specimen, the dark-field contrast increases significantly as the membrane becomes folded. In this state, strong folding and buckling of the membrane enhances scattering, thus increasing dark-field at the cost of phase sensitivity of the reconstruction procedure for GI.

More generally, even for identical tissue (of identical mass density, mean electron density, and nano-structure) the absorption, phase, and dark-field contrasts behave differently under the influence of changed secondary morphology at the micrometer level, finally leading to varying contrast composition in the correlated images.

5.5 Parchment degradation

This example illustrates, the potential of laminography based on Talbot interferometry for the study of parchments. For very long time, parchment has been used as a material for writing. A group of antique collective texts from the Hebrew Bible, parabiblical and Jewish sectarian texts and is known as the Dead Sea Scrolls was made by parchment from animal skin, such as sheep and goats (11). Due to the storage conditions, exposure to light, as well as influence of humidity and bacteria, the persistence of these manuscripts is in great danger. In order to preserve such significant historical documents of mankind, understanding of the parchment structure and its deterioration processes is of fundamental interest for our cultural heritage.

Parchment degradation has been studied by other x-ray methods such as x-ray diffraction, fluorescence analysis, and x-ray absorption near edge structure (53, 63). Recently, absorption tomography of a small piece of the Dead Sea Scrolls indicated the advantages of 3-D non-destructive imaging (26).

In order to understand how the degradation of the parchment occurs, freshly prepared parchment was examined in comparison to already degradated parchment from the Dead Sea Scrolls. Due to inhomogeneity of the parchment and its complex structure, Talbot interferometry based laminography was applied so that multiple-contrast information can be used.

The preparation techniques of parchment and ink from Dead Sea Scrolls have been studied via several analytical techniques, which should allow mimicking the traditions used by the ancient Jewis scribes, who prepared their own parchment and ink for the Dead Sea Scrolls. Scientists are interested to find out, whether their mimicked parchment fabrication process significantly mimics the recipes which were used at Qumran and other sites during the second Temple period (300 BC-70 AD).

There are two main recipes today used by orthodox circles in Jerusalem: One based on the slake (lye) method, whereas the second one uses potash made of ashes of burned wood. Both, however, start with the depilation, or de-hairing, of the fresh hide after fat and tissue have been removed, either mechanically or manually, by continuous scraping and grinding the hide to the wanted thickness. After depilation, the raw hide is tanned in a concoction made of organic matter such as Rhus leaves or oak galls known for their tanning properties. Subsequently, the hide is rinsed well and is stretched over a frame

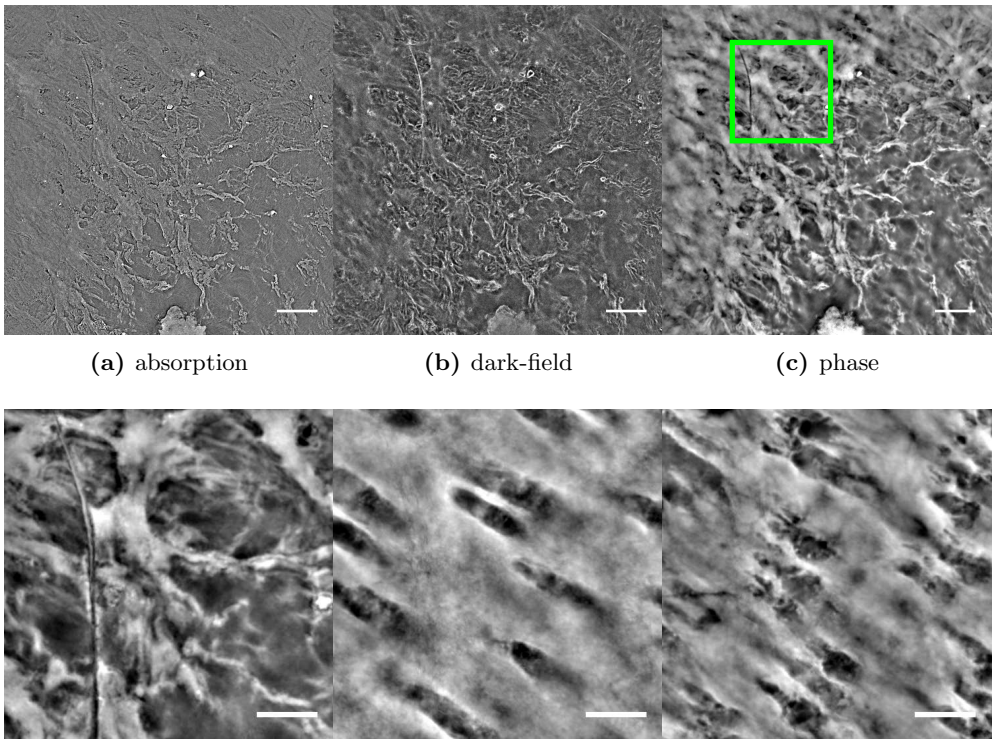

(a) absorption **(b)** dark-field **(c)** phase

(d) flesh side **(e)** flesh-to-skin transition **(f)** skin side

Figure 5.10: Figures (a-c) show absorption, dark-field, and phase contrast slices through the reconstructed 3-D volume of the freshly prepared parchment. The scale bar is 1 mm. Figures (d-f) are the phase contrast slices at different heights, through the 3-D laminographic volume of the parchment. The thickness of the piece is 280 μm. Figures (d) and (f) are recto (skin) and verso (flesh) sides correspondingly. Figure (e) depicts a slice through the middle of the volume at 140 μm from the surface. All images are the zoomed ROI from the Fig. (c). The scale bar is 500 μm.

in a well-vented room without making use of sunlight that eventually would destroy the skin. When the entire skin is dry, which can take one or two days depending on the temperature, it is cut into pages of specific size. The fresh parchment skin used in this study was prepared according to the slake/lye technique.

Here laminography was applied within a feasibility study, investigating whether structural information from both fresh and historical parchment can be gathered. In more detail, according to fabrication procedure and the type of material used, morphological variation going from the bottom to the top side of the parchment can be expected.

Slices through the reconstructed 3-D volumes of absorption, dark-field, and phase contrast from the freshly prepared parchment are shown in Fig. 5.10 (a-c), respectively. The slices correspond to the verso (back or flesh) side of the parchment. All three images of different contrast show details of the fat-like structure in the parchment. Further, the absorption contrast image (Fig. 5.10 a) indicates highly absorbing particle-like components, which could come from the sample preparation or storage. The dark-field image (Fig. 5.10 b) enhances interfaces inside the parchment structure and especially highlights the scattering signal from the particles within it. Parchment is a weakly absorbing material. As expected, the phase map (Fig. 5.10 c) gives best contrast, at least, for the parchment tissue. The three slices selected in Fig. 5.10 (d-f) zoom into a region of interest and show phase contrast images for three different but equidistant depths. In the slices we observe a characteristic variation of the porous microstructure, especially from Fig. 5.10 d to 5.10 e. The slices also indicate lateral density variation within the parchment material.

A piece of degradated parchment from one of the Dead Sea Scrolls (QUM 922, Cave 4) is visualized in Fig. 5.11 (a-f). One can clearly observe the structural changes due to degradation if comparing the slices of fresh and historical specimen. Already by naked eye, both are fundamentally different. Absorption, dark-field, and phase contrast slices taken from the same depth of the parchment are shown in Fig. 5.11 (a-c), demonstrating the strong structural changes suffered over time. The dark-field image 5.11 (b) shows that the area density of the interfaces inside the parchment has considerably increased which might be due to the appearance of micro-fissures inside the former tissue. Overall, the parchment's structure has decomposed and shrunk to a large extent. Also, significant warpage occured. On all phase contrast slices taken at different depth of the parchment (Fig. 5.11 (d-f)), discover the formation of collagen fibrils, particle-like structures, and micro-cracks is clearly visible compared to the formerly much more homogeneous material of fresh parchment. The detailed morphology of collagen fibrils varies from one slice to the next. At the edges of the parchment the collagen fibrils are more structured and more dense. So, in the examined sample the parchment was preserved better at the edges. The observation, that the collagen system seems to be more disordered in the center of the parchment, supports the earlier hypothesis that the deterioration might have developed from the inside towards the outside (63).

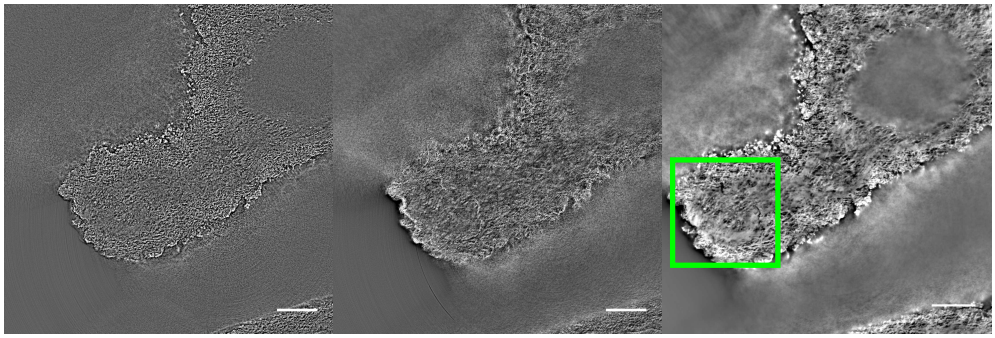

(a) absorption **(b)** dark-field **(c)** phase

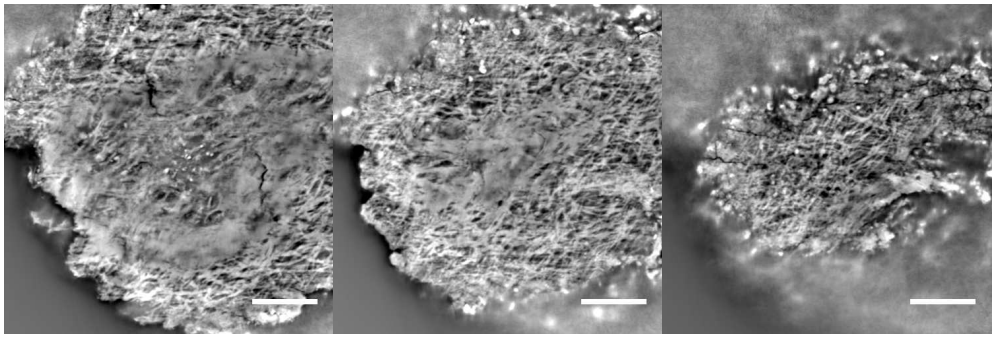

(d) flesh side **(e)** flesh-to-skin side transition **(f)** skin side

Figure 5.11: Figures (a-c) show absorption, dark-field, and phase contrast slices through the reconstructed 3-D volume from the small piece of Dead Sea scrolls. The scale bar is 1 mm. As for the freshly prepared parchment, figures (d-f) show phase contrast slices at the different depth of parchment (zoomed region from (c)). The total thickness of the parchment from the Dead Sea scrolls is about 150 μm. The scale bar is 500 μm.

Under methodical points of view, it can be concluded that grating interferometry combined with laminography is a very promising technique for systematic studies of historical parchment degradation, such as Dead Sea Scrolls and others. Moreover, applying the phase-stepping technique, images of different contrast modes can be retrieved making absorption, dark-field, and phase contrast simultaneously available. Systematic use of multiple-contrast images will provide more complementary understanding of structural changes within a 3-D volume. Since the method enables to non-destructively scan large volume of parchment and to zoom into various regions of interest with variably chosen resolution, the technique seems presently to be the only 3-D method allowing to perform representative studies of structure changes.

6 Conclusions

The aim of the thesis was the development and implementation of a Talbot grating interferometry for imaging of flat samples with high speed. The results of the thesis can be classified in three parts: theoretical considerations, instrumentation development, and application of grating interferometry to different specimens.

In the first part, Talbot grating interferometry in laminographic geometry was theoretically described. Reviewing the forward problem of image formation and the inverse problem for data retrieval of gratings-based laminography, the main reconstruction equations have been developed in both real and reciprocal space (5). These equations and considerations form the basis for the optimization of the experiments and setups in the following parts of the thesis. The reconstruction routine includes a computation-time efficient 1-D projection filter and a filter adapted to retrieve the spatial electron density modulation of the object from differential phase images. This allows to extract - within a single measurement - information on the 3-D distribution of the specimen's properties to attenuate, scatter, and phase-shift the probing x-ray wave field.

In the second part of this thesis, a procedure for quality assurance of the gratings to be used in grating interferometry is developed. Based on the visibility of the contrast curve, its standard deviation, and signal to noise ratio, it is possible to determine the optimal grating set for high quality imaging experiments (46). A new concept for the fabrication of phase gratings with periods matching the x-ray divergence was introduced - the tilted grating design. In experiments, tilted grating structures showed high visibility of the contrast curve (comparable with the normal grating design), while suppressing the Moiré fringes present with the conventional design, thus being more suitable for grating interferometry.

Furthermore, a Talbot grating interferometry setup was integrated into existing tomographic and laminographic stations (4). The interferometers were set up at two different synchrotron facilities and beamlines the high-speed setup at the TopoTomo beamline at the ANKA light source and the high-sensitivity setup at the ID19 beamline at the ESRF. Based on the theoretical framework developed in the first part of the thesis, two separate, one, for high phase sensitivity and on optimized for high-speed

Parameters	High-speed setup	High-sensitivity setup
Beamline	TopoTomo, ANKA	ID19, ESRF
Energy range [keV]	6-40	7-100
Energy resolution [ΔE/E]	white light (optional 10^{-2})	bandwidth of 10^{-2} or 10^{-4}
Available Talbot distances [mm]	10-800	20-400
Available Talbot orders	1	1, 3, 5
Minimum detectable phase shift [μrad]	50	9
Maximum sample size V x H [mm]	6 x 8	158 x 158
Exposure time [s]	0.001	2
Total time for tomogram [min]	0.07	120

Table 6.1: Basic parameters for high-speed and high-sensitivity grating interferometers.

experiments were implemented. The basic parameters of the two realized instruments are shown in Table 6.1.

The capabilities of the high phase sensitivity setup was demonstrated for a few examples which pointed out the possibility of distinguishing materials with very similar properties as well as giving the possibility for phase selectivity and correlation of three contrast functions available with grating interferometry.

In the high-speed setup, the measurement time needed for grating interferometry could be reduced by approximately 4 orders of magnitude, opening the window for entirely new experimental possibilities in grating interferometry.

Based on the methodical and instrumentation developments, the third part of the thesis describes a wide variety of imaging applications covering material science, cultural heritage, and biology as for high-speed as for high-sensitivity setups.

6.1 Perspectives

Based on the research work on Talbot grating interferometry in this thesis novel routes for a further improvement of the technique can be envisioned. Some of them will be discussed in the following.

1. The high-speed grating interferometer at the TopoTomo beamline could be further optimized to the increase available Talbot distances and thus the minimum

detectable phase shift. The required improvement in transverse coherence can be achieved by utilizing a third so called source grating, preferably installed a few meters upstream of the instrument. The third grating would decrease available flux at the beamline only by factor of two, still allowing for high-speed measurement but offering high phase sensitivity at the same time.

2. The acquisition speed with Talbot grating interferometry can be further increased by utilizing different reconstruction routines. The three (instead of four) images phase stepping technique would still allow to reconstruct absorption, phase, and dark-field contrasts. In the cases where phase contrast only is sufficient, two image scheme would be sufficient to qualitatively reconstruct phase contrast. Finally, in application cases requiring only low resolution ($20\,\mu$m) phase contrast imaging, the Fourier method of analyzing Moiré fringes from a single image could be employed, allowing experiments four times faster than achieved within this work.

3. The high-speed interferometer developed within this thesis allows for *in situ* experiments, however not for biomedical applications. In order to pursue biomedical imaging, optimization of the radiation dose imposed on the specimen has to be performed. The optimization can include optimization of speed (described above), x-ray spectra (higher energies would be required) and the interferometry setup. For example positioning the specimen after phase grating will reduce the dose on the sample by the amount absorbed in the grating while not reducing the numbers of transmitted photons to the detector. Similarly, a suitable material enclosing the sample can function as an additional filter for the soft part of the spectrum. It can be estimated that the x-ray dose can be reduced from currently 18 Gy to below 4 Gy (below half of lethal dose for mice) which would open Talbot grating interferometry for *in vivo* application.

4. The Talbot grating interferometry could be further implemented at a laboratory source, extending its applications to harder x-ray energies and larger samples. The implementation and optimization of grating interferometry at the laboratory source would open up the market for non destructive material testing and clinical diagnostics.

5. And last but not the least, the multiple contrasts available with grating interferometry could be combined with x-ray microscopy. Retrieving attenuation, phase, and dark-field contrasts with nanometer spatial resolution will pioneer wide range of new application fields. In fact, while not a topic in this manuscript, the development of such microscope was done in the framework of this thesis. The so-called MiQA microscope is currently in the construction phase and will be installed at the IMAGE beamline in the end of 2014.

In summary, such work would push grating interferometry to become a routine technique for practical applications at the micro and nano scale for correlative imaging of attenuation, phase, and dark-field contrasts at low dose and high acquisition speeds.

List of Figures

List of Tables

References

[1] W. Yashiroi A. Momose and Y. Takeda. *X-ray phase imaging with Talbot interferometry*. Medical Physics Publishing, 2010. 26, 28

[2] Inc Aerotech. **Aerotech dedicated to the science of motion**. 64

[3] M. Allen. *UHMWPE processing: techniques and problem. UHMWPE for Arthroplasty: past, present and future*. 2003. 72

[4] V. Altapova, J. Butzer, T.d.S. Rolo, P. Vagovic, A. Cecilia, J. Moosmann, J. Kenntner, J. Mohr, D. Pelliccia, V.F. Pichugin, and T. Baumbach. **X-ray phase-contrast radiography using a filtered white beam with a grating interferometer**. *Nuclear Instruments and Methods in Physics Research A*, **648**:42–45, 2011. 93

[5] V. Altapova, L. Helfen, A. Myagotin, D. Hänscke, J. Moosmann, J. Gunneweg, and T. Baumbach. **Phase contrast laminography based on Talbot interferometry**. *Optics Express*, **20(6)**:6496–6508, 2012. 93

[6] J. Banhart. *Advanced tomographic methods in materials research and engineering*, **66**. Oxford University Press, 2008. 29

[7] E.W. Becker, W. Ehrfeld, P. Hagmann, A. Maner, and D. Münchmeyer. **Fabrication of microstructures with high aspect ratios and great structural heights by synchrotron radiation lithography, galvanoforming, and plastic moulding (LIGA process)**. *Microelectronics Engineering*, **4**:35–36, 1986. 4

[8] E.M. Gullikson B.L. Henke and J.C. Davis. **X-ray interactions: photoabsorption, scattering, and reflection at E=50-30,000 eV, Z=1-92**. *Atomic Data and Nuclear Data Tables*, **54**:181, 1993. 4, 11, 97

[9] U. Bonse and M. Hart. **An x-ray interferometer**. *Appl. Phys.Lett.*, **6**:155–156, 1965. 4, 5

[10] M. Born and E. Wolf. *Principles of optics*. Library of Congress Cataloging in Publication Data, 1980. 13, 33, 36

[11] D. Bradley and D. Creagh. *Physical techniques in the Study of Art, Archaeology and Cultural Heritage*. Elsevier, 2007. 89

[12] A. Bravin. **Exploiting the x-ray refraction contrast with an analyser: the state of the art**. *J. Phys. D: Appl. Phys*, **36**:A24–A29, 2003. 4

[13] A. Bravin, P. Coan, and P. Suortti. **X-ray phase-contrast imaging: from pre-clinical applications towards clinics**. *Physics in Medicine and Biology*, **58**:R1–R35, 2013. 3

[14] A. Burvall, U. Lundstroem, P.A.C. Takman, D.H. Larson, and H.M. Hertz. **Phase retrieval in x-ray phase-contrast imaging suitable for tomography**. *Optics Express*, **19**:10359–10376, 2011. 5

[15] J.T. Bushberg, J.A. Seibert, E.M. Leidholdt, and J.M. Bonne. *The essential physics of medical imaging*, **Third edition**. Lippincott Williams and Wilkins, 2011. 50

[16] Michael Chabior. *Contributions to the characterization of grating-based x-ray phase-contrast imaging*. PhD thesis, Technical University Dresden, 2011. 44, 55

[17] Y. Cheng, V. Altapova, L. Helfen, F. Xu, T. dos Santos Rolo, P. Vagovic, M. Fiederle, and T. Baumbach. **Multi-contrast computed laminography at ANKA light source**. *Journal of Physics: Conference Series*, **463**:012038, 2013. 59

[18] P. Cloetens, W. Ludwig, E. Boller, L. Helfen, L. Salvo, R. Mache, and R. Schlenker. **Quantitative phase contrast tomography using coherent synchrotron radiation**. *Proceedings SPIE: Developments in X-ray Tomography III*, **4503**:82–91, 2002. 10

[19] Peter Cloetens. *Contribution to phase contrast imaging, reconstruction and tomography with hard synchrotron radiation*. PhD thesis, Vrije Universiteit Brussel, 1999. 5, 12, 36

[20] P. Coan, A. Bravin, and G. Tromba. **Phase-contrast x-ray imaging of the breast: recent developments towards clinics**. *Journal of Physics D: Applied Physics*, **46**:494007, 2013. 3

[21] John M. Cowley. *Diffraction physics*. North-holland Personal Library, 1995. 5, 16

[22] K. Creath. **Step height measurement using two-wavelength phase-shifting interferometry**. *Applied Optics*, **26**:2810–2816, 1987. 26

[23] C. David, B. Noehammer, H.H. Solak, and E. Ziegler. **Differential x-ray phase contrast imaging using a shearing interferometer**. *Appl. Phys. Lett.*, **81**:3287–3289, 2002. 3, 4, 6

[24] M. Sánchez del Río and R.J. Dejus. **XOP: Recent developments**. *SPIE proceedings*, **3448**:1–5, 1998. 11, 97

[25] P.C. Diemoz, P. Coan, Ch. Glaser, and A. Bravin. **Absorption, refraction and scattering in analyzer-based imaging: comparison of different algorithms**. *Optics Express*, **18**:3494–3509, 2010. 3, 5

[26] J. Dik, L. Helfen, P. Reischig, J. Blaas, and J. Gunneweg. **A short note on the application of synchrotron-based micro-tomography on the Dead Sea scrolls in Holistic Qumran**. *Holistic Qumran*, pages 21–28, 2010. 89

[27] P.-A. Douissard, A. Cecilia, X. Rochet, X. Chapel, T. Martin, T. van de Kamp, L. Helfen, T. Baumbach, L. Luquot, X. Xiao, J. Meinhardt, and A. Rack. **A versatile indirect detector design for hard x-ray microimaging**. *Journal of Instrumentation*, **7**:P09016, 2012. 59

[28] M. Boerner V. Nazmov P.J. Jakobs E. Reznikova, J. Mohr. **Soft x-ray lithography of high aspect ratio SU8 submicron structures**. *Microsystem Technologies*, **14**:1683–1688, 2008. 42

[29] G.W. Faris and R.L. Byer. **Three-dimensional beam-deflection optical tomography of a sepursonic jet**. *Appl. Opt.*, **27**:5202, 1988. 32

[30] L.A. Feldkamp, L.C. Davis, and J.W. Kress. **Practical cone-beam algorithm**. *J. Opt.Soc.Am. A*, **1**:612–619, 1984. 29

[31] R. Fitzgerald. **Phase-sensitive x-ray imaging**. *Physics today*, **53**:1–4, 2000. 6

[32] B.P. Flannery, H.W. Deckman, W.G. Roberge, and K.L. D Amico. **Three-dimensional x-ray microtomography**. *Science*, **237**:1439–1444, 1987. 29

[33] S.H. Gage. *Modern dark-field microscopy and the history of its development*, **39**. Transactions of the American Microscopical Society, 1920. 28

[34] S. Gondrom, J. Zhou, M. Maisl, H. Reiter, M. Kroening, and W. Arnold. **X-ray computed laminography: an approach of computed tomography for applications with limited access**. *Nuclear engineering and design*, **190**:141–147, 1999. 29

[35] P. Goodman and A.F. Moodie. **Numerical evaluation of N-beam wave functions in electron scattering by the multi-slice method**. *Acta Crystallogr.*, **10**:280–290, 1974. 13

[36] W.L. Grayson, T.P. Martens, G.M. Enga, M. Radisic, and G. Vunjak-Novakovic. **Biomimetic approach to tissue engineering**. *Seminars in Cell and Developmental Biology*, **20**:665–673, 2009. 71

[37] H. Gross. *Handbook of optical systems, Vol 1: Fundamentals of technical optics*. W:Wiley-VCH Verlag, 2005. 16

[38] J.P. Guigay. **Fourier-transform analysis of Fresnel diffraction patterns and in-line holograms**. *Optik*, **49**:121–125, 1977. 15

[39] T.E. Gureyev, S.C. Mayo, G. Meyers, D.M. Paganin, A. Pogany, Y.I. Nesterets, and S.W. Wilkins. **Refracting Röntgen's rays: propagation-based X-ray phase contrast for biomedical imaging**. *Journal of Applied Physics*, **105**:102005, 2009. 4

[40] L. Helfen, T. Baumbach, P. Mikulik, D. Kiel, P. Pernot, P. Cloetens, and J. Baruchel. **High-resolution three-dimensional imaging of flat objects by synchrotron-radiation computed laminography**. *Applied Physics Letters*, **86**:071915, 2005. 17, 97

[41] G.T. Herman. *Fundamentals of computerized tomography: image reconstruction from projections*. Academic Press, 1980. 64

[42] Fraunhofer institute for industrial mathematics. **Modular algorithms for volume images**, 2014. 73

[43] J.A.Nielsen and D. McMorrow. *Elements of modern x-ray Physics*. Wiley, 2001. 10, 35

[44] R.E. Cameron J.S. Capes, H.Y. Ando. **Fabrication of polymeric scaffolds with a controlled distribution of pores**. *Journal of materials science: materials in medicine*, **16**:1069–1075, 2005. 72

[45] A.C. Kak and M. Slaney. *Principles of computerized tomographic imaging*, **1**. Society of industrial and applied mathematics, 2001. 29

[46] J. Kenntner, V. Altapova, T. Grund, F.J. Pantenburg, J. Meiser, T. Baumbach, and J. Mohr. **Fabrication and characterization of analyser gratings with high aspect ratios for phase contrast imaging using a Talbot interferometer**. *AIP Conf. Proc.*, **1437**:89–93, 2012. 93

[47] Johannes Kenntner. *Herstellung von GItterstrukturen mit Aspektverhältnis 100 für die Phasenkontrastbildgebung in einem Talbot-Interferometer*. PhD thesis, Karlsruhe Institute of Technology, 2012. 44, 46

[48] A. Kostenko, K. Joost Batenburg, H. Suhonen, S.E. Offerman, and L.J. van Vliet. **Phase retrieval in in-line x-ray phase contrast imaging based on total variation minimization**. *Optics Express*, **21**:710–723, 2013. 5

[49] S.P. Krüger. *Optimization of waveguide optics for lensless x-ray imaging*. Universitätsverlag Göttingen, 2010. 12

[50] P. Mikulik P.Pernot A. voropaev M. Elyyan M. Di Michiel J. Baruchel T. Baumbach L. Helfen, A. Myagotin. **On the implementation of computed laminography using synchrotron radiation**. *Rev. Sci. Instrum.*, **82**:063702, 2011. 29, 30

[51] J.-C. Labiche, O. Mathon, S. Pascarelli, M. A. Newton, G. Guilera Ferre, C. Curfs, G. Vaughan, A. Homs, and D. F. Carreiras. **The fast readout low noise camera as a versatile x-ray detector for time resolved dispersive extended x-ray absorption fine structure and diffraction studies of dynamic problems in materials science, chemistry, and catalysis**. *Rev. Sci. Instrum.*, **78**:091301, 2007. 80

[52] M. Langer, P. Cloetens, J.P. Guigay, S. Valton, and F. Peyrin. **Quantitative evaluation of phase retrieval algorithms in propagation based phase tomography**. *Biomedical Imaging: From Nano to Macro*, pages 552–555, 2007. 5

[53] R. Larsen. *Microanalysis of parchment*. Archetype Publications, 2002. 89

[54] R.A. Lewis. **Medical phase contrast x-ray imaging: current status and future prospects**. *Physics in Medicine and Biology*, **49**:3573–3583, 2004. 4

[55] Photron Europe Limited. **Photron High Speed Cameras**. 64

[56] A.W. Lohmann. **An array illuminator based on Talbot-effect**. *Optik*, **79(1)**:41–45, 1988. 22

[57] M.H. Maleki and A.J. Devaney. **Noniterative reconstruction of complex-valued objects from two intensity measurements**. *Optical Enginnering*, **33**:3243–3253, 1994. 16

[58] R.H. Menk. **Interference imaging and it's application to material and medical imaging**. *Nuclear Physics B: Proceedings supplements*, **78**:604–609, 1999. 4

[59] J. Mohr, T. Grund, D. Kunka, J. Kenntner, J. Leuthold, J. Meiser, J. Schulz, and M. Walter. **High aspect ratio gratings for X-ray phase contrast imaging**. *AIP Conference proceedings*, **1466**:41–50, 2012. 4

[60] A. Momose. **Recent advances in x-ray phase imaging**. *Jpn. Journal of Applied Physics*, **44**:6355–6367, 2005. 6

[61] A. Momose, S. Kawamoto, I. Koyama, Y. Hamaishi, K. Takai, and Y. Suzuki. **Demonstration of x-ray Talbot interferometry**. *Japanese Journal of Applied Physics*, **42**:L866–L868, 2003. 3, 6

[62] A. Momose, W. Yashiro, Y. Takeda, Y. Suzuki, and T. Hattori. **Phase tomography by X-ray Talbot interferometry for biological imaging**. *Japanese Journal of Applied Physics*, **45**:5254, 2006. 3

[63] B. Murphy, M. Cotte, M. Mueller, M. Balla, and J. Gunneweg. **Degradation of parchment and ink of the Dead Sea scrolls investigated using synchrotron-based X-Ray and Infrared microscopy**. *Holistic Qumran*, pages 77–98, 2010. 89, 91

[64] A. Myagotin, A. Voropaev, L. Helfen, D. Hanschke, and T. Baumbach. **Efficient Volume Reconstruction for Parallel-Beam Computed Laminography by Filtered Backprojection on Multi-Core Clusters**. *Image Processing, IEEE Transactions on*, **22**(12):5348–5361, 2013. 31, 61

[65] F. Natterer. *The mathematics of computerized tomography*. Society for industrial and applied mathematics, 2001. 24

[66] M.S. Nielsen, T. Lauridsen, M. Thomsen, T.H. Jensen, M. Bech, L.B. Christensen, E.V. Olsen, M. Hiviid, R. Feidenhans'l, and F. Pfeiffer. **X-ray tomography using the full complex index of refraction**. *Physics in Medicine and Biology*, **57**:5971–5979, 2012. 6

[67] D. Paganin, S.C. Mayo, T.E. Gureyev, P.R. Miller, and S.W. Wilkins. **Simultaneous phase and amplitude extraction from a single defocused image of a homogeneous object**. *Journal of Microscopy*, **206**:33–40, 2002. 3

[68] David M. Paganin. *Coherent X-ray Optics*. Oxford: Oxford University Press, 2006. 20, 21

[69] F. Pfeiffer, M. Bech, O. Bunk, P. Kraft, E.F. Eikenberry, C. Broennimann, C. Gruenzweig, and C. David. **Hard X-ray dark-field imaging using a grating interferometer**. *Nat. Materials*, **7**:134–137, 2008. 3, 6, 28, 69

[70] F. Pfeiffer, O. Bunk, C. Kottler, and C. David. **Tomographic reconstruction of three-dimensional objects from hard X-ray differential phase contrast projection images**. *Nucl. Instrum. Meth. Phys. Res. A*, **580**:925–928, 2007. 6, 32

[71] F. Pfeiffer, T. Weitkamp, O. Bunk, and C. David. **Phase retrieval and differential phase-contrast imaging with low-brilliance X-ray sources**. *Nature Physics*, **2**:258–261, 2006. 3, 4, 6

[72] A. Pogany, D. Gao, and S.W. Wilkins. **Contrast and resolution in imaging with a microfocus X-ray source**. *Rev. Sci. Instr.*, **68**:2774–2782, 1997. 16

[73] Microworks precision structures. **Microworks: gratings for x-ray differential phase contrast imaging**, 2012. 42, 103

[74] L. H. Schwartz and J. B. Cohen. *Diffraction from materials*. Academic Press, 1977. 11, 18

[75] C.E. Shannon. **Communication in the presence of noise**. *Proc. Institute of Radio engineers*, **37**:10–21, 1949. 60

[76] S.R. Stock. *MicroComputed tomography: methodology and applications*, **1**. OCrc Pr Inc, 2008. 29

[77] Y. Surrel. **Design of algorithms for phase measurements by the use of phase-stepping**. *Applied Optics*, **35**:51–60, 1996. 26

[78] G.J. Swanson. *Binary optics technology: The theory and design of multi-level diffractive optical elements*. Lincoln Laboratory, Massachusetts Institute of Technology, 1989. 35

[79] M Takeda, H. Ina, and S. Kobayashi. **Fourier-transform method of fringe-pattern analysis for computer-based topography and interferometry**. *J. Opt. Soc. Am.*, **72**, 1982. 26

[80] H.F. Talbot. **Facts relating to optical science**. *Philos. Mag*, **IV**, 1836. 22

[81] A. Tapfer, M. Bech, B. Pauwels, X. Liu, P. Bruyndonckx, A: Sasov, J. Kenntner, J. Mohr, M. Walter, J. Schulz, and F. Pfeiffer. **Development of a prototype gantry system for preclinical x-ray phase-contrast computed tomography**. *Medical Physics*, **38**:5910–5915, 2011. 6

[82] A. Thompson, D. Attwood, E. Gullikson, M. Howells, K-J. Kim, J. Kirz, J. Kortnight, I. Lindau, Y. Liu, P. Pianetta, A. Robinson, J. Scofield, J. Underwood, and G. Williams. *X-ray data booklet*. Lawrence Berkley National Laboratory, 2009. 11

[83] H. Gross W. Singer, M. Totzeck. *Handbook of Optical Systems: Physical Image Formation*. Wiley, 2005. 20

[84] R.H. Wade. **Spectral Analysis of Holograms and Reconstructed Images**. *Optik*, **40**:201–216, 1974. 15

[85] Z. Wang, K. Kang, Z. Huang, and Z. Chen. **Quantitative grating-based x-ray dark-field computed tomography**. *Applied Physics Letters*, **95**:094105, 2009. 32

[86] B. E. Warren. *X-ray diffraction*. Dover Publications Inc., 1990. 10

[87] T. Weitkamp, A. Diaz, C. David, F. Pfeiffer, M. Stampanoni, P. Cloetens, and E. Ziegler. **X-ray phase imaging with a grating interferometer**. *Optics Express*, **13**:6296–6304, 2005. 35

[88] T. Weitkamp, P. Tafforeu, E. Boller, P. Cloetens, J-P. Valade, P. Bernard, F. Peyrin, W. Ludwig, L. Helfen, and J. Barushel. **Parallel-beam imaging at the ESRF beamline ID19: current status and plans for future**. *AIP Conf. Proc.*, **1234**:83–86, 2009. 78, 103

[89] Timm Weitkamp. *Imaging and tomography with high resolution using coherent hard synchrotron radiation*. PhD thesis, Hamburg University, 2002. 13

[90] S. W. Wilkins, T. E. Gureyev, A. Pogany D. Gao, and A. W. Stevenson. **Phase-contrast imaging using polychromatic hard X-rays**. *Nature*, **384**:335–338, 1996. 3, 4, 5, 16

[91] M. Willner, M. Bech, J. Herzen, I. Zanette, D. Hahn, J., J. Mohr, A. Rack, T. Weitkamp, and F. Pfeiffer. **Quantitative X-ray phase-contrast computed tomography at 82 keV**. *Optics Express*, **21**(4):4155–4166, 2013. 55

[92] Y. De Witte, J. Vlassenbroeck, and L. Van Hoorebeke. **A multiresolution approach to iterative reconstruction algorithms in x-ray computed tomography**. *IEEE trans. image processing*, **19**:2419–2427, 2010. 29

[93] F. Xu, L. Helfen, T. Baumbach, and H. Suhonen. **Comparison of image quality in computed laminography and tomography**. *Optics Express*, **20**:794–806, 2011. 30

[94] A. Yaroschenko, M. Bech, G. Potdevin, A. Malecki, T. Biernath, J. Wolf, A. Tapfer, M. Schüttler, J. Meiser, D. Kunka, M. Amberger, J. Mohr, and F. Pfeiffer. **Non-binary phase gratings for x-ray imaging with a compact Talbot interferometer**. *Optics Express*, **22**:547–556, 2014. 55

Declaration

I herewith declare that I have produced this paper without the prohibited assistance of third parties and without making use of aids other than those specified; notions taken over directly or indirectly from other sources have been identified as such. This paper has not previously been presented in identical or similar form to any other German or foreign examination board.

The thesis work was conducted from 01.11.2009 to 25.04.2014 under the supervision of Prof. Dr.rer.nat. Tilo Baumbach at the Laboratory for Applications of Synchrotron Radiation, Faculty of Physics, KIT.

Karlsruhe,